

POLITECNICO DI TORINO

Corso di Laurea Magistrale in Ingegneria Aerospaziale

Master of Science Thesis

Full-PIC Simulation of Ion Thruster Plume and Thrust Vectoring Devices



Supervisor:

Prof. Lorenzo Casalino

Company Supervisor:

Ing. Mario Pessana

Candidate:

Artem Kolisnichenko S235824

December 2018

Una dedica speciale a Sioma che mi è sempre stato vicino...

Acknowledgements

I would like to thank my company advisor, Ing. Mario Pessana from Advanced Propulsion Division of Thales Alenia Space, for giving me this unique and challenging opportunity, for all his advices and support on my research.

A special thanksgiving goes to Ing. Demis Boschetti from EMC Division of Thales Alenia Space. His group is a special one, and honestly, it has been a big pleasure to perform my simulations in the EMC department and I am really happy that my research started during the FIFA World Cup 2018. The results presented here are obtained thanks to many discussions with a large number of knowledgeable colleagues.

Above all I want to say thank to my family. To my mother for the total and unconditional support she has always given me. You sacrificed a lot for me and my graduation, you are an example from whom take inspiration. To Sioma, I will never forget you and your support during long nights of studying. And finally, the hugest thanks goes to Nastya for her support and much more, she has never given up supporting me during all my university career and not only!

Abstract

Electric propulsion is a mature and widely used technology in modern spacecraft applications. This kind of propulsion has strongly demonstrated its main advantages both analytically and in-flight experimentally. However, during a mission the need to control the thrust vector may arise, since a displacement of the center of gravity may be caused by the propellant consumption and the rotation of solar arrays. Thus, the ability to control the thrust vector orientation opens new possibilities for mission optimization; 8-10 degrees in all directions are sufficient to satisfy current needs. Normally, the thrust vector control (TVC) is achieved by mounting the thruster on a mechanically actuated gimbal platform or robotic arms; these techniques are found to be heavy and expensive, and may affect the overall reliability of the system.

The purpose of this thesis is to contribute in collaboration with Advanced Propulsion Department of Thales Alenia Space to the analysis of non-mechanic TVC, applicable to the electric propulsion thrusters, capable to control the thrust direction in a reliable and efficient way, and characterized by being simple and low-cost. The control of the orientation of plasma plume emission in self-consistent electric field cannot be described by an analytical model, since finite beams have the freedom to expand their cross section in response to the space-charge forces. Therefore, a particle simulation is needed to resolve the problem.

For this reason the thesis presents Full-Particle-In-Cell numerical simulations of ion thruster plume and magnetic thrust vectoring concept applied on it. The full PIC method, using CST Particle solver, treats both ions and electrons as macro particles, and is applied to the VECMAN MTV concept first, with the twofold objective of verifying the suitability of the PIC model to analyze the plasma plume to the vectoring device and to verify the suitability of the VECMAN to perform vectoring.

Contents

1	Introduction to Electric Propulsion	1
1.1	Overview	1
1.2	Gridded Ion Thruster	2
1.3	Electric Thruster Plumes	4
1.3.1	Plume Physics	4
1.3.2	Plume Modeling	4
1.4	Particle Velocity Distribution	7
1.5	Thesis Objectives and Description	8
2	Thrust Vector Control Devices	9
2.1	General Principles	9
2.2	Thrust Steering by means of Internal Modifications	11
2.3	Thrust Vectoring by acting on Plasma Plume	13
3	Plasma Physics on Computers	19
3.1	Introduction to Plasma Physics	19
3.2	Collisionless plasma	22
3.3	Fully-Kinetic Methodology	23
3.4	Particle-In-Cell Methodology	25
3.4.1	Computation of Charge Density	27
3.4.2	Computation of Field Equations	27
3.4.3	Computation of Equations of Motion	28
3.4.4	Algorithm Output	31
3.4.5	Restriction of Simulation Parameters	32
3.5	CST Particle Studio	32
4	Code validation with One-Dimensional Analytical Model	35
4.1	One-Dimensional Analytical Theory of Space Charge Flow	35
4.2	Three-Dimensional Particle In Cell Simulations	42
4.2.1	Simulations setup	42
4.2.2	Results and Discussion	43

5	Particle-In-Cell Simulations	51
5.1	GOCE's T5 Ion Thruster Plume Modeling	51
5.1.1	GOCE ITA Plume Data	51
5.1.2	Source Models	52
5.1.3	Simulation Setup	54
5.1.4	Dimensional Scaling	58
5.1.5	Plume Model Validation	58
5.2	Magnetic Thrust Vectoring Concept	65
5.2.1	Magnetic Steering Analysis	65
5.2.2	Simulation Setup	66
5.2.3	Beam Diagnostics	68
5.3	Vectorial Magnetic Nozzle Concept	77
5.3.1	Preliminary Analysis	77
5.3.2	Vectoring Performance	77
6	Conclusions	83
6.1	Final discussion	83

List of Figures

1.1	Schematic cross section drawing of a gridded ion thruster with electron bombardment plasma generation.	3
1.2	Schematic representation of two regions of a plasma plume and a stream-line containing 95% of ion current. The typical shapes for initial conditions for the far-region plume are reported: initial profiles for velocity slope δ , axial velocity v , and density ν , the initial divergence angle α_0 , and the equivalent final divergence angle α_F [9].	5
2.1	Thrust Module Assembly composed by two Hall effect thrusters mounted onto a Thrust Mechanism Orientation [40]	10
2.2	Ion beam deflection using accelerator grid traslation [44].	11
2.3	Hall effect thruster scheme with the external steering coil [47].	12
2.4	Hall thruster (1) with small coils (2) mounted at the engine exit (3) (a) and the same thruster with a big coil (4) tilted at 30° (b) [49].	13
2.5	External magnetic deflection configuration [34].	14
2.6	Arrangement of two (5) and four (6) rectangular coils for thrust vectoring mounted on a SPD-100 [49].	15
2.7	Vector magnetic nozzle composed by accelerated plasma plume (1), permanent magnets (2) and three non-concentric coils capable of controlling the thrust vector (3-4-5) [52].	16
2.8	Left: Sketch of a VECMAN constructed with $N = 3$ elliptical coils tilted at $\alpha = 15^\circ$ place at the exit section of a HPT-like plasma source. Right: A configuration made of $N = 5$ and $\alpha = 15^\circ$ interlocked intertwined circular coils slightly offset from the origin of coordinates [51].	17
3.1	Schematic view of a plasma (a) and a discharge (b) [4].	19
3.2	Time scales ordering for a general plasma.	21
3.3	A typical cycle in a particle simulation code.	26
3.4	One dimensional numerical grid uniformly spaced [26].	28
3.5	Leap-frog integration method showing time centering of force F while advancing v and of while advancing x	29
3.6	Solution for ω in terms of ω_0 for simple harmonic motion. Phase error is the difference between the numerical and exact frequency ω_0 [26].	31

4.1	Non-monotonic potential profiles associated with one-dimensional non-neutralized ion beam emission between two plane electrodes.	39
4.2	Neutralization of one-dimensional ion beam model [6].	40
4.3	Potential profiles for one-dimensional ion beam neutralized at distance Δx from accelerator grid [6].	41
4.4	Simulation setup.	42
4.5	Total number of particles in the simulation domain at different time steps	45
4.6	Maximum potential \hat{V} on the $x - y$ cutting plane at different time steps.	46
4.7	Potential profiles for ion beam neutralized at different distances $\Delta z/z_a$ from emission surface of radius $R_b = 10$ cm.	46
4.8	Ion density number for cases A1, A2 and A3 in (a), (b) and (c), respectively, at the simulation steady-state.	47
4.9	Potential map for cases A1, A2 and A3 in (a), (b) and (c), respectively, at the simulation steady-state.	47
4.10	Ion density number and potential maps for case A4 in (a) and (b), respectively, at the simulation steady-state.	48
4.11	Ion density number and potential maps for case A5 in (a) and (b), respectively, at the simulation steady-state.	49
5.1	Schematics of the beam probe diagnostic used in [23].	51
5.2	Ions and electrons emission surfaces.	54
5.3	Simulation setup with curves representing the probes.	55
5.4	Potential (a) and charge density (b) after 10000 time steps on the center $z - y$ plane.	56
5.5	Ions (a) and electrons density (b) after 10000 time steps on the center $z - y$ plane.. . . .	57
5.6	Macro-particles count in the simulation domain.	59
5.7	Macro-particles count after 500 time steps in the simulation domain.	60
5.8	Ion current density validation at distance $12R$ from thruster exit.	61
5.9	Ion current density validation and filtered simulation solution at distance $12R$ from thruster exit.	62
5.10	Plasma potential validation at distance $12R$ from thruster exit.	62
5.11	Electron density at distance $12R$ from thruster exit.	63
5.12	Ion density map at the simulation steady-state on the center $z - y$ plane.	63
5.13	Electron density map at the simulation steady-state on the center $z - y$ plane.	64
5.14	Potential map at the simulation steady-state on the center $z - y$ plane.	64
5.15	Plume deflection angle as a function of applied magnetic field to the ion beam for a fixed application distance $L = 10$ cm.	65
5.16	Simulation setup and MTV concept applied at the distance R from thruster exit.	67
5.17	Macro-particles count in the simulation domain for thrust level 20 mN.	67
5.18	Ion density distribution at distance $z = R$ from thruster exit.	69
5.19	Ion density distribution at distance $z = 6R$ from thruster exit.	70

5.20 Ion density distribution at distance $z = 9R$ from thruster exit.	70
5.21 Ion density distribution at distance $z = 12R$ from thruster exit.	71
5.22 Ion density distribution at distance $z = 15R$ from thruster exit.	71
5.23 Ion density distribution at distance $z = 18R$ from thruster exit.	72
5.24 Ion density for thrust demands 3 mN (a), 8.3 mN (b) and 20 mN (c).	73
5.25 Electron density for thrust demands 3 mN (a), 8.3 mN (b) and 20 mN (c) on the center $z - x$ plane.	74
5.26 Potential maps for thrust demands 3 mN (a), 8.3 mN (b) and 20 mN (c) on the center $z - x$ plane.	75
5.27 Charge density maps for thrust demands 3 mN (a), 8.3 mN (b) and 20 mN (c) on the center $z - x$ plane.	76
5.28 Simulation setup of VECMAN concept modeled with one coil placed at distance D from thruster exit on the center $z - y$ center. The neutraliser is positioned close to the thruster.	78
5.29 Magnetic field generated by a VECMAN coil tilted at 30° with respect to x axis on the center $z - y$ center. Map colors illustrate the magnitude of the magnetic field along z axis.	79
5.30 Magnetic field generated by a VECMAN coil tilted at 30° with respect to x axis. Map colors illustrate the magnitude of the magnetic field along y axis on the center $z - y$ center. The field B_y is responsible of thruster vectoring.	79
5.31 Ion density map on the center $z - x$ center.	80
5.32 Ion density map on the center $z - x$ center.	80
5.33 Ion density distribution at different distances from thruster exit.	81

List of Tables

4.1	Simulation cases	43
4.2	Simulation results and comparison with one-dimensional model.	44
5.1	Steady state performance parameters.	52
5.2	Performance parameters of a gridded ion thruster having 10 cm of diameter and the magnetic field needed to carry out a thruster vector angle of 8° . . .	66
5.3	Simulation cases to carry out a thruster vector angle of 8°	66
5.4	Simulation case to carry out a thruster vector angle of 8° with VMN.	77

Chapter 1

Introduction to Electric Propulsion

1.1 Overview

Electric propulsion (EP) is a mature technology used in modern spacecraft applications ranging from technology demonstrators to science missions and commercial applications such as station-keeping on geostationary communications satellites. Its main advantage with respect to the conventional chemical propulsion, is the mass of propellant consumption m_p , given by the rocket equation of Tsiolkovskiy [1]

$$m_f = m_0 e^{-\Delta v/c} \quad m_p = m_0 \left(1 - e^{-\Delta v/c}\right), \quad m_0 = m_f + m_p \quad (1.1)$$

where m_f is the final spacecraft mass, m_0 is the initial spacecraft mass, Δv is the required mission velocity increment and c is the exhaust velocity of the thruster. Chemical propulsion is energy limited, as its performance in terms of c depends on the amount of energy per unit mass E_{ch} stored in the chemical bonds of the propellant, which is used to accelerate the exhaust gas.

$$E_{ch} = \frac{E_{reaction}}{m_p} \rightarrow \dot{m}_p E_{ch} = \dot{m}_p \frac{c^2}{2} \rightarrow c = \sqrt{2E_{ch}} \quad (1.2)$$

Thus, once the propellant is chosen the maximum exhaust velocity is limited as the chemical reaction energy is fixed by the propellant. For example, with liquid hydrogen/oxygen combustion, as the one used in Space Shuttle Main Engine, the maximum achievable exhaust velocities are of order 4-5 km/s.

In contrast, EP is power limited, since electric thrusters use the electric energy from a primary power source P_e , like the solar array, to produce an ionized propellant and accelerate it into vacuum. In this way, the propellant exhaust velocity depends on how much electric power is available on board. Typically, ion thrusters operate with exhaust velocities around 20'000-40'000 m/s.

$$\eta_t P_e = \frac{\dot{m}_p c^2}{2} = \frac{Tc}{2} \rightarrow c = \sqrt{\frac{2\eta P_e}{\dot{m}_p}} = \frac{2\eta P_e}{T} \quad (1.3)$$

where η_t is the thrust efficiency and $T = \dot{m}_p c$. According to the rocket equation (1.1), a high exhaust velocity can significantly decrease the launch mass of a spacecraft. This property of EP is very attractive to mission designers, since it means that a smaller portion of the total system mass needs to be devoted to fuel. Hence, an interplanetary probe can carry a larger payload, or the initial mass can be reduced, allowing the probe to be launched on a smaller launch vehicle which is cheaper.

There are many figures of merit for electric thrusters, but mission and application planners are primarily interested in thrust, specific impulse, and total efficiency to relate thruster performance to the delivered mass and change in the spacecraft velocity during thrust periods.

Contrary to chemical propulsion, where the thrust can be very large by increasing the mass flow rate \dot{m}_p , the limited available electric power in electric propulsion allows achieving much lower thrust levels, usually about 50-200 mN, which brings long thrust periods once in space and the impossibility to produce sufficient lift-off forces to overcome the gravitational pull of the Earth.

While thrust is self-explanatory, specific impulse (I_{sp}) is defined as the propellant exhaust velocity divided by the gravitational acceleration constant $g_0 = 9.80655 \text{ m/s}^2$

$$I_{sp} = \frac{c}{g_0} \quad (1.4)$$

Following Equation (1.1), it is clear that a higher specific impulse allows to achieve a given Δv expending much less propellant mass, and thus, reduces the total mass required to complete a mission.

The thrust efficiency η_t is the jet power produced by the thrust beam (P_t) divided by the electrical power required by the propulsive system (P_e)

$$P_t = \frac{\dot{m}_p c^2}{2} = \frac{Tc}{2} \quad \rightarrow \quad \eta_t = \frac{P_t}{P_e} = \frac{\dot{m}_p c^2}{2P_e} = \frac{Tc}{2P_e} = \frac{T^2}{2\dot{m}_p P_e} \quad (1.5)$$

Naturally, spacecraft designers are then concerned with providing the electrical power that the thruster requires to produce a given thrust.

1.2 Gridded Ion Thruster

In electric propulsion the acceleration methods used to produce thrust can be classified in three categories: electrothermal, electrostatic and electromagnetic [2]. However, in this thesis the main topic is the gridded ion thruster (GIT), which works according to electrostatic acceleration principle. The choice of the engine is due the available experimental data. A schematic cross section drawing of a gridded ion thruster is illustrated in Figure (1.1). The geometry is described in terms of three basic components:

- Plasma generator: the neutral propellant atoms are injected into the ionization chamber, where the plasma is generated by means of electron bombardment [3] (high-energy primary electrons are released into the discharge chamber by a cathode) or

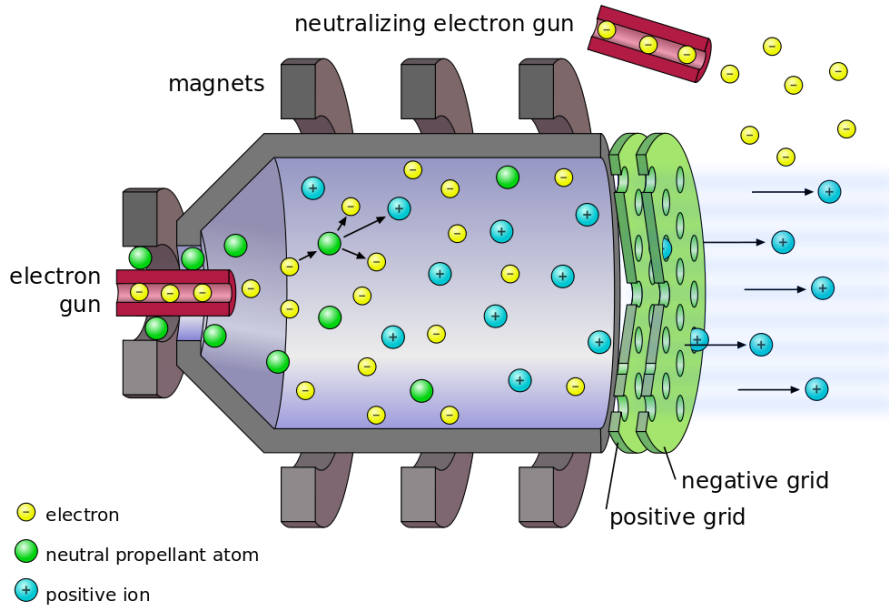


Figure 1.1: Schematic cross section drawing of a gridded ion thruster with electron bombardment plasma generation.

radio-frequency radiation [4] (free electrons are accelerated by electromagnetic waves. Thus, ions and low energy electrons are generated by collisions between primary electrons and neutral propellant atoms to form a quasi-neutral steady-state plasma in the discharge chamber. Usually, magnet-generated magnetic fields are applied to contain primary electrons and to avoid their premature escape to anode, and increase the probability of ionizing collisions with atoms. It can be assumed that ions are extracted to neutrals and only neutral atoms remain in this chamber. A more detailed description of an ion thruster plasma generators can be found in Chapter 4 of [2].

- Screen and acceleration grids: from a generated plasma in the discharge chamber, the ions are extracted by a screen grid (positively charged) and the electrons are kept from leaving through this grid, and are collected by an anode. Then, only positive charges are accelerated by strong electric fields created by a potential difference applied between the biased multi-aperture grids. The acceleration grid is negatively charged. The accelerated ion density current is space-charge limited by Child's law [5] over the accelerating gap between the grids. The exhaust velocity is given by

$$c = \sqrt{\frac{2q}{m_+} \Delta V}. \quad (1.6)$$

The potential difference applied between the two grids are of orders up to 1 kV and thanks to the high efficient ionization techniques (from 60% to >80%), the specific

impulse may reach un to 4500 seconds. As for the ionization chamber, a more detailed description of the acceleration process is found in Chapter 5 of [2].

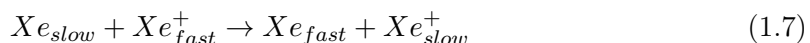
- In order to avoid a negative charging of the spacecraft, electrons must be ejected from the spacecraft into the ion beam downstream the accelerating grid. This is usually accomplished by means of electron-emitting device, such as hot filament, plasma-bridge or electron-gun injector. The electrons are provided at the same current as the ions. According to one-dimensional theory the neutralization has to be accomplished within a few distances between the acceleration gap [6] from the thruster exit. However, in practise the cathode is found located more downstream [7]. Different ion beam neutralization techniques are found [6] and a detailed explanation is reported in Chapter 6 of [2].

1.3 Electric Thruster Plumes

1.3.1 Plume Physics

Integration and determination of location of electric thruster on a spacecraft is one of the biggest challenges of system engineers, since the thruster plume interacts with the other subsystems, such as the solar arrays or onboard sensors. This interaction can produce mechanical erosion or contamination and forces or torques on object it interacts with [8].

Basically, plumes consist of ions and electrons of various energies and some non-ionized propellant neutral gas. The dominant specie is represent by energetic beam ions accelerated by the thruster fields. Since in EP thrusters the ionization efficiency is not 100%, some fraction of the propellant leaves the thruster as a neutral gas with low thermal velocities. In this way, close to the thruster exit, the fast ions collide with the neutral atoms and charge-exchange ions form. This reaction converts slow moving neutral atoms and fast moving ions into fast moving neutrals and slow moving ions:



where Xe_{fast} are not relevant since their trajectory is the same of original ions. However, in the beam, the electric field develops also in radial direction due to the geometric divergence of the plume and slow moving ions Xe_{slow}^+ feel this local electrostatic field and they are accelerated radially out of the plume. When these ions impact on spacecraft surfaces, they might produce sputtering and the sputtered material can deposit on other surfaces, contaminating them. Both the direct sputtering damage and the contamination due to deposition provoke a degradation in the performance of the affected components.

1.3.2 Plume Modeling

In order to achieve higher thrust levels, a heavy neutral gas is used as a propellant. This leads to have very different dynamics for ions and electrons, since the mass of electrons is 5 or 6 orders of magnitude lighter, and thus, they respond much more faster to external

perturbations. When an external applied magnetic field is present in a thruster plume, a classification into two fundamental families of plasma plumes is needed:

- *Magnetized plasma plumes*: electrons are forced to follow Larmor orbits around the local magnetic field direction and can traverse the field lines only through rare collisional events. This magnetically guided plasma is present in Helicon plasma thruster, AF-MPD, ECR thruster and VASIMR.
- *Non-magnetized plasma plumes*: consist of the expansion of quasi-neutral plasma plume in its self-consistent electric field which is formed by a plume of ions neutralized with electrons. It is present in gridded ion thruster and Hall effect thruster plumes. A GIT plasma plume is a topic of this thesis.

An EP plume can be simulated in different ways depending on the type of the problem to be solved. Generally, a plasma plume can be distinguished in *near region plume* and *far region plume*, depending on the distance from the source thruster. The two regions are illustrated in Figure (1.2).

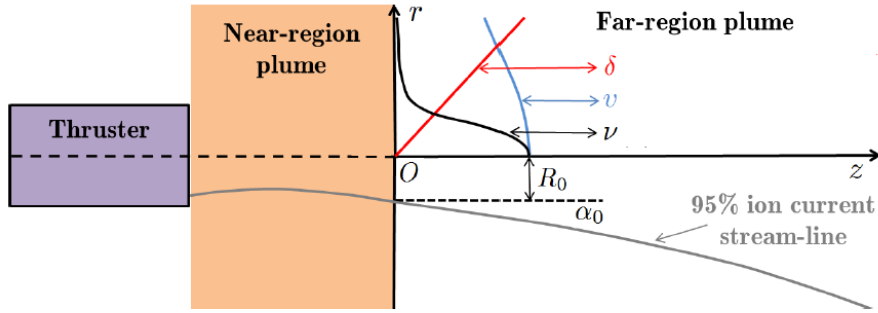


Figure 1.2: Schematic representation of two regions of a plasma plume and a stream-line containing 95% of ion current. The typical shapes for initial conditions for the far-region plume are reported: initial profiles for velocity slope δ , axial velocity v , and density ν , the initial divergence angle α_0 , and the equivalent final divergence angle α_F [9].

The *near region plume* is a region close to the thruster exit, up to a few thruster radii, characterized by the presence of large neutral density which brings to collisions and creation of CEX ions surrounding the spacecraft and the influence of neutraliser, which generates a non-homogenized three-dimensional plume, since the neutralization is occurring. Moreover, the residual electric and magnetic fields from the thruster may be observed.

Experimentally, this region is easy to measure both in vacuum chambers, for GIT [10, 11, 12, 13, 14] and HET [15, 16, 17, 18, 18, 19], and onboard real satellites [20, 21, 22]. Commonly, the measurements are executed at distances of about 1 m from the thruster exit. The plume properties, such as current density profile, electrons temperature, plasma potential, divergence angle, etc, may be identified [23, 24]. The plume dispersion angle is around 30-40 deg for HETs and 10-20 deg for GIT [25].

Numerically, a plasma thruster plume can be simulated in different ways depending on the type of the problem to be solved. When three-dimensional physical phenomena are present with large variation of plasma properties and electron-ion couplings, as happens in the near region, the full physics is required to be solved. This can be attained with a *full-Particle-In-Cell* [26] or a *direct kinetic codes* [27]. Indeed, these methods are essential to study complex problems like the neutralization process in GIT or the anomalous transport of the electrons in the axial direction in HET. However, the computation cost is excessive for simulation domains of a few meters in a 3D problem, since in full-PIC the timestep and the cell size are constrained by time and length scales of the fastest specie (for electrons these are limited by Debye length λ_{De} and plasma frequency ω_{pe}), respectively; and in kinetic codes the Vlasov-Maxwell system of equations for a distribution function is 6-dimensional and the solution is extremely expensive (10 cells in every dimension, which is a bad resolution, lead to have a huge domain of 10^6 total cells). Thus, several assumption must be made. A more detailed description of full-PIC and full-kinetic models is provided in the following chapter.

In addition, the problem of ion beam neutralization may be studied with a particle-particle (PP) model [28], but this method is found to be not efficient as full-PIC, since the computing time of PP scales as $o(N^2)$, where N is the number of macroparticles used in the simulation [27].

The *multi-fluid models* are not suitable for studying this region, as a large number of fluids per species has to be introduced, in order to represent deviations of the distribution function from a Maxwellian, and a kinetically-unjustified assumption for fluid equations closures has to be made.

In order to reduce the computational cost with respect to full-PIC or fully kinetic simulations, the use of an *hybrid-PIC method* is suggested, in which the fastest species (electrons) are treated as a fluid and the heavy and slow species (ions and neutrals) are simulated as macro-particles of a PIC sub-model. This choice, compared to full-PIC model, permit to eliminate the need of solving λ and ω_{pe} , as typically ions are 2-3 orders of magnitude slower than the electrons; and compared to multi-fluid models, an hybrid code maintains a generic distribution function for all heavy species particles. However, some simplifications about electrons thermodynamics are made by introducing Boltzmann relation, which requires that the electrons behave as an isothermal local equilibrium fluid, or by employing a polytropic law. An hybrid-PIC method is a good choice to study plasma plume expansion and its interaction with satellite and other objects. For example, spacecraft contamination and charge-exchange plasma environment by means of hybrid-PIC simulations were studied in [29] and in [30], respectively, since the electrons physics are not required to be modelled as particles.

The *far region plume* is the zone farther away from the thruster where the plume has already been quasi-neutralized. It starts from a few thruster radii away from the exit. The region is characterized by near-collisionless expansion with a single-peaked plume density profile, since the effects of neutraliser become negligible with respect to the plume kinetic energy, the residual thermal pressure, and the self-consistent ambipolar electric field. The far plume is hard to measure due technological limits of vacuum chamber testing [2]; large

vacuum tanks and low chamber pressure are required to perform measurements at distances of 7-10 m from the thruster exit [31]. Nevertheless, numerically this region can be studied with a collisionless fluid models [9] or with analytical models [32], as these methods require low computational cost even on huge domains.

1.4 Particle Velocity Distribution

In ion and Hall thrusters, the charge particles are subject to a large number of collisions with each other, and with the other species in the plasma. This effect of collisions is to develop a distribution of the velocities for each species, such as each particle will move with a speed that is a function of the macroscopic temperature and mass of that species. The charged particles in the thruster, therefore, can usually be described by different velocity distribution functions, and the random motions can be calculated by taking the moments of those distributions.

Commonly, in electric thrusters have a Maxwellian velocity distribution for the charged particles, which is the most probable distribution of velocities for a group of particles in thermal equilibrium. In three dimensions, the Maxwellian velocity distribution function is

$$f(u, v, w) = \left(\frac{m}{2\pi k_B T} \right)^{3/2} \exp \left[-\frac{m}{2k_B T} (u^2 + v^2 + w^2) \right], \quad (1.8)$$

where u , v , and w are the velocity components in the three coordinate axes. The average kinetic energy of a particle in the Maxwellian distribution is

$$E_{ave} = \frac{\iiint_{-\infty}^{\infty} \frac{1}{2} m (\vec{v})^2 f(u, v, w) dudvdw}{\iiint_{-\infty}^{\infty} f(u, v, w) dudvdw} = \frac{3}{2} k_B T \quad (1.9)$$

and the average speed

$$v_{ave} = \left(\frac{8k_B T}{\pi m} \right)^{1/2}. \quad (1.10)$$

In the plasma electrons are observed to be very mobile and tend to make a large number of coulomb collisions with each other. Thus they can usually be characterized by a Maxwellian temperature T_e . In fact, in ion and Hall thrusters the electrons tend to be relatively hot, compared to the ions and atoms, since they are typically injected into the plasma or heated by external mechanisms to provide sufficient energy to produce ionization.

On the other hand, the ions are accelerated with high velocities, but their random velocities and temperature is low, compared to that of electrons. In fact, the thrusters with non-magnetized plasma plumes have cold ions and Maxwellian electrons [2]. Typical electron-to-ion temperature ratio is

$$\frac{T_e}{T_i} = 10. \quad (1.11)$$

1.5 Thesis Objectives and Description

One of the objectives of this thesis is to develop and validate an ion thruster plasma plume model having ions and electrons emitters separated in order to study the neutralization process of an ion beam. In this way, with the developed model it is possible to study new neutralization architectures for the next generation missions.

In the second moment, such plasma plume model is applied to study a magnetic thrust vectoring concept in order to establish how large the magnetic field should be to provide deflections of interest and to investigate the relative position of the neutraliser with respect to the thrust vector device. In addition, the plume model was tested on the Vectorial Magnetic Nozzle, since its patent cited the possible application on gridded ion thrusters.

From the observation made about the plume modeling in Section 1.3.2, the need of a full-Particle-In-Cell code has arisen to reach both objectives.

Thus, for the ion thruster neutralization, several three-dimensional full-PIC simulations have been performed by using a commercial software called CST Particle Studio and its fully integration with the multi-purpose 3D EM modules of CST STUDIO SUITE, such as the CST EM STUDIO electro and magneto-static solvers, has allowed to study magnetic thrust vectoring concepts.

A state-of-the-art about the thrust vectoring methods is introduced in Chapter 2 with a particular attention on the existing patented devices. Then, a detailed information about the plasma simulation on computers and Particle-In-Cell methodology is provided in Chapter 3. Chapter 4 describes the code validation against a one-dimensional analytical model and the simulations results are reported in Chapter 5. The last Chapter 6 summarized the conclusions and future work.

Chapter 2

Thrust Vector Control Devices

2.1 General Principles

One of the differences between chemical propulsion and electric propulsion is the thrust level. Usually, in electrostatic thrusters typical values ranges up to 50-200 mN, and for a given mission, fixed the total impulse I_t , these values bring to have long burn period in space. The thrust is achieved by ejecting energetic beam of ionised propellant from the engine. The position and the stability of the thrust vector are important properties of the beam for the design and operation of the attitude and orbit control system (AOCS) of the spacecraft. The direction and magnitude of thrust is defined by spatial and angular distribution in time of the plasma plume ejected from the propulsion system. In order to optimize the mission's AOCS, the position of the thrust vector relative to the centre of mass is required to be known during the mission. However, the displacement of the centre of mass is uncertain, since it can be caused by the propellant consumption in the tanks or movements of solar arrays and other appendages and may lead to large and unacceptable propellant consumptions. Thus, a thrust vectoring control (TVC) can be used to compensate such misalignment or manufacturing inaccuracies. Furthermore, for missions such as station-keeping or orbit transfer the ability to control the direction of the thrust vector on the spacecraft allows to enhance the mission performance by minimizing transfer time or final spacecraft position error [33]; while during primary propulsion manoeuvres it can be employed to offload the reaction wheels, what is usually achieved by a chemical propulsion system. In effect, according to the requirements of the thrust vector control deflections of about 8 to 10 degrees in all directions are sufficient to accomplish the requirements of most current propulsion missions [34].

Basically, the thrust direction on a spacecraft may be achieved by using two or more thrusters and changing their relative amplitude of thrust. As an example, the architecture of six thruster placed at the edges of a star was proposed and patented as a method to control the thrust vector [35]. Nevertheless, this method is expensive and increases weight, but results to be promising for large and high power exploration missions where several thrusters would be required to operate with maximum total impulse capability.

A common technique for thrust vectoring consist of mounting the engines on gimbaled

thrust orientation mechanism (TOM), it was used on ESA's Artemis communications satellite [36] and on the SMART-1 spacecraft [37], or on robotic arms [38]. In this way the thruster can be swiveled relatively to the spacecraft. However, such TVC solution is found to be heavy, complex and expensive and may affect the overall reliability of the system, since it compromises many moving mechanical parts. Typically, the mass of TOM exceeds that of the thrusters. In Figure (2.1) is illustrated the Snecma Thrust Module Assembly (TMA), flown on the Intelsat-X-02, Inmarsat-4 F1 [39] and Inmarsat-4 F2 satellites, includes two Hall thrusters fitted onto a Thrust Orientation Mechanism with $\pm 12^\circ$ gimbal authority on 2 axes [40].

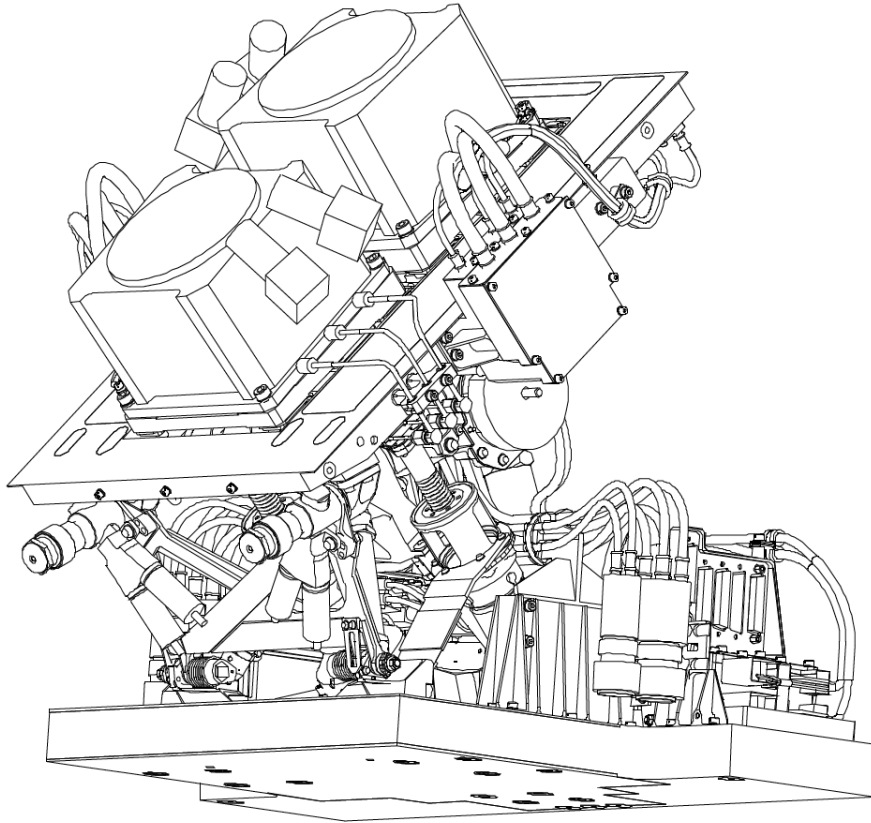


Figure 2.1: Thrust Module Assembly composed by two Hall effect thrusters mounted onto a Thrust Mechanism Orientation [40]

Without displacement or rotation of thruster, to change the direction of thrust vector of a generic axisymmetrical thruster, which generates force along the axis of the symmetry, it is necessary to include the additional force in perpendicular direction to the axis [41]. The lateral force breaks the azimuthal uniformity of the plume and can be localized in different characteristic areas of the engine [42]:

- In the area of the anode, if present;

- In the ionization zone;
- In the acceleration zone;
- In the external plasma.

Moreover, such lateral force might be obtained according to these physical concepts:

- Electrostatic or magnetic vectoring;
- By a non-uniform injection of propellant or geometrical design modifications.

2.2 Thrust Steering by means of Internal Modifications

In literature [34] a promising option for thrust vectoring for an ion engine was proposed. It consists of employing electrostatic deflection of the ions within the grid system, by lateral translation of the acceleration grid with respect to the screen grid. A movement of under 0.5 mm produces the beam deflection of 8° to 10° . A single grids aperture is sketched in Figure (2.2). This system is patented [43]. Although, it should be noticed that the grid is moved by the usage of actuators, and thus, an internal modification of the thruster is required, which may affect the life time by causing direct impingement or overcrossing within the grid.

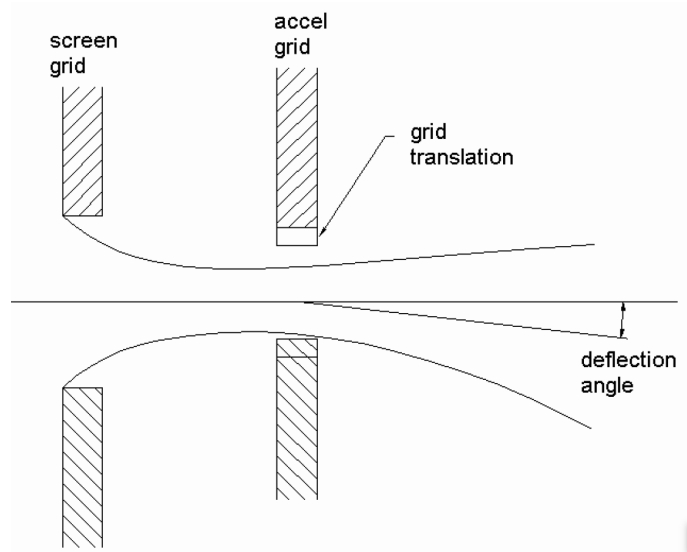


Figure 2.2: Ion beam deflection using accelerator grid traslation [44].

Thrust steering of the Hall thruster plume by means of localized unsymmetrical injection of propellant and addition of external magnetic steering system has been proposed in [42]. The azimuth modification of the radial magnetic field in the magnetic gap changes

the electric field, which is used to accelerate the ion beam. Then, the deformation of equipotential surfaces causes the angle of the thrust vector to be deflected. This concept has been proposed in patent [45] and comprises a four horizontal horseshoe-shaped pole pieces with electromagnet coils. The geometry is showed in Figure (2.3). A theoretical beam deviation of 11° was predicted by the simulations at a cost of up to 12% of thrust efficiency and a 23% drop of specific impulse, but the test campaign of a prototype showed that 15° could be reached [46]. However, this deviation angle led to a local overheating of the ceramic walls of the discharge channel, drops in thrust efficiency and local ceramic erosion. The performance model of such method was developed and tested too [47].

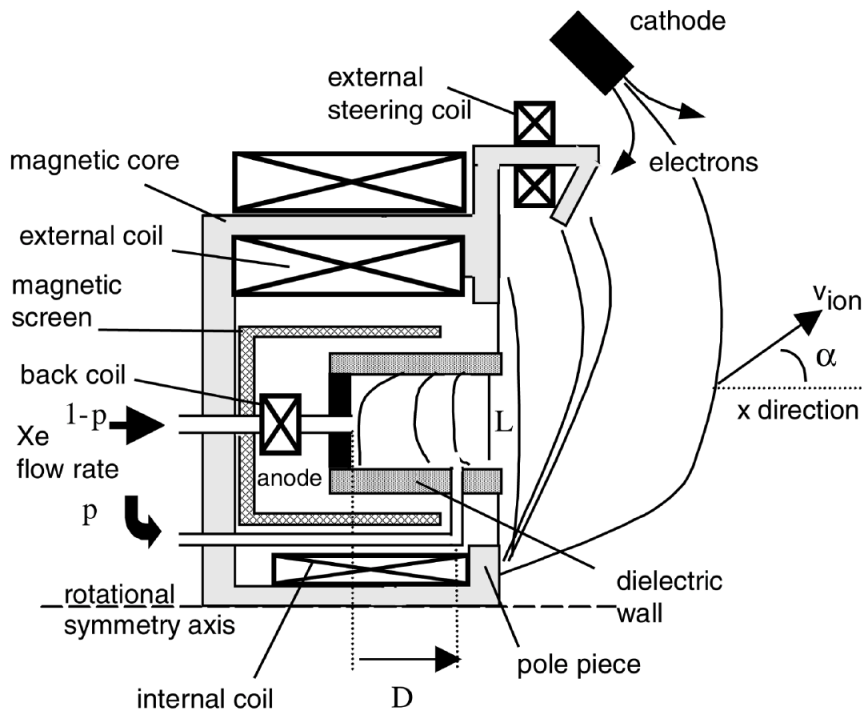


Figure 2.3: Hall effect thruster scheme with the external steering coil [47].

Furthermore, different devices for Hall thrusters capable to create additional magnetic field that interact with the proper magnetic field of Hall thrusters are proposed in literature [48]. The external magnetic field is generated by two pairs of small coils placed at the engine exit with their axes perpendicular to the direction of the flow of plasma. The configuration with only two coils was tested in order to evaluate its capability of steering the thrust [49]. The scheme is in Figure (2.4(a)). Experiments showed that small deflections of $1^\circ - 2^\circ$ are achievable. Moreover, in the same patent another TVC patented device, called Vectorial Magnetic Nozzle (VMN) [50], was applied to modify magnetic fields of a HET. It includes an arrangement of $N \geq 3$ intertwined magnetic coils located at the thruster exit. In this way, each coil is tilted at a fixed angle with respect to the axis of the thruster, and precessed an angle $2\pi/N$ with respect to each other to create a rotational-symmetric

configuration. In Figure (2.4(b)) is illustrated one of these circular coils tilted at 30° . Results of the experiment reported thrust vector deflection up to 3° . However, this device may be applied in a different way: instead of modifying the internal magnetic field of the thruster, a field generated by coils can be applied directly on a plasma beam ejected from the thruster.

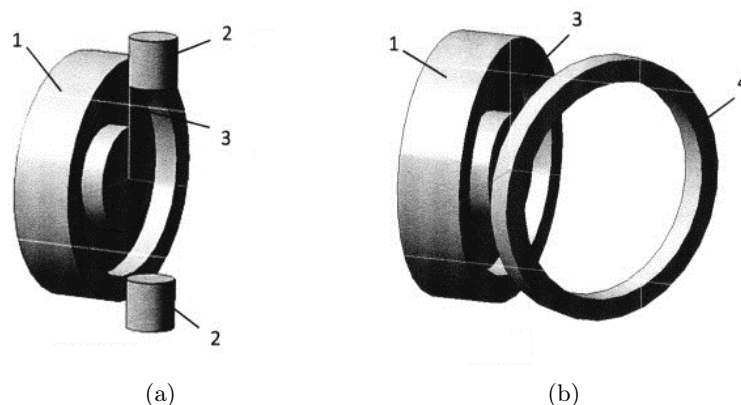


Figure 2.4: Hall thruster (1) with small coils (2) mounted at the engine exit (3) (a) and the same thruster with a big coil (4) tilted at 30° (b) [49].

2.3 Thrust Vectoring by acting on Plasma Plume

Conceptually, a non-mechanical method to steer an ion beam, without modifying the internal fields topologies, can be achieved by means of applying electric or magnetic field trasversally accross the charged ions as they emerge from the grids of the thruster. In fact, both concepts applied on the ion thruster plume were proposed in [34]. It is believed that these concepts are applicable to Hall effect thrusters too, while the application on thrusters with the magnetized plume is to be studied.

The description of the electrostatic transverse field generated by two pairs of orthogonal deflectors plates, and the ion beam passing through it, was discussed in [34]; but nothing about the position of the neutraliser was mentioned, which can be placed upstream or downstream of the TVC device. Hence, the neutralization process has to be studied too, since electrons are attracted towards the positive plate with a high voltage, and thus, they impact on it with high energy causing sputtering. Moreover, the electric field edge effects of deflecting plates may interact with internal thruster's fields, which leads in decreasing of performances.

The magnetic concept generates the magnetic field in traversal direction with respect to the thruster longitudinal axis, which interacts with the ion beam ejected from the thruster, and thus, deflects the thrust vector. Such magnetic field can be created by different devices, but preliminary calculations are needed to determinate how large this field would have to be to provide deflections of interest. Let us consider a configuration composed by the thruster

ion beam and four electromagnetic devices, which produces the uniform and perpendicular to the ion motion magnetic fields B_x and B_y . A sketch is provided in Figure (2.5).

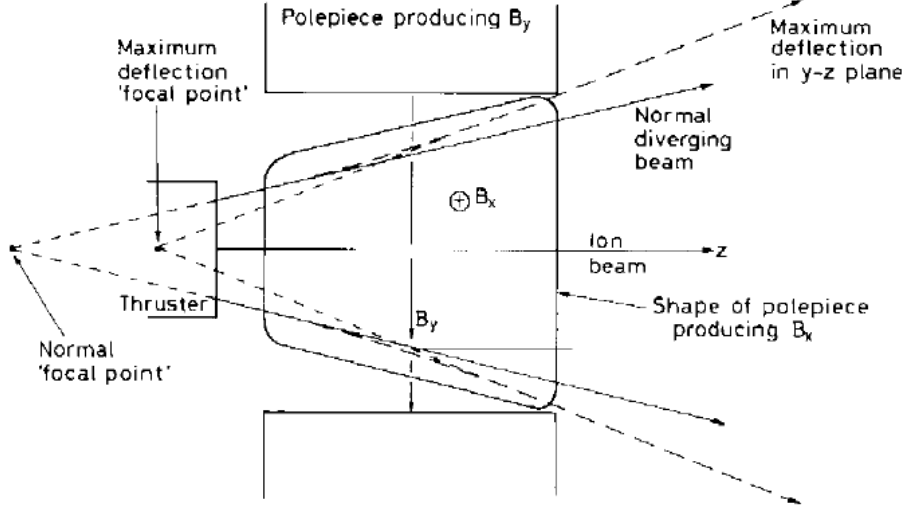


Figure 2.5: External magnetic deflection configuration [34].

The ions crossing the region of the applied magnetic field B_x with uniform velocity v_z will move in an arc of a circle of gyro-radius R in y direction, in according to Lorentz force F

$$R = \frac{m_i v_z}{q B_x} \quad \vec{F} = q(\vec{v} \times \vec{B}), \quad (2.1)$$

where m_i is the ion mass and q is the elementary charge. This cyclotron motion continues until the beam exits the field region of length L . Thus, the deflection angle α is given by

$$\sin \alpha_y = \frac{L}{R} \quad B_x = \frac{m_i v_z}{q L} \sin \alpha_y. \quad (2.2)$$

In order to achieve the deflection angle $\alpha_y = 8^\circ$ in y for an ion thruster operating at $v_z = 30000$ m/s ($I_{sp} \approx 3000$ s), the application of the magnetic field B_x of 380 Gauss is needed for a distance of $L = 15$ cm.

However, in the ion thrusters the charged particles are not ejected with the same velocity, since different phenomena like collisions with other particles (ions, electrons and neutrals) occur close to the engine exit. Hence, the charged particles in the thruster are usually described by a Maxwellian velocity distribution function. Therefore, each particle moves with a different velocity and the deflection plume angle α depends on its velocity.

Moreover, the relative position of the neutraliser with respect to the applied magnetic field, should be studied too, since the electrons are much lighter than ions. Low magnetic field strength are needed to fully-magnetize the electrons. For example, the electrons moving with their thermal velocity ($T_e = 1$ eV) through a magnetic field $B_x = 380$ Gauss

of the configuration in Figure (2.5), will move with gyro-radius

$$R_e = \frac{m_e v_{te}}{q B_x} = 10^{-4} \text{ m.} \quad (2.3)$$

Such small Larmor radius suggest that the electrons streamlines coincide with magnetic lines, and thus, they will move in the direction x , while the ions are deflected in y .

The simplest way to generate the uniform magnetic field in transversal direction with respect to the thruster axis, is that of employing at least two rectangular coils arranged in parallel planes. In fact, such a device has been proposed and patented in [49], and it is showed in Figure (2.6). In order to take care of the plume divergence the coils can be arranged with a slight angle to each other. By controlling the current flowing in the coils the necessary strength of magnetic field \vec{B} is created and the plasma beam crossing it with velocity \vec{v} is deviated in $\vec{v} \times \vec{B}$ direction. Thus, when an arrangement of four rectangular coils are used and by controlling the current in all four coils, the plume can be deviated in any azimuthal desired direction.

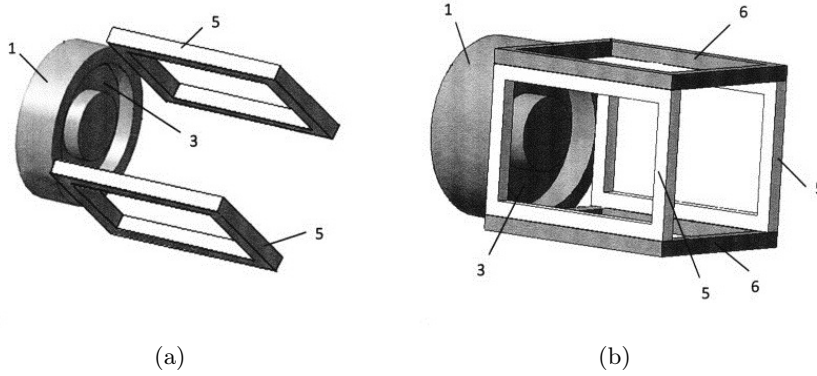


Figure 2.6: Arrangement of two (5) and four (6) rectangular coils for thrust vectoring mounted on a SPD-100 [49].

Preliminary design of this device for the HET SPD-100 suggests to select the frame length, width and the distance between planes 14 cm, 11 cm and 11 cm, respectively. Experimental investigation showed that vector angles of 5° in all directions are achievable with 200 turns of wire for each coil. Regarding the neutralization the low energy electrons will be trapped inside the beam of heavy ions and will follow their trajectory [49]. Such affirmation is to be verified by means of full-PIC simulations or experiments.

Although, the thrusters with magnetized plumes can be vectored by means of externally applied magnetic field. Those engines have a magnetic nozzle (MN) configuration, which consists of an axisymmetric convergent-divergent magnetic field that guides the expansion of a hot plasma to form a supersonic jet: ions gain axial kinetic energy at the expanse of electron internal energy thanks to the mediation of the self-consistent electric field [51]. Thus, both ions and electrons are fully-magnetized and move along the magnetic lines till

the plasma detaches from them due to demagnetization and inertia. The MNs are present in the Helicon plasma thrusters (HPT), the applied-field magneto-plasma-dynamic thruster (AF-MPD), electron-cyclotron-resonance thruster (ECR) and the variable specific impulse magneto-plasma-rocket (VASIMR). A non-symmetric MN configuration allows to deflect the plasma jet laterally in any direction to control the thrust vector. According to this line of thought, some concepts have been proposed that allow to change the direction of thrust vector by changing the direction of the magnetic lines of the magnetic nozzle.

The invention [52] discloses a magnetic nozzle composed of a permanent magnet arranged in front of a plasma flame-spraying nozzle and a plurality of non-concentric coils, which are arranged at the back of the nozzle and form a double-magnetic mirror tube. The proportion of current on the plurality of non-concentric coils when the plasmas are released from the magnetic nozzle is adjusted, so that the vector direction of the external magnetic field deviates from the central axis of the thruster, so as to guide the flow direction of external plasmas and further to change the thrust vector direction. The scheme is illustrated in Figure (2.7).

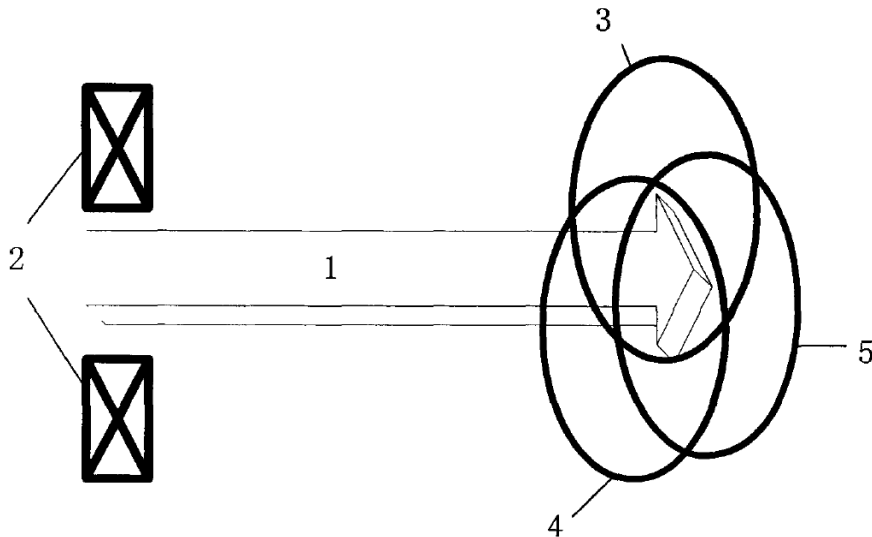


Figure 2.7: Vector magnetic nozzle composed by accelerated plasma plume (1), permanent magnets (2) and three non-concentric coils capable of controlling the thrust vector (3-4-5) [52].

A magnetically steerable helicon double layer thruster (MS-HDLT) is proposed too [53]. The configuration comprises an additional large external transverse coil perpendicularly oriented to the thruster axis and located on one flank of the thruster. However, in order obtain the steering in any azimuthal direction another additional transverse solenoid is needed. The steering of a magnetic nozzle of an helicon plasma thruster by means of two solenoids in a Helmholtz configuration attached to the engine exit is presented in [54]. This system was found to be capable to deflect the magnetic nozzle, but the divergence of the magnetic lines was increased significantly. Moreover, these devices may affect the internal

plasma dynamics and the efficiency of the thruster.

A similar invention to [52], but with three or more non-aligned conductive coils located at the outlet of the thruster, is the Vectorial Magnetic Nozzle (VECMAN) [50]. The system makes use of no moving parts or electrodes, for obtaining thrust vectoring capability in space plasma thrusters. It consists of $N \geq 3$ intertwined magnetic coils which are tilted at an angle α with respect to the axis of the thruster, and precessed an angle $2\pi/N$ with respect to each other to create a rotational-symmetric configuration.

Physically, a VECMAN device can be realized by winding simultaneously the N coils on a circular spool, resulting in a set of interwoven elliptical coils, or by intertwining rigid circular coils of slightly different radii or slightly offset from the axis into that position. Both constructions are shown on the left and right in Figure (2.8), respectively. By controlling

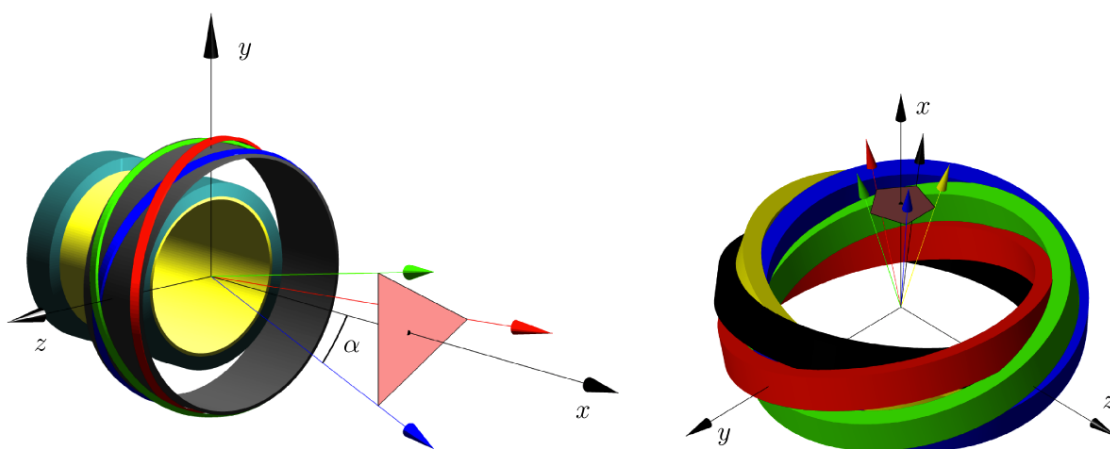


Figure 2.8: Left: Sketch of a VECMAN constructed with $N = 3$ elliptical coils tilted at $\alpha = 15^\circ$ placed at the exit section of a HPT-like plasma source. Right: A configuration made of $N = 5$ and $\alpha = 15^\circ$ interlocked intertwined circular coils slightly offset from the origin of coordinates [51].

the electric current on each coil, it is possible to create an orientable 3D magnetic field. The principles are the following:

- If all coils carry the same electric current, the system generates a magnetic nozzle whose axis coincides with the axis of the thruster. The magnetic field in this case is near-axisymmetric, with small asymmetries becoming important only close to the metal of the coils. A larger α and a lower N increase the asymmetry and reduce the usable MN radius for the plasma.
- By using different current values for each coil, it is possible to break the symmetry and reorient the axis of the MN. If all the electric currents on the coils have the same sign, the axis of the MN can be oriented in any direction within a reference N -polygonal angular space, where the maximum deflection angle (at the vertices of this polygon) is α . For example, with $N = 5$ the angular place is a pentagon. By inverting the

sign of some of the electric currents on the coils it is possible to generate deflections beyond that N-polygonal space, at the cost of a higher total electric current for the same field strength at the origin, and a higher asymmetry in the MN periphery.

The VECMAN design is placed near or at the exit plane of the plasma thruster and can be tailored to produce a deflection up to 15° [55]. It controls the shape and intensity of the magnetic field downstream without affecting the internal plasma dynamics and the internal plasma dynamics. It can be applied to any MN-based thruster, as well as other thrusters without an applied magnetic field, such as self-field MPD and GIT.

The concept has not been tested yet, the simulations with the fully-magnetized plasma expansion suggest thrust deflections of 5° - 10° [51].

Nevertheless, when the the device concepts is applied to the plasma thrusters with magnetized plumes some drawbacks might be identified. The total current flowing in the TVC coils must be capable to generate high enough magnetic field to magnetize and accelerate the plasma plume. Every coil is powered with a direct current independently and controllably, what requires delicate and sophisticated electronic components. This generates high power consumption and heat dissipation.

Chapter 3

Plasma Physics on Computers

3.1 Introduction to Plasma Physics

A plasma is a collection of free charged particles (ions and electrons) moving in random directions that is, on the average, electrically neutral. In other words, let us assume to grab some plasma (see Figure (3.1)). As long as the radius of this volume is larger than a certain characteristic length (called the Debye length, λ_D), the collection will contain approximately equal amount of positive (from ions) and negative (from electrons and negative ions) charge. The ratio of ionized particles to neutral atoms is the ionization fraction. In electric thrusters, about 90% of the working gas is ionized [6]. Plasmas were first introduced to describe partially ionised gas in [56].

Plasmas are often called a fourth state of matter and a simple discharge example is shown schematically in Figure [4]. The scheme is built with a voltage source that drives current through a low-pressure gas between two parallel electrodes. The gas between these two plates "breaks down" to form a plasma characterized by a fractional ionization given by

$$\chi_{iz} = \frac{n_i}{n_g + n_i} \quad (3.1)$$

Some more details of discharges and plasma generation can be found in [4].

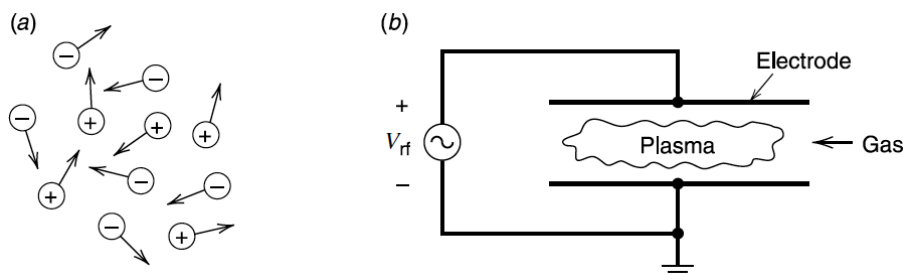


Figure 3.1: Schematic view of a plasma (a) and a discharge (b) [4].

Therefore, a plasma physics studies plasma behavior through experiments, theory and

simulation, which are needed to study collective and kinetic effects, especially in a non linear development. These collective phenomena, that a plasma displays, shows correlations on long range path between different particles and waves. This comes out when a large particle number is considered and when they come out in unusual way waves, instabilities and phenomena that convert energy from one source to another may be observed. For example electrostatic energy can be converted to a particle acceleration. All these events happens throw collective effects of plasma.

Modeling of plasmas is complicated by the presence of external and self-induced electromagnetic fields, inter-particle interactions, presence of solid objects, and the different characteristic time scales at which ions and electrons propagate.

The plasma characteristic frequency can be defined as follows:

- Electron plasma frequency which represents a sinusoidal electrostatic oscillation of the electron cloud with respect to the ion cloud at natural frequency and it is the shortest frequency that can be observed in a plasma

$$\omega_{pe} = \sqrt{\frac{n_e q^2}{m_e \epsilon_0}}. \quad (3.2)$$

- When the assumption of infinite mass ions in not made, the ions also move slightly with the oscillation natural frequency

$$\omega_{pi} = \sqrt{\frac{n_i q^2}{m_i \epsilon_0}}. \quad (3.3)$$

- Thus, the plasma frequency is

$$\omega_p = \omega_{pi} + \omega_{pe} \quad (3.4)$$

and for $m_i \gg m_e$, $\omega_p \approx \omega_{pe}$.

The electron plasma frequency is associated with a Debye length λ_{De} , length within which the charge is screened with thermal motion of electrons:

$$\lambda_{De} = \frac{v_{th}}{\omega_{pe}} = \sqrt{\frac{\epsilon_0 k_B T_e}{q^2 n_e}} \quad (3.5)$$

When the particle's self-induced magnetic fields are important, a skin depth defined and represents a distance where electromagnetic waves are screened

$$\lambda_{skin} = \frac{c}{\omega_{pe}}. \quad (3.6)$$

The longest frequency in a plasma is gyration or cyclotron frequency

$$\omega_c = \frac{qB_0}{m_e} \quad (3.7)$$

Hence, for a characteristic plasma the time scales are found to be in a typical ordering (see Figure (3.2)):

- t_{pe} plasma time for electrons;
- t_{ce} electron cyclotron time;
- t_{pi} plasma time for ions;
- t_{ci} ion cyclotron time;
- t_a Alfven wave time;
- t_{cs} ion sound period;
- t_{ei} electron-ion collision time.

where in a low frequency regime are found t_a , t_{cs} and t_{ei} .

The length scales of the plasma associated with time scales follow this ordering:

- λ_{De} Debye length;
- ρ_e Larmor radius of electrons;
- $\lambda_{skin,e}$ skin depth of electrons;
- ρ_i Larmor radius of ions;
- $\lambda_{skin,i}$ skin depth of ions;
- L is the scale of the system where scale gradients are important.

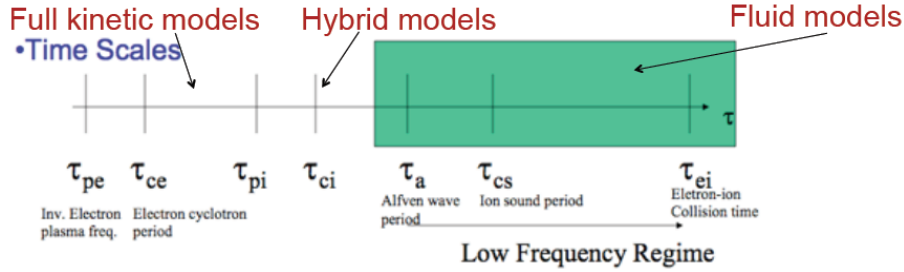


Figure 3.2: Time scales ordering for a general plasma.

It is obviously impossible in the general case to write and solve the system of momentum equation of all the particles in the plasma. Therefore, different numerical models have been introduced: kinetic, fluid and fluid-kinetic.

The fluid models are applicable in a low frequency regime and in order to simulate short scales a full kinetic model is necessary. There is also an intermediate regime where Hybrid simulations are applicable and in which electrons are treated as fluid and ions are treated as kinetic particle. The fluid models are good to predict the velocity of a plasma at a given position and the velocity is single valued. As far as fluid is concerned two counter-streaming beams are not moving at all as their average velocity is zero. However, two

counter-streaming beams still have lots of free energy that can be tapped. So a single fluid model is not capable to capture these phenomena. In a multi-fluid model a single sub-fluid is still allowed to have one velocity and two counter-streaming beams start to interact and some particle turn around the beam and an extra sub-fluid must be introduced with a different velocity in the same place. Thus, kinetic are very good for multi-valued velocity distribution functions.

In order to speed up the calculation, simplifying assumptions are generally taken to match the problem at hand. In literature several papers can be found using fluid model for electrons, assuming the Boltzmann relationship, in the simulation models of ion thruster plumes [29], [57], [58]. In this way simulation model then consists of only the heavy particles, ions and neutrals. This simplification has a tremendous impact on the computational speed, since the time integration can be performed on the much larger ion time scale.

3.2 Collisionless plasma

The plasma plumes of ion thrusters are characterized by low plasma densities. At low density, plasma behaves more like a collection of discrete particles, than a single continuous fluid. High-density plasmas are simulated using the extension of computational fluid dynamics into electromagnetics, magnetohydrodynamics.

A collisionless laboratory plasma is characterized by $N_D \gg 1$, where

$$N_D = n\lambda_D^3 \quad (3.8)$$

is the number of particles sitting in a Debye cube, which can be explained by another characterization of plasma. Since the physical behaviour of a plasma is one of electrons and ions moving in their Coulomb fields with sufficient kinetic energy to inhibit recombination:

$$\frac{KE}{PE} \gg 1, \quad (3.9)$$

where KE is the thermal kinetic energy and PE is the microscopic potential energy. To be noticed that the requirement $KE \gg PE$ may be satisfied at $N_D = 10$ [26].

Moreover, the larger is N_D the less collisional is plasma. In order to explain this concept let us consider a charged particle around other charges which will be attracted or repelled depends on its charge. So, the particle feels the other charges. When there are more charges, every of them will give a contribute to a particle and some of them will be cancelled. Hence, the more charges a particle has around, the easier will be to move around, since the average contribution of pull and push will be balancing out. It means when $N_D \gg 1$ the individual particle effect is not important and the collective effect is dominant. Hence, a collisionless system has a very large number of particles in Debye cube.

The second characterization of a collisionless plasma is also related to N_D through

$$\frac{\nu}{\omega_{pe}} \approx \frac{\ln N_D}{N_D} \ll 1 \quad (3.10)$$

Furthermore, in a collisionless plasma the mean free path is large and it means the plasma behaves at wavelength longer than the Debye length

$$L \gg \lambda_{De}. \quad (3.11)$$

This description can be realized by use of models with, for example, $L = 50\lambda_D$ [26].

The difference from a laboratory plasma is that simulations proceed discontinuously in time step by step, using digital rather than analogical computations. However, the numerical methods on which the code is based must provide sufficient accuracy and stability to make the simulations useful through many characteristic cycles of the plasma. Moreover, the temporal grid must be fine grained to follow the plasma with acceptable accuracy and stability too.

3.3 Fully-Kinetic Methodology

A microscopic state of a plasma at time t is defined by an exact particle distribution density of a kind s :

$$N_s(\vec{x}, \vec{v}, t) = \sum_{i=1}^{N_s} \delta(\vec{x} - \vec{x}_i(t)) \delta(\vec{v} - \vec{v}_i(t)) \quad (3.12)$$

which is a six-dimensional phase space equation [59]. This distribution describes the position \vec{x} and the velocity \vec{v} of each individual particle at the time t . The 6 coordinates (x, y, z, u, v, w) and the time coordinate are all independent. It means that for a particle i with coordinates (\vec{x}_i, \vec{v}_i) at any time t , the density will be one at point (\vec{x}_i, \vec{v}_i) of phase space and zero at any other point. Mathematically, this property is described by a δ -function, and hence, it generates a spike distribution function with a very noisy density. The total number of particles is obtained by integrating $N_s(\vec{x}, \vec{v}, t)$ over the position and velocity phase.

From the continuity equation in phase space with a few mathematical operations the Klimontovich equation is obtained

$$\frac{\partial N_s}{\partial t} + \vec{v} \cdot \nabla_x N_s + \frac{\vec{F}}{m} \cdot \nabla_v N_s = 0, \quad (3.13)$$

where the nabla operators ∇_x and ∇_v are the gradients in phase space and \vec{F} is the force to which particles are subject. This equation is the basis of the kinetic description of a plasma from a microscopic point of view and represent an exact description of all particles of the plasma. Hence, all the trajectories and all the positions are included. However, it is very difficult to make direct use of the Klimontovich equations, since it is exact and contains too many details [60].

Normally, a dynamic spikey distribution function $N_s(\vec{x}, \vec{v}, t)$ is substituted with a smoothed distribution function $f_s(\vec{x}, \vec{v}, t)$, representing its ensemble average over the six-dimensional phase space of the particles of a population s . A full mathematical description is provided in [59]. The averaging operation leads to the Boltzmann's equation:

$$\frac{\partial f_s}{\partial t} + \vec{v} \cdot \nabla_x f_s + \frac{q}{m} (\vec{E} + \vec{v} \times \vec{B}) \cdot \nabla_v f_s = \left(\frac{\partial f}{\partial t} \right)_{collisions}. \quad (3.14)$$

which provides a description of a plasma for a smoothed particle distribution function. The right hand side represents the effect of collisions.

In order to consider the self consistent electro-magnetic fields of a plasma, it is necessary to couple the Boltzmann's equations (3.14) with the Maxwell's system of equations:

$$\begin{cases} \nabla \cdot \vec{E} = \frac{\rho}{\epsilon_0} \\ \nabla \times \vec{E} = -\frac{\partial \vec{B}}{\partial t} \\ \nabla \cdot \vec{B} = 0 \\ \nabla \times \vec{B} = \mu_0 \left(\vec{J} + \epsilon_0 \frac{\partial \vec{E}}{\partial t} \right) \end{cases} \quad (3.15)$$

where ρ and \vec{J} are the charge density and the current density in the plasma, respectively, and the permittivity and permeability of free space are indicated with ϵ_0 and μ_0 , respectively.

The charge density is

$$\rho = \sum_s q_s n_s = e(Zn_i - n_e) \quad (3.16)$$

where q_s is the charge state of species s , Z is the charge state, n_i is the ion number density, and n_e is the electron number density.

The current density is

$$\vec{J} = \sum_s q_s n_s v_s = e(Zn_i v_i - n_e v_e), \quad (3.17)$$

where v_i and v_e are the electron and the ions velocities, respectively.

When effects of collisions are ignored ($N_D \gg 1$), the Boltzmann's equation (3.14) coupled with Maxwell's equations (3.15), becomes the Vlasov-Maxwell system of equations with a self-consistent electro-magnetic fields for a plasma (3.18), studied first by Vlasov [61]:

$$\begin{cases} \frac{\partial f_s}{\partial t} + \vec{v} \cdot \nabla_x f_s + \frac{q}{m} \left(\vec{E} + \vec{v} \times \vec{B} \right) \cdot \nabla_u f_s = 0 \\ \nabla \cdot \vec{E} = \frac{\rho}{\epsilon_0} \\ \nabla \times \vec{E} = -\frac{\partial \vec{B}}{\partial t} \\ \nabla \cdot \vec{B} = 0 \\ \nabla \times \vec{B} = \mu_0 \left(\vec{J} + \epsilon_0 \frac{\partial \vec{E}}{\partial t} \right) \end{cases} \quad (3.18)$$

The fully-kinetic methods solve a system of equations (3.18), which is a six-dimensional for a 3D problem. By the way, even for the EP problem, in which the effects of speed of light are ignored and only electric fields and potentials are dealt, the fully-kinetic method is feasible only for low dimensional studies.

3.4 Particle-In-Cell Methodology

Particle-In-Cell (PIC) is a technique commonly used to simulate motion of charged particles, or plasma on a computer. This method was introduced in the late 1950's and early 1960's, and the basics of the technique have not really changed. However, what has significantly changed is the computer power. Only in the last ten years powerful enough computers became available and it was observed that developments in computers have stimulated interest in these topics which allowed to simulate large enough systems to observe phenomena that were not expected. Today, Particle-In-Cell methodology gained more importance in research of phenomena such as solar wind propagation, or analysis of electric thruster plumes.

The PIC method uses computational particles, called macro-particles, to represent the real ions, electrons and neutrals. However, instead of computing the Coulomb force or solving Vlasov-Maxwell system of equations (3.15) directly, it is more practical to solve equations (3.15) evolving a lot of individual particles modeled as as macro-particles and moved with self-consistent electro-magnetic fields that are known on a grid. The macro-particles represent the characteristics of the these equations and the number of particles is concerned along the characteristics, so each particle is a solution of this system. Thus, the particle-in-cell method discretizes the particle distribution functions with a finite number of macro-particles.

Charged particles interact with each other by attracting particles of opposite charge and repelling those with the same charge by the Coulomb force, given by

$$\vec{F} = \frac{1}{4\pi\epsilon_0} \frac{q_1 q_2}{r^2} \vec{r}_{12}. \quad (3.19)$$

Conceptually, one might ask why not simulate plasma by taking a collection of particles representing the real physical ions and electrons and directly compute this force? This method is called Particle-Particle (PP), since it directly uses Coulomb's law to calculate the electrostatic force between particles and thus eliminates the constraints on mesh resolution and domain size of the Particle-In-Cell method. A collisionless plasma may also be simulated using a Particle-Particle (PP) model [62]. A PP model does not use a mesh and calculates the electrostatic forces on particles directly from the Coulomb's law between each particle pair. It is well understood that, in general, the PP method is not as efficient as PIC because the computing time of PP scales as $o(N^2)$, where N is the number of macroparticles used in the simulation [62]. However, because the PP method eliminates the requirements on mesh resolution and domain size and the need for an iterative field solve, it may provide an attractive alternative to PIC for those applications in which the total computational time is dominated by that of the field solver. The application of the PP method to simulate ion beam neutralization was explored in [28]. On the other hand, by computing directly forces between particles the solution will present a stochastic noise, since the simulation will never contain enough particles to represent what actually the nature does.

The force acting on the particles is given by the Lorentz force

$$\vec{F} = q(\vec{E} + \vec{v} \times \vec{B}) \quad (3.20)$$

and the motion of each particle is governed by Newton's Second Law

$$\begin{aligned}\frac{d\vec{v}}{dt} &= \frac{\vec{F}}{m} \\ \frac{d\vec{x}}{dt} &= \vec{v},\end{aligned}\tag{3.21}$$

which is a problem scaled as $o(N)$. Clearly, it is not computationally feasible to simulate every physical ion, electron or neutral since in a thruster plume simulation there are several tens of million of real particles. The ratio of real particles per macro-particle is called the specific weight.

A typical evolution cycle of a PIC code is illustrated in Figure (3.3). At each time step the code solves for the fields from particles and then moves particles (in a three-dimension code up to 10^6 particles are processed at each time step). The loop iterates until maximum number of time steps is achieved or until simulation reaches steady state.

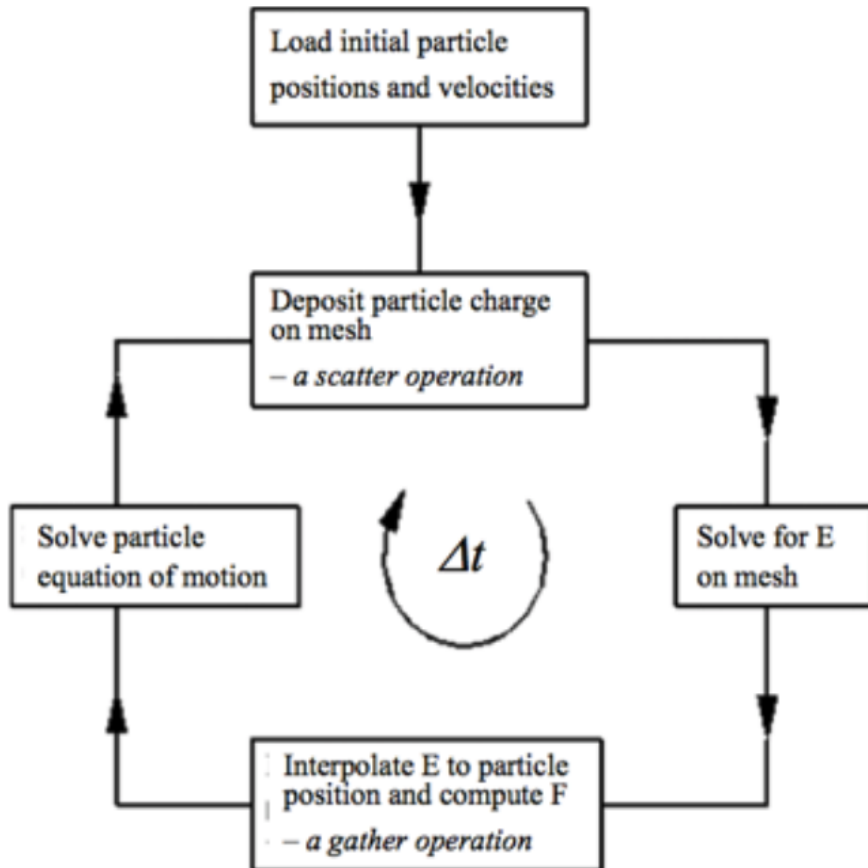


Figure 3.3: A typical cycle in a particle simulation code.

3.4.1 Computation of Charge Density

The simulation cycle starts at $t = 0$ with some appropriate initial conditions on the particle positions and velocities which are put on the grid. This deposition is also called a scatter operation. The ties to the fields quantities are made by calculating the charge and current densities on the grid. This calculation is done through *weighting* to the grid points that is dependent on particle position.

The cycle starts with some particles deposited on the grid. The simplest way is to use the zero-order weighting scheme which corresponds to the *nearest-grid-point* deposition. According to this method if the particle falls in a particular cell, that particle is in the cell and its charge is deposited to the grid location. This is the simplest and the fastest method can be done and the price to pay is a very noisy solution, since if the particle moves a little bit across the grid cell, it suddenly shifts its charge to another cell and this will introduce a spike in current which radiates electromagnetic waves in EM codes and in ES codes it will cause very noise fluctuations in electric field.

In order to reduce the noise in the solution when low order shape function is used, it is suggested to use more particles. Hence, the fluctuations in the charge deposition will get suppressed and the distribution of charge will get smoother.

A better approach is a first-order weighting, or *cloud-in-cell*, according to which a particle has a square shape in which the charge of a particle is uniformly distributed. Whichever part falls in a particular grid will get deposited in that grid. This generates a smoother of charge deposition and field fluctuations. This reduces the noise in the solution.

Higher order shapes by use of quadratic and cubic splines are also available. The increase of the order of the shape function usually reduce the noise in solution but at the cost of more computation.

3.4.2 Computation of Field Equations

The electric and magnetic fields on the grid are obtained from the charge and current densities solving Maxwell's equation in a general case. However, in electric space propulsion the effects of speed of light are ignored and only electric fields and potentials are dealt

$$\nabla \times \vec{E} = \frac{\partial \vec{B}}{\partial t} \approx 0. \quad (3.22)$$

Hence, the particle self-induced magnetic fields become static and the problem is electrostatic

$$\vec{E} = -\nabla V. \quad (3.23)$$

Let us consider a one dimension problem in x , the differential equations to be solved are

$$\begin{aligned} \vec{E} = -\nabla V &\rightarrow E_x = -\frac{\partial V}{\partial x} \\ \nabla \cdot \vec{E} = \frac{\rho}{\epsilon_0} &\rightarrow \frac{\partial E_x}{\partial x} = \frac{\rho}{\epsilon_0} \end{aligned} \quad (3.24)$$

By combining these two equation the Poisson's equation is obtained

$$\nabla^2 V = -\frac{\rho}{\varepsilon_0} \quad \rightarrow \quad \frac{\partial^2 V}{\partial x^2} = -\frac{\rho}{\varepsilon_0} \quad (3.25)$$

which can be discretized with finite difference with central differencing on one dimension grid uniformly spaced showed in Figure (3.4).

$$\frac{V_{j+1} - 2V_j + V_{j-1}}{(\Delta x)^2} = -\frac{\rho_j}{\varepsilon_0} \quad (3.26)$$

and for the electric field

$$E_j = \frac{V_{j+1} - V_{j-1}}{2\Delta x}. \quad (3.27)$$

The discretized equation for potential (3.26) can be written in matrix form and by using

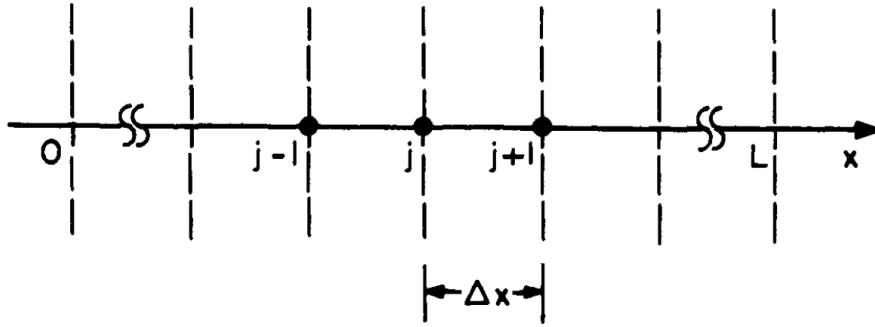


Figure 3.4: One dimensional numerical grid uniformly spaced [26].

the known boundary conditions, there will be as many equations as unknowns; thus, the problem is solvable. One of the methods to solve this system is a discrete Fourier series for all grid quantities. A more detailed description is in [26].

Therefore, when the FFT method is used the number of floating point operations for the complete scheme scales as:

$$\alpha N_p + \beta N_g \ln N_g + \gamma N_g. \quad (3.28)$$

The expense of the operations is given by particles pushes at every step which is proportional to the number of particles N_p ; since the equations are evaluated on a grid, it goes with a number of grid points N_g and the Poisson's equation solve goes with $N_g \ln N_g$.

3.4.3 Computation of Equations of Motion

The next step in the ES-PIC algorithm is the interpolation of the electric field from the grid to the particles in order to apply the force at the particle by performing a weighting. To be noted that at this step the particles are scattered around within the grid. The interpolation is a gather operation where the charge is taken from the grids and put it back

to the particles. To ensure the momentum conservation the same interpolation technique must be used to compute the force on a particle as was used to perform the assignment of the particle charge to the mesh.

The integration of particle motion through a time Δt is commonly performed by using the Leap-frog method which is the second-order accurate method [63]. The name comes from the fact that times at which velocity and positions are known are offset from each other by half a time step, and this gives a second-order accuracy, and it is good method for conservation properties, for example, it can conserve the total energy.

First, the velocity is integrated through the time step and next, the position is updated. As such, the two quantities leap over each other. This idea is sketched in Fig (3.5).

The Newton's Second Law equations are replaced by the finite difference equations in

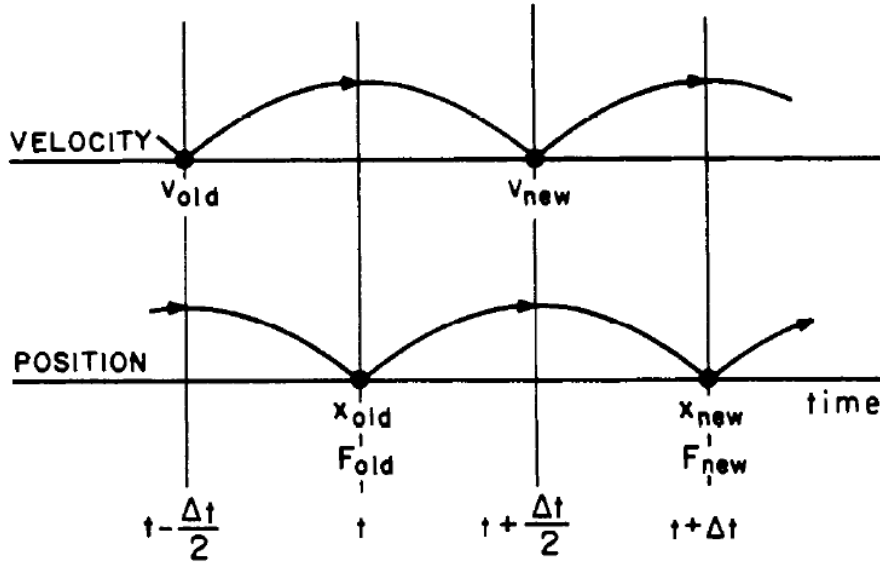


Figure 3.5: Leap-frog integration method showing time centering of force F while advancing v and of while advancing x .

explicit form

$$\begin{aligned} v^{k+\frac{1}{2}} &= v^{k-\frac{1}{2}} + \frac{F^k}{m} \Delta t \\ x^{k+1} &= x^k + v^{k+\frac{1}{2}} \Delta t \end{aligned} \quad (3.29)$$

The force has two parts,

$$\vec{F} = \vec{F}_{electric} + \vec{F}_{magnetic} = q\vec{E} + q(\vec{v} \times \vec{B}) \quad (3.30)$$

where the electric field \vec{E} is calculated from the particle and from the external source and the magnetic field \vec{B} is calculated only from the external source. The integration with a magnetic term can be performed with a Boris scheme [64].

After particles are moved to new positions, it is necessary to verify that all particles are still in the computational domain. Two boundary interactions are possible. The particles

can either exit the domain, or can collide with solid objects. Computational boundaries are either open (or absorbing, allowing particles to leave), reflective (elastically returning particles into the domain) or periodic (particles are transported to the opposite side of the domain). The reflective boundary is used to identify planes of symmetry. Details of particle-surface interaction, which can result in erosion of native material.

However, the time step Δt needs to satisfy numerical constraints as in every numerical method. In the leap-frog method this constraint can be illustrated with a simple harmonic oscillator, described by the second-order differential equation

$$\frac{d^2x}{dt^2} = -\omega_0^2 x. \quad (3.31)$$

The analytical solution for this equation is

$$x(t, t_0) = A(t_0) \cos \omega_0 t + B(t_0) \sin \omega_0 t. \quad (3.32)$$

Obviously, in numerical algorithm the time step cannot be larger than the period of the oscillation since the oscillation will be missed. In fact, if the finite-difference approximation of leap-frog method

$$\frac{dv}{dt} \rightarrow \frac{v^{k+\frac{1}{2}} - v^{k-\frac{1}{2}}}{\Delta t} = \frac{x^{k+1} - 2x^k + x^{k-1}}{\Delta t^2} \quad (3.33)$$

is substituted into a homogeneous equation of motion, the following equation is obtained:

$$\frac{x^{k+1} - 2x^k + x^{k-1}}{\Delta t^2} = -\omega_0^2 x \quad (3.34)$$

The last one can be solved by assuming solution of the form

$$x_t = A e^{-i\omega t} \quad (3.35)$$

where A is an initial value and ω is the unknown. If the last one is substituted into the homogeneous equation of motion, the equation

$$\sin\left(\omega \frac{\Delta t}{2}\right) = \pm \omega_0 \frac{\Delta t}{2} \quad (3.36)$$

is obtained. The plot for this solution is shown in Figure (3.6). It can be seen that for

$$\omega_0 \Delta t > 2 \quad (3.37)$$

real solution for ω becomes complex and numerical instability is observed which brings to the explosion of code, while for

$$\omega_0 \Delta t \ll 2 \rightarrow \omega \approx \omega_0, \quad (3.38)$$

as desired. The phase error is observed when

$$\omega_0 \Delta t < 2 \quad (3.39)$$

but the simulation will still work. In order to observe oscillations for some tens of cycles with acceptable accuracy the phase error suggest a choice of

$$\omega_0 \Delta t \leq 0.3 \quad (3.40)$$

Hence, since in a full-PIC code electrons are treated as particles, the fastest oscillation frequency in a plasma ω_{pe} must be resolved in order to avoid the code explosion. However, Δt limitation can be overcome by the leap-frog implicit formulation, what complicates the code considerably, but in practice it allows to overstep this constraints only by a factor of 2 or 3.

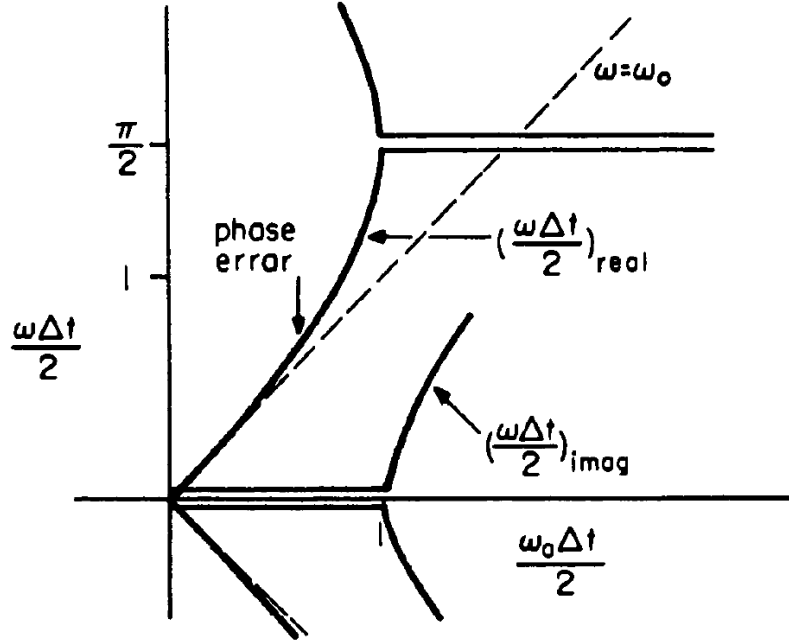


Figure 3.6: Solution for ω in terms of ω_0 for simple harmonic motion. Phase error is the difference between the numerical and exact frequency ω_0 [26].

3.4.4 Algorithm Output

The output from PIC codes includes various diagnostics which are printed out at particular time steps; some of them might be in form of snapshots, such as the spatial distribution of plasma parameters like potential, charge density, electron temperature, as well as particle data such as velocities and current densities. In addition, time-dependant output of global aggregate diagnostic data, such as total kinetic and potential energy of the simulation, is helpful in diagnosing code performance.

The loop repeats until some condition is satisfied. Simulations with continuous sources are run until a steady state is achieved. The steady state is characterized by the net number of particles in the simulation domain remaining constant between time steps. In

other words, the number of new particles generated by sources is balanced by the number of particles leaving the domain through the boundaries.

3.4.5 Restriction of Simulation Parameters

Time step

In an ES-Particle-In-Cell plasma simulation, the value of time step must satisfy these conditions:

- Courant condition (rectangular coordinate) according to which the time step depends on the resolution of the grid

$$dt < 1 / \sqrt{\frac{1}{dx_1^2} + \frac{1}{dx_2^2}} \quad (3.41)$$

with $\omega_{pe} = 1$ and $c = 1$

- Leapfrog time step limitation

$$\omega_{max} dt < 0.3 \quad (3.42)$$

where ω_{max} is the maximum frequency of the system.

- Particles do not have to move more than one cell per grid step

$$v_{max} dt < \min(dx_1, dx_2). \quad (3.43)$$

Resolution

Typically, in order to measure the space charge density the mesh requires to resolve a Debye length

$$dx \approx \lambda_{De} \quad (3.44)$$

and the resolution requires at least 4-9 particles per cells per species.

3.5 CST Particle Studio

CST Particle Studio (CST PS), part of Simulia, a Dassault Systemes brand, is a specialist tool for the fast and accurate analysis of charged particle dynamics in 3D electromagnetic fields. Powerful and versatile, it is suitable for tasks ranging from designing magnetrons and tuning electron tubes to modeling particle sources and accelerator components. It features three modules:

- The particle tracking solver can model the behavior of particles through static fields, and with the gun iteration, space charge limited emission.

- The particle-in-cell (PIC) solver, which works in the time domain, can perform both a fully consistent simulation of particles and electromagnetic fields, and electrostatic simulation (ES-PIC) in which Poisson's equation is solved to update the electrostatic fields defined at the spatial grid points in the simulation space.
- For relativistic applications, the wakefield solver can calculate how the fields generated by particles traveling at (or close to) the speed of light interact with the structure around them.

CST PS is integrated with the multi-purpose 3D EM modules of CST STUDIO SUITE, such as the CST EM STUDIO electro- and magnetostatic solvers and the CST MICROWAVE STUDIO eigenmode solver. It is fully embedded in the CST STUDIO SUITE design environment, thus benefiting from its intuitive modeling capabilities and powerful import interfaces. CST PS is based on the knowledge, research and development that went into the algorithms used in the MAFIA-4 simulation package. The powerful PIC solver can also make use of GPU computing, offering significant performance enhancements on compatible hardware. Further information can be found on the product's website [65].

Chapter 4

Code validation with One-Dimensional Analytical Model

In this chapter the one-dimensional space charge ion beam emission is discussed and *CST Particle Studio*'s ES-PIC solver was applied to validate the code by means of 1D analytical model which involves several obvious idealization. Similar approach was done by Wang and Lai [66] who simulated with full ES-PIC code the physics of non-neutralized ion beam emission from spacecraft to a low-density space plasma and compared results with one-dimensional analytical model. Instead, the space charge emissions in vacuum between two electrodes were studied.

The ion beam emitters are similar to ion thrusters in which heavy positive charges are accelerated by electrostatic forces within a biased grid to form a beam with a high velocity; usually the energy range is approximately kilo-electron volt energy corresponding to a couple of amperes of positive ion current. Then, the beam is neutralized by emitting electrons in order to avoid the spacecraft charging, and thus, the quasi-neutral plasma beam is formed with a little space charge effect based on the dynamics of heavy ions, usually Xe^+ .

4.1 One-Dimensional Analytical Theory of Space Charge Flow

The one-dimensional theory is based on the space charge flow of an ion beam in a diode in which charged particles are accelerated between two electrodes in a vacuum tube. In this case the neutralization is not provided and the positive space charge effects are formed. When the current density is low the charge flow is monotonic but at higher values of current density the space charge effects become important and if the initial velocity is zero the maximum density that can be transmitted is fixed by Child-Langmuir's law [5]. In case of non-zero initial velocity the potential profile may be non monotonic with a potential hump formed.

The solution for this problem follows the classical theory and it was first presented by Fay et al. [67] who considered an ion beam emitted from a plane electrode at $x = 0$ and received by a plane electrode at $x = L$. The situation is illustrated in Figure (4.1).The

initial beam particle kinetic energy is

$$qV_{bk0} = \frac{1}{2}mv_0^2 \quad (4.1)$$

and the emitting current density given by

$$J_0 = qn_0v_0 \quad (4.2)$$

In addition, the potentials at the electrodes are

$$V(0) = V_s \quad \text{and} \quad V(L) = 0. \quad (4.3)$$

The governing equations are the Poisson's equation, current continuity, and energy conservation equation:

$$\begin{cases} \frac{d^2V}{dx^2} = -\frac{qn}{\varepsilon_0} \\ n_b = \frac{J_0}{qv} \\ qV_{b0} = qV_s + qV_{bk0} = \frac{1}{2}mv^2 + qV \end{cases} \quad (4.4)$$

where qV_{b0} is the total beam particle energy and v_b is the particle velocity given by

$$v_b = \sqrt{\frac{2q}{m}(V_{b0} - V)} \quad (4.5)$$

and the ion been can be transmitted only when $V_{b0} > V$. Thus, the differential equation for the space charge flow problem becomes

$$\frac{d^2V}{dx^2} = -\frac{J_{b0}}{\varepsilon_0} \left[\frac{2q}{m}(V_{b0} - V) \right]^{-\frac{1}{2}} \quad (4.6)$$

The last one can be integrated

$$\left[\left(\frac{dV}{dx} \right)^2 \right]_{x_1}^{x_2} = \left[\frac{2J_{b0}}{\varepsilon_0} \sqrt{\frac{2m}{q}} \sqrt{V_{b0} - V} \right]_{V_1}^{V_2} \quad (4.7)$$

In this way it is possible to define a monotonic solution potential profile $V(x)$ characterized by

$$V_s > 0 \quad \text{and} \quad v_0 = 0 \quad \rightarrow \quad V_{b0} = V_s \quad \text{and} \quad \frac{dV}{dx} = 0 \quad \text{at} \quad x = 0 \quad (4.8)$$

The solution is a well-known Child-Langmuir law of space charge limited current between two plane electrodes

$$J_0 = \frac{4}{9} \sqrt{\frac{2m}{q}} \frac{\varepsilon_0 V_s^{3/2}}{L^2} \quad (4.9)$$

which represents a fundamental limit on the current which can be drawn across a give plane gap by a given potential difference [5].

However, the potential $V(x)$ can have a non-monotonic profile with a maximum at $x = x_m$ and $V(x_m) = V_m > 0$ which leads to a more general solution to Equation (4.7). By defining the dimensionless variables:

$$\hat{x} = \frac{x}{L}, \quad \hat{V} = \frac{V}{V_{b0}}, \quad \hat{J}_0 = \frac{J_0}{J_c}, \quad (4.10)$$

where J_c is the space charge limit current for a potential V_{b0}

$$J_c = \frac{4}{9} \sqrt{\frac{2m}{q}} \frac{\varepsilon_0 V_{b0}^{3/2}}{L^2} \quad (4.11)$$

Thus, the Equation (4.6) becomes

$$\frac{d^2 \hat{V}}{d\hat{x}^2} = -\frac{4}{9} \frac{\hat{J}_0}{1 - \hat{V}} \quad (4.12)$$

Integrating between \hat{x} and \hat{x}_m with $d\hat{V}/d\hat{x}(x_m) = 0$ leads to

$$\left(\frac{d\hat{V}}{d\hat{x}} \right)^2 = \left(\frac{4}{3} \right)^2 \hat{J}_0 \left(\sqrt{1 - \hat{V}} - \sqrt{1 - \hat{V}_m} \right) \quad (4.13)$$

And since $d\hat{V}/d\hat{x}$ has a different sign on each side of x_m

$$\begin{aligned} \frac{d\hat{V}}{d\hat{x}} &= \frac{4}{3} \sqrt{\hat{J}_0} \left(\sqrt{1 - \hat{V}} - \sqrt{1 - \hat{V}_m} \right)^{1/2} && \text{when } 0 < \hat{x} < \hat{x}_m \\ \frac{d\hat{V}}{d\hat{x}} &= -\frac{4}{3} \sqrt{\hat{J}_0} \left(\sqrt{1 - \hat{V}} - \sqrt{1 - \hat{V}_m} \right)^{1/2} && \text{when } \hat{x}_m < \hat{x} < 1 \end{aligned} \quad (4.14)$$

By integrating the following equation

$$\frac{d\hat{V}}{\left(\sqrt{\hat{V}_{b0} - \hat{V}} - \sqrt{\hat{V}_{b0} - \hat{V}_m} \right)^{1/2}} = \pm \frac{4}{3} \sqrt{\hat{J}_0} d\hat{x} \quad (4.15)$$

the solution becomes

$$\begin{aligned} \sqrt{\hat{J}_0} \hat{x}_m &= \left(\sqrt{\hat{V}_{b0}} + 2\sqrt{1 - \hat{V}_m} \right) \sqrt{\sqrt{\hat{V}_{b0}} - \sqrt{1 - \hat{V}_m}} && \text{when } 0 < \hat{x} < \hat{x}_m \\ \sqrt{\hat{J}_0} (1 - \hat{x}_m) &= \left(1 + 2\sqrt{1 - \hat{V}_m} \right) \sqrt{1 - \sqrt{1 - \hat{V}_m}} && \text{when } \hat{x}_m < \hat{x} < 1 \end{aligned} \quad (4.16)$$

where

$$\hat{V}_{b0} = \frac{1}{2} m v_0^2 \frac{1}{q V_{b0}} = 1 - \hat{V}_s \quad (4.17)$$

Thus, the solution becomes

$$\frac{1 - \hat{x}_m}{\hat{x}_m} = \frac{(1 + 2\sqrt{1 - \hat{V}_m}) \sqrt{1 - \sqrt{1 - \hat{V}_m}}}{(\sqrt{V_{bk0}} + 2\sqrt{1 - \hat{V}_m}) \sqrt{\sqrt{\hat{V}_{bk0}} - \sqrt{1 - \hat{V}_m}}} \quad (4.18)$$

Three different cases can be defined

$$\begin{aligned} \hat{V}_s &\geq 0, & 0 \leq \hat{x}_m < 0.5 \\ \hat{V}_s &\leq 0, & 0.5 < \hat{x}_m \leq 1 \\ \hat{V}_s &= 0, & \hat{x}_m = 0.5 \end{aligned} \quad (4.19)$$

The first two cases are illustrated in Figure (4.1).

However, in the limiting case $\hat{V}_m = 1$ when $V_m = V_{b0} = V_{bk0} + V_s$ the ion beam comes to a potential peak V_m at x_m with $v(x_m) = 0$. It means that some particles can be reflected back to upstream and others can be accelerated downstream the potential halt. Let us define the fraction of J_0 that can be transmitted through this potential barrier, the beam particle density becomes

$$\begin{aligned} n &= \frac{J_0}{qv} + \frac{(1-f)J_0}{qv} \quad \text{when } 0 < \hat{x} < \hat{x}_m \\ n &= \frac{fJ_0}{qv} \quad \hat{x}_m < \hat{x} < 1 \end{aligned} \quad (4.20)$$

The solution for this limiting case is

$$\sqrt{(2-f)\hat{J}_0\hat{x}_m} = \hat{V}_{bk0}^{3/4} \quad \sqrt{f\hat{J}_0(1-\hat{x}_m)} = 1 \quad (4.21)$$

Thus,

$$\frac{1 - \hat{x}_m}{\hat{x}_m} = \sqrt{\frac{2-f}{f}} \frac{1}{V_{bk0}^{3/4}} \quad (4.22)$$

To be noted that when the emitting current $J_0 > J_c$, the potential peak V_m operates as a virtual anode which means that the kinetic energy of flowing charge is not sufficiently high to overcome the potential hump, and thus, some charge flow backward and some forward [66].

Furthermore, Jahn [6] represented the potential profile in the region between accelerator and neutralizer for one-dimensional model of an ion thruster with a plasma source at potential V_0 , an accelerator at zero potential and a separation of x_a from the source. It was assumed that the beam was neutralized everywhere beyond a third plane, at Δx from accelerator, point from which the potential is zero. Thus, for a space-charge limited ion current the potential profile depends on J , V_0 and ratio of gap sizes $\Delta x/x_a$. The model is illustrated in Figure (4.2). It was observed that a duality in solutions exists and depends on mathematical admissibility of negative-flowing and positive-flowing ion

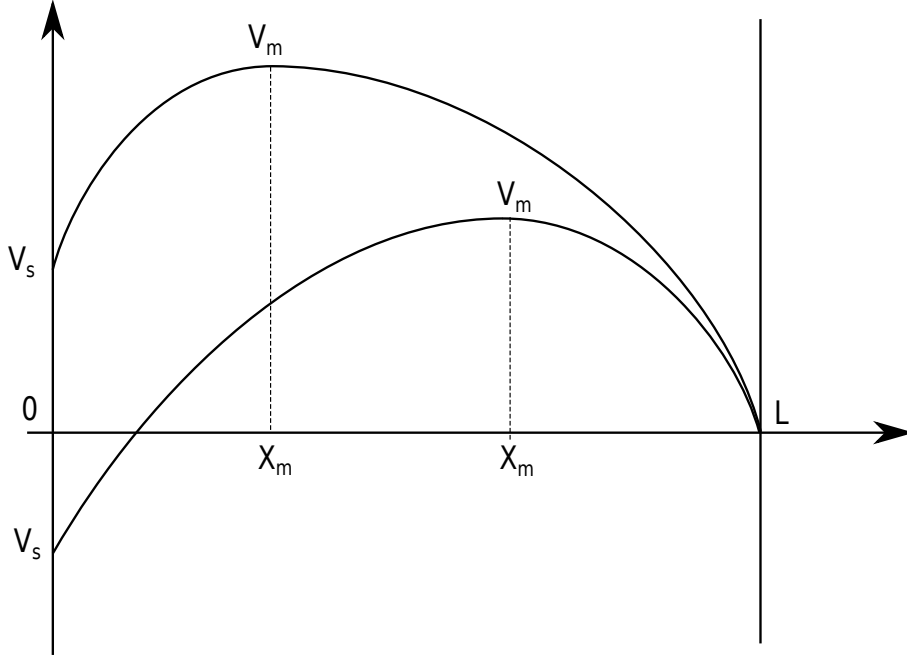


Figure 4.1: Non-monotonic potential profiles associated with one-dimensional non-neutralized ion beam emission between two plane electrodes.

currents. Physically, some fraction of ion beam may be reflected when the potential in the second gap rises to a value of V_0 and it would correspond to a beam-stalling condition.

If only positive-flowing current exists and $\Delta x/x_a$ is gradually increased from zero, $V(x)$ results to be symmetrical about $x_a + \Delta x/2$ where the potential profile reaches its maximum values V_m . The magnitude of V_m increases monotonically with Δx . This solution is represented in the Figure (4.3(a)). When $\Delta x/x_a = 2\sqrt{2}$, V_m reaches the value of $3/4V_0$ and beyond this point no solution involving only positive-flowing ion current exists. Thus, if negative-flowing current is admitted potential profile changes and a new asymmetric branch of solutions is available, each of which has a $V_m = V_0$ and some fraction R of the beam is reflected and returns to the source. It was found that for the position $\Delta x/x_a = 2\sqrt{2}$ the simple symmetric solutions cease and the maximum potential V_m is found to be at $x = 1.75x_a$ with $R = 0.77$ reflected positive current.

Moreover, when $\Delta x/x_a$ is increased from $2\sqrt{2}$ to ∞ , the asymmetrical profile is observed, but the fraction of the beam reflected increases from 0.77 to 1 and V_m is regressed to position $1.707x_a$ (see in Figure (4.3(b))).

Finally, physically it may be concluded that one-dimensional beam model must be neutralized at least within a distance of $2\sqrt{2}x_a$ after it leaves the accelerator grids. However, for a more elaborate three-dimensional neutralization models with ion beams of finite cross sections are necessary to derive the corresponding neutralization requirements.

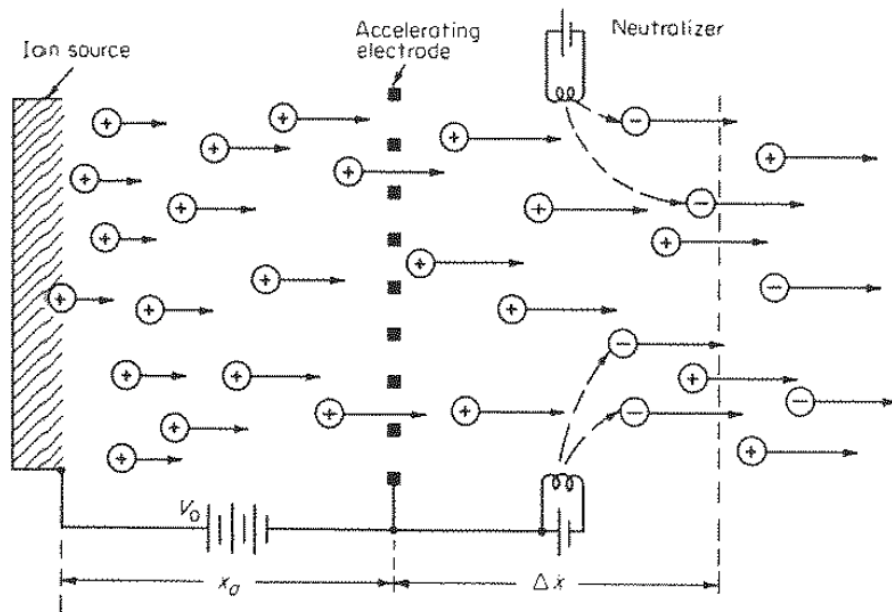
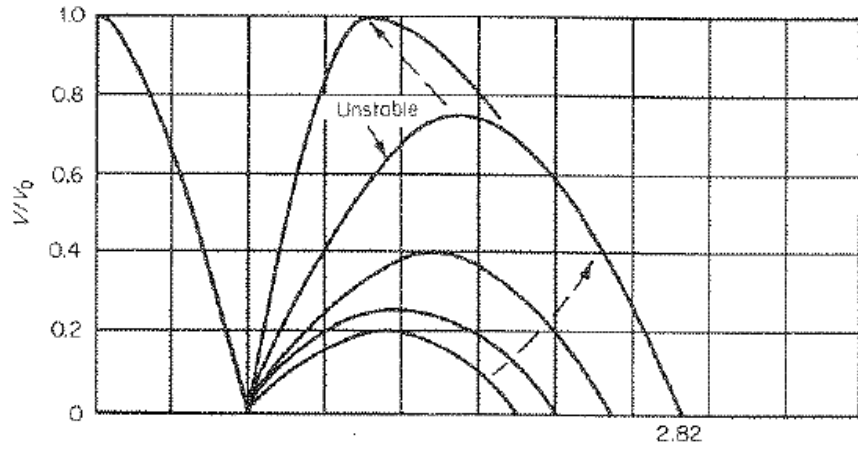
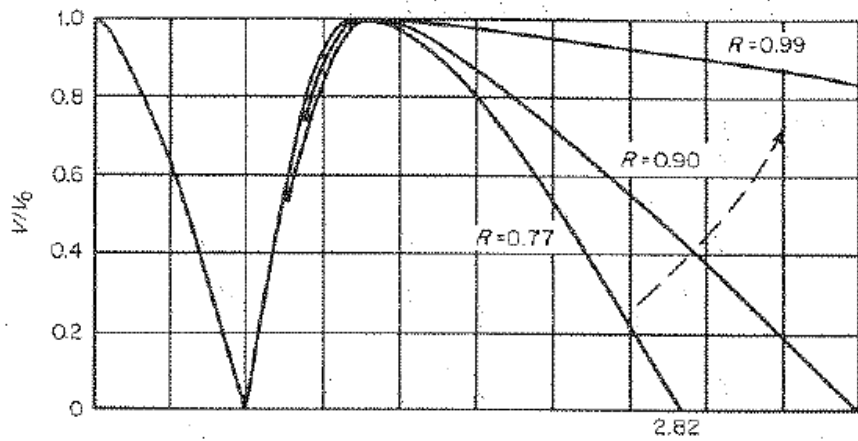


Figure 4.2: Neutralization of one-dimensional ion beam model [6].



(a)



(b)

Figure 4.3: Potential profiles for one-dimensional ion beam neutralized at distance Δx from accelerator grid [6].

4.2 Three-Dimensional Particle In Cell Simulations

4.2.1 Simulations setup

The ES-PIC code was applied to one-dimensional theory in order to validate it. The idea is to predict the position x_m of the potential hump and its maximum value V_m for different neutralization distance $\Delta x/x_a$. Moreover, it was also studied the influence of emission radius on the potential hump. The simulation setup is showed in Figure (4.4). The ion emitter is modeled as a circular conducting surface having a radius R_b and a fixed potential V_s relative to the ambient. All the other boundaries are taken to be open boundaries and the plane at z_{max} is set to be at $V = 0$. By changing the position of this plane it is possible to obtain different position, where the beam is neutralized. The ambient of the simulation is taken to be vacuum. The ion particles are injected in the simulation domain at every time step with initial velocity v_0 defined in Eq. (4.1) and the emission form an uniform cylindrical beam at the emitter surface exit with the current density J_0 defined in Eq. (4.2). When the particles hit the emitter or flow out the simulation domain, they are deleted from the simulation.

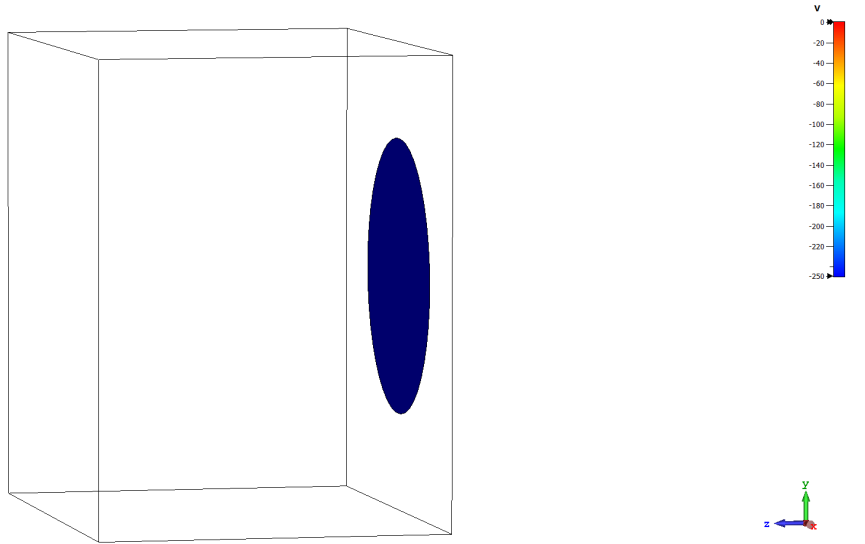


Figure 4.4: Simulation setup.

The emitter surface is set to $V_s = -250 V$, the initial kinetic energy is the beam ions is set to be

$$qV_{bk0} = \frac{1}{2}mv_0^2 = 1000 eV \quad (4.23)$$

and the density current is set to be

$$J_0 = qn_0v_0 = 1.84 \frac{A}{m^2}. \quad (4.24)$$

The acceleration gap from Child-Langmuir law given in Eq. (4.9) is given by

$$x_a = \sqrt{\frac{4}{9} \sqrt{\frac{2q}{m_i} \frac{\varepsilon_0 V_{b0}}{J_0}}} = 5.1043 \text{ cm} \quad (4.25)$$

where the ion mass is taken to be artificially $m_i = 100m_e$. The total energy of the beam at the emitter exit is

$$qV_{b0} = qV_{bk0} + qV_s = 750 \text{ eV}. \quad (4.26)$$

The simulation cases are summarized in Tab. (4.2). Please note that in three-dimensional simulations z axis corresponds to x axis of one-dimensional theory, so in this way for the simulations $z_a = x_a$. The number of grid cells N_z in z direction depends on the neutralization distance $\Delta z/z_a$, while $N_x = N_y = 171$ were kept constant. Hence, the total cells number N varied from 1×10^6 to 1.45×10^6 elements. Moreover, it was decided to have a uniform hexagonal mesh with $d_{cell} = 0.2$ cm in all three directions. The simulations time also depends on the domain in z direction but they were run until a steady state had been achieved, it means that the total number of particles in the simulation domain didn't vary in time. The time step is taken to be $dt = 1$ ns and this also ensures $v_0 dt \ll d_{cell}$. At every time step 40 emission points ejected 6241 particles from the emitter what leads to have the total number of particles in the domain, once the steady state is achieved, from 7.85×10^5 to 2.2×10^6 particles.

Case	$\Delta z/z_a$	R_b (cm)	N_z	T (ns)
A1	2	10	53	200
A2	$2\sqrt{2}$	10	74	240
A3	4	10	104	1200
A4	5	10	129	1200
A5	10	10	257	1200

Table 4.1: Simulation cases

4.2.2 Results and Discussion

From the simulation it is possible to obtain $V_{m,sim}$ and the position $x_{m,sim}$ on $x-y$ cutting plane through the emitter center. Then, the maximum potential $V_{m,sim}$ is substituted in the following equation to obtain $x_{m,1D}$.

$$\frac{1 - \hat{x}_m}{\hat{x}_m} = \frac{\left(1 + 2\sqrt{1 - \hat{V}_m}\right) \sqrt{1 - \sqrt{1 - \hat{V}_m}}}{\left(\sqrt{V_{bk0}} + 2\sqrt{1 - \hat{V}_m}\right) \sqrt{\sqrt{\hat{V}_{bk0}} - \sqrt{1 - \hat{V}_m}}} \quad (4.27)$$

The summary simulations results are reported in Table (4.2).

Case	$\Delta z/z_a$	R_b (cm)	$z_{m,sim}/z_a$	$V_{m,sim}$ (V)	$x_{m,1D}/x_a$	Error (%)
A1	2	10	1.38	70.86	1.37	1.25
A2	$2\sqrt{2}$	10	1.67	207.31	1.70	2.03
A3	4	10	2.06	462.71	2.24	7.92
A4	5	10	1.25	748.89	2.76	54.71
A5	10	10	1.17	740.12	5.50	78.68

Table 4.2: Simulation results and comparison with one-dimensional model.

In Figures (4.5) and (4.6) are reported the total number of particles in the simulation domain and the maximum potential \hat{V} on the $x - y$ cutting plane at different time steps, respectively. These two plots show that in all cases the simulations reached the steady-state, since from Figure (4.5) the number of particles in the simulation domains does not vary. It means that the emitted particles are equal to that removed from the boundaries. The maximum potential in time plot (4.6) shows that once the steady-state is reached the maximum potential equals or is limited by the total beam particle energy divided by q . Some oscillations are observed for cases A4 and A5.

The simulation results display ion density number and potential maps in Figures from (4.8) to (4.11) on a $x - y$ plane cutting through the emitter center.

In cases A1 and A2 the potential hump is well predicted, in fact the relative error is around 2%. The ion densities show that the beam in two cases is almost one-dimensional. However, when the neutralization distance is moved up to $\Delta z/z_a = 4$ in case A3 the potential hump $\hat{V} < \hat{V}_m$ and no back flow current is observed, while the potential profile is still similar to the previous two cases. For 1D theory a total reverse flow would occur, since the beam has not been neutralized within $\Delta z/z_a = 2\sqrt{2}$. The position of V_m is predicted within 8% and from ion density number a higher beam divergence can be observed.

In case A4 the neutralization distance ($\Delta z/z_a = 5$) is further increased and a potential peak is formed with $\hat{V}_m = 1$ at distance very close to the emission surface. This situation correspond to the virtual anode [66] in which the maximum potential reflects back the particles toward the emitter and only a small ion density flows downstream, since the particles lack kinetic energy. When the neutralization is imposed further downstream A5 at a double distance of the case A4, the situation is pretty the same, the virtual anode is formed. The potential profiles with virtual anode changes its concavity as it can be observed from Figure (4.7).

The one-dimensional theory provides a good prediction of the potential peak location for the cases with $R_b > \Delta z$. The motivation of this situation is attributed to the beam divergence, since within the distance $\Delta z = R_b$ the beam is approximately one dimensional. In three-dimensional situations the beams have the freedom to expand their cross section prior the neutralization, in response to the space-charge forces. In fact, this situation is observed in the case A4, the beam divergence is increased due the space-charge forces and the total current back flow is not observed. It means that compared to one-dimensional theory the neutralization requirements are less severe, as the beam was not neutralized

within a maximum distance of $2\sqrt{2}x_a$.

Finilizing, the neutralizer does not have to be placed within a few accelerator gap distance, as requested from one-dimensional calculations. Indeed, in practise the electron emitter is positioned father downstream, since some electrons tend to migrate upstream due to their low mass and high thermal velocity [7].

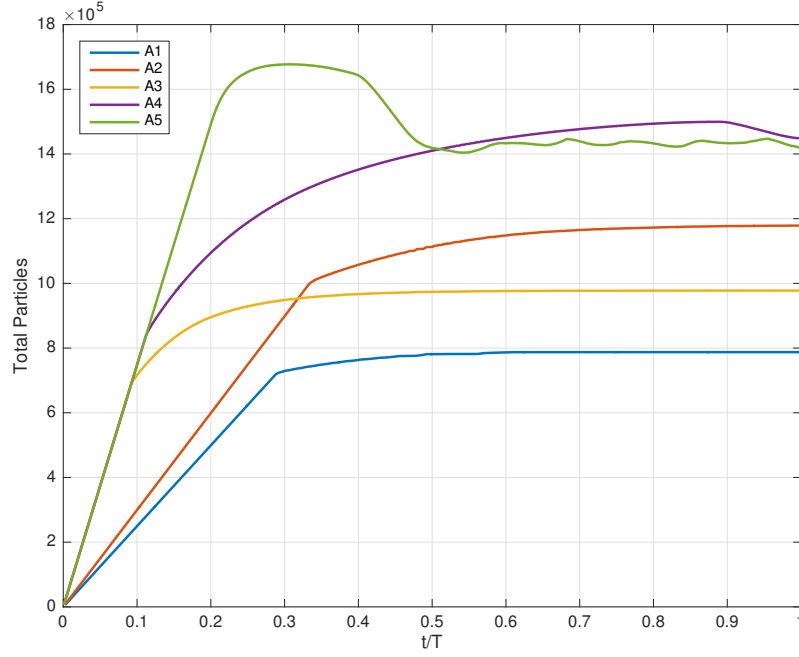


Figure 4.5: Total number of particles in the simulation domain at different time steps

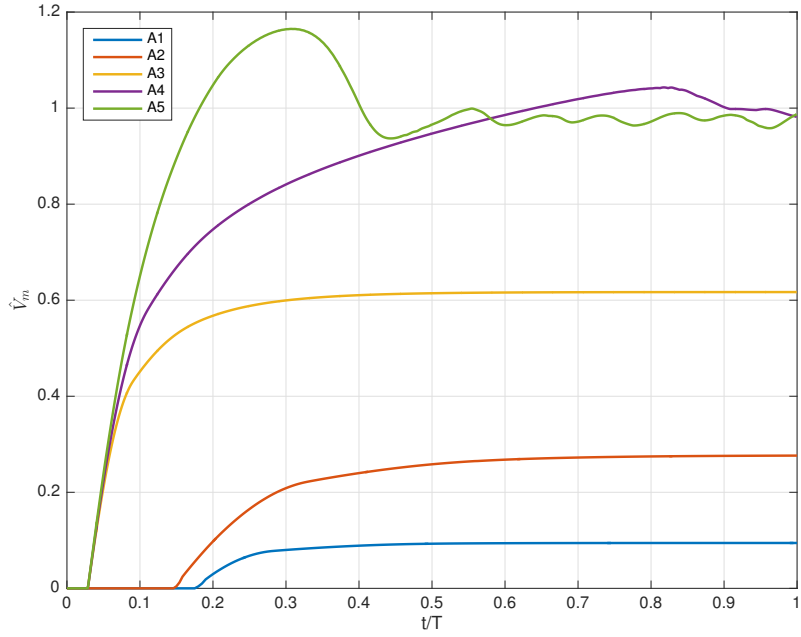


Figure 4.6: Maximum potential \hat{V} on the $x-y$ cutting plane at different time steps.

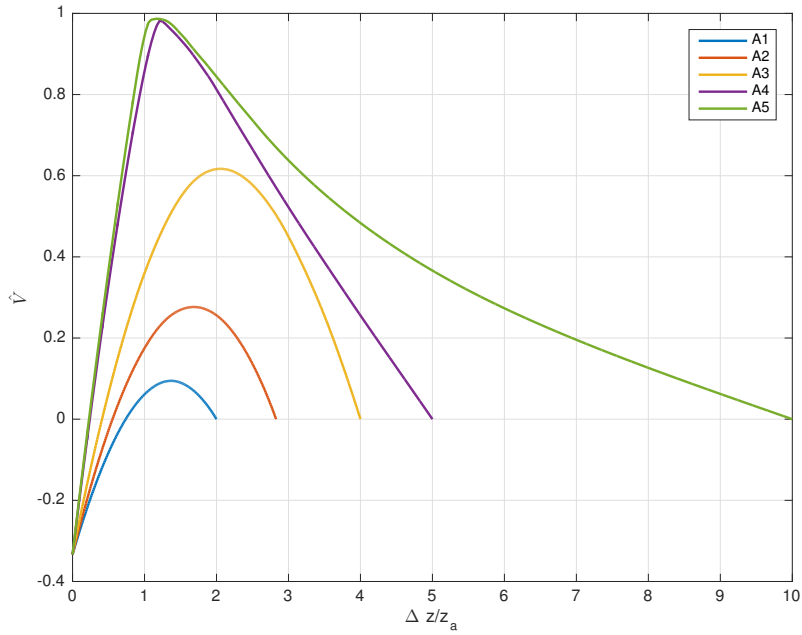


Figure 4.7: Potential profiles for ion beam neutralized at different distances $\Delta z/z_a$ from emission surface of radius $R_b = 10$ cm.

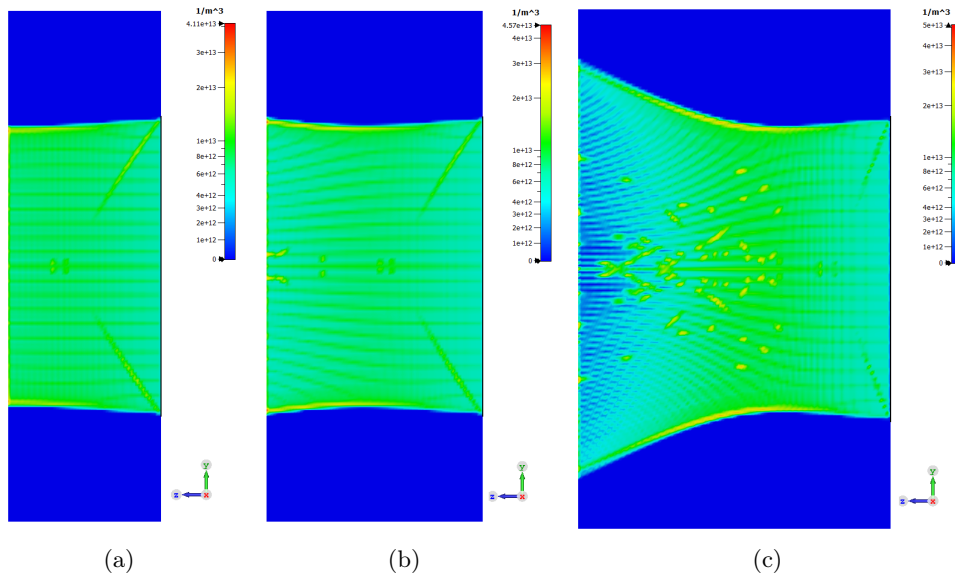


Figure 4.8: Ion density number for cases $A1$, $A2$ and $A3$ in (a), (b) and (c), respectively, at the simulation steady-state.

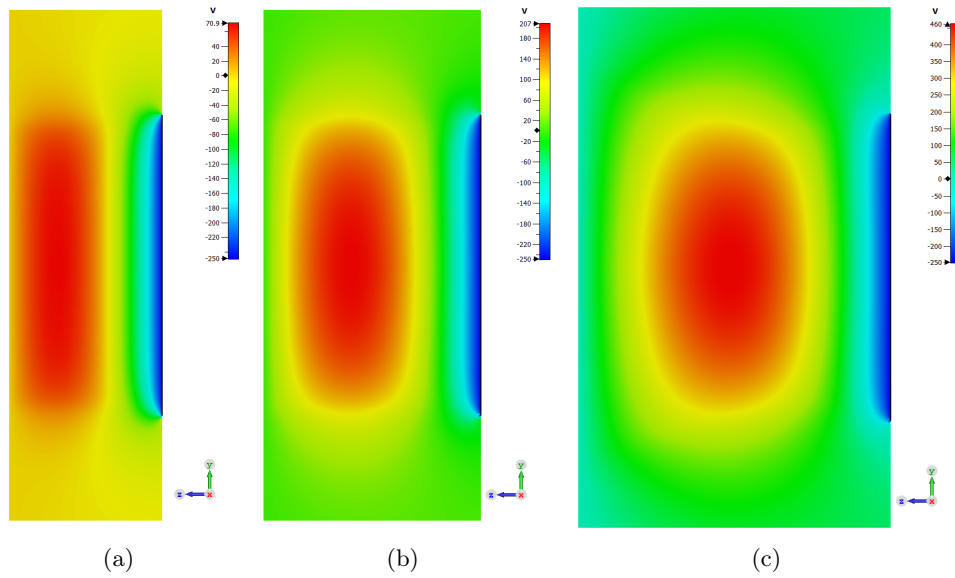


Figure 4.9: Potential map for cases $A1$, $A2$ and $A3$ in (a), (b) and (c), respectively, at the simulation steady-state.

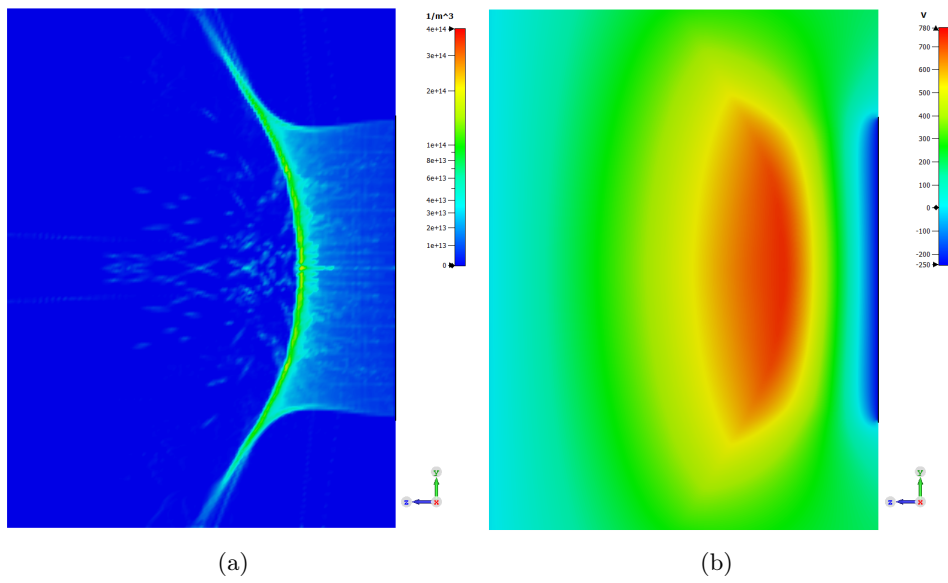
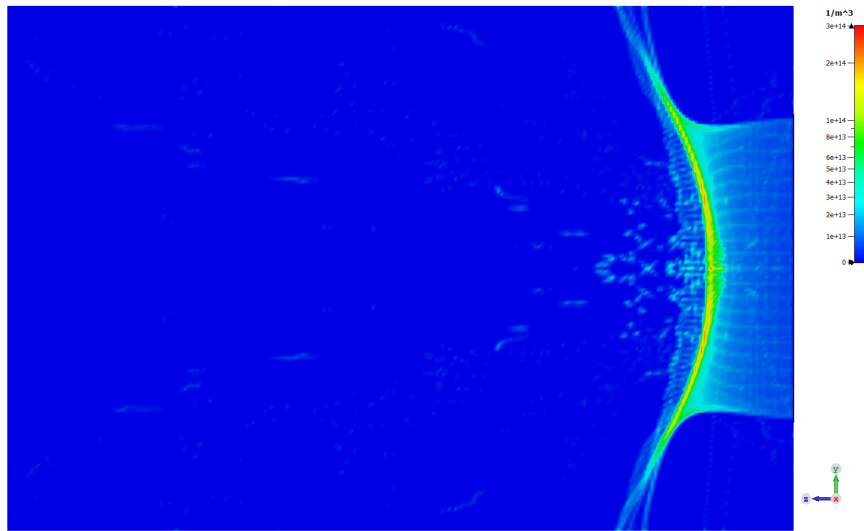
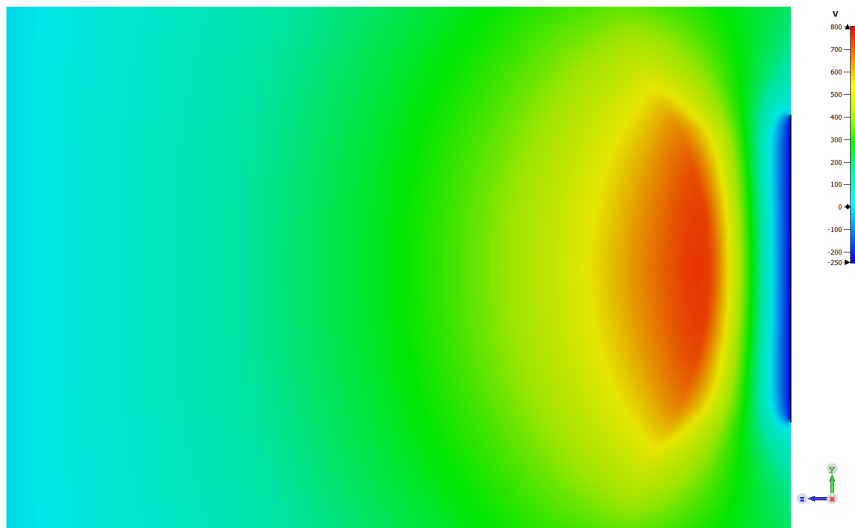


Figure 4.10: Ion density number and potential maps for case *A4* in (a) and (b), respectively, at the simulation steady-state.



(a)



(b)

Figure 4.11: Ion density number and potential maps for case A5 in (a) and (b), respectively, at the simulation steady-state.

Chapter 5

Particle-In-Cell Simulations

5.1 GOCE's T5 Ion Thruster Plume Modeling

5.1.1 GOCE ITA Plume Data

Firstly, the GOCE's Ion Thruster Assembly (ITA) plume model is validated with the experimental plume data obtained during the qualification testing [23]. The ion beam has been characterized by use of Faraday cup probes and Langmuir probes. The beam probe diagnostic consisted of a 2.4 m diameter semi-circular arm, on which 11 Faraday Cup probes were used for ion current density measurement, and 2 Langmuir probes were mounted to measure the plasma density and electron energy. The schematic of the probes position is showed in Figure (5.1): the Faraday cup probes were positioned equidistantly along the central region of the arm, and the Langmuir probes were mounted at the centre. The whole arm can be rotated about its axis, so that a 2D plot of ion current density and 1D plot of plasma properties can be produced.

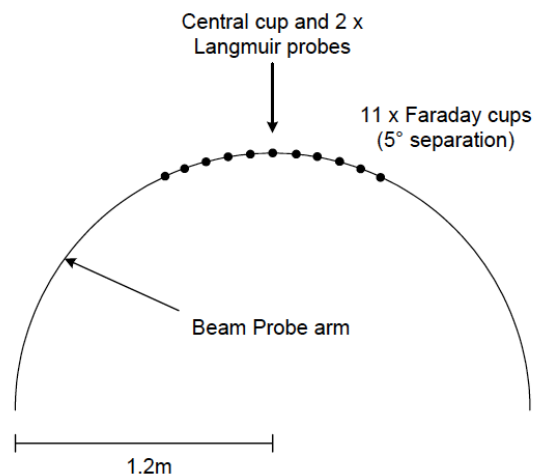


Figure 5.1: Schematics of the beam probe diagnostic used in [23].

The plume measurements was completed for beam divergence, ion current density distribution, electron density, effective electron energy and plasma potential over the required operational thrust range of 1 – 20mN. However, in this thesis only three thrust levels are considered and their corresponding performance parameters, and are reported in Table (5.1).

T (mN)	\dot{m} (mg/s)	I_{beam} (mA)	Power (W)	I_{sp} (s)
3	0.09	57.4	113	1268.2
8.3	0.240	155.8	258	2171.9
20	0.531	366.7	598	2980.2

Table 5.1: Steady state performance parameters.

5.1.2 Source Models

Let us consider the operation parameters corresponding to the thrust level of 8 mN and assuming that all the propellant is ionized, the exhaust velocity of Xenon ions is

$$v_i = I_{sp} g_0 = 21298.8m/s. \quad (5.1)$$

This velocity correspond to the injection velocity used in the simulations. Thus, the ions are emitted as a cold high velocity beam, assumed to follow the Maxwellian distribution at 0.1 eV of thermal energy.

$$v_{ti} = \sqrt{\frac{3k_b T_i}{m_i}} = 469.57 m/s \quad (5.2)$$

The ions Mach number based on its thermal velocity is

$$M_i = \frac{v_i}{v_{ti}} = 45.36 \quad (5.3)$$

To be noticed that the real Xe^+ to electron mass ratio was used.

$$\frac{m_i}{m_e} = 239313.24. \quad (5.4)$$

Some recent works, in order to speed up the simulation time, assumed protons as ions [68], [69], which are much lighter than the actual Xenon ions.

$$\frac{m_p}{m_e} = 1836. \quad (5.5)$$

The ion current density is

$$J_i = \frac{I_{beam}}{\pi R^2} = 19.84 A/m^2 \quad (5.6)$$

where $R = 5$ cm is the thruster radius. Using this values along with the velocity at the exit defines the average ion number density as

$$\bar{n}_i = \frac{J_i}{qv_i} = 5.813 \times 10^{15} \text{ m}^{-3}. \quad (5.7)$$

The initial beam divergence $\alpha_0 = 12^\circ$ and the Gaussian profile for ion density at the thrust exit are imposed, as suggested in [11]

$$n(r) = n_{scale} \exp\left(-\frac{r^2}{R_{th}^2}\right), \quad (5.8)$$

where n_{scale} is consequently calculated once \bar{n}_i is known.

The neutraliser current is calculated by assuming the quasi-neutrality of the beam in which ion and electron densities are equal

$$n_e \approx n_i, \quad (5.9)$$

and it is assumed that the electrons are injected with their thermal velocity corresponding to $T_e = 1$ eV

$$v_{te} = \sqrt{\frac{3k_bT_e}{m_e}} = 726407 \text{ m/s}. \quad (5.10)$$

According to this data, the expansion of the plasma is meso-thermal, since the following characteristics are verified:

$$v_{te} \gg v_i \gg v_{ti}. \quad (5.11)$$

In addition, in a well neutralized plasma beam the net current is balanced

$$I_{beam} + I_e = 0. \quad (5.12)$$

The electron current density is

$$J_e = n_i q v_{te} = 676.55 \text{ A/m}^2 \quad (5.13)$$

Hence, the neutralization emission radius surface is calculated

$$R_e = \sqrt{\frac{I_{beam}}{\pi J_e}} = 0.8562 \text{ cm} \quad (5.14)$$

All the simulations considered the emissions in vacuum with only ions and electrons species. The neutral particles are not included.

The Debye length at the thruster exit

$$\lambda_D = \sqrt{\frac{\varepsilon_0 k_b T_e}{n_i q^2}} = 9.75 \times 10^{-5} \text{ m} \quad (5.15)$$

and the number of particles sitting in a Debye cube

$$N_D = n \lambda_D^3 = 5.668 \times 10^{11} \quad (5.16)$$

show that the plasma close to the thruster exit is collisionless. The plasma frequency is

$$\omega_{pe} = \sqrt{\frac{n_e q^2}{\varepsilon_0 m_e}} = 4.3 \times 10^9 \text{ rad/s}. \quad (5.17)$$

5.1.3 Simulation Setup

The thruster is modeled as a cylinder having a diameter 10 cm and length 5 cm. The material property is set to a perfectly electric conducting (PEC) material with a fixed electric potential $V_{sc} = 0$ to the ambient. The neutraliser emission surface is placed 2 cm downstream and 6 cm upper from the thruster's exit center, inclined at 30° towards the beam. The ions and electrons sources are discretized in 20 emission points on their surfaces, showed in Figure (5.2), from which at every time step 1521 macro-particles per specie are injected. Thus, the resolution requirement is respected.



Figure 5.2: Ions and electrons emission surfaces.

The simulation domain size is $60 \times 60 \times 140$ cm, huge enough with respect to the thruster diameter. The thruster axis is aligned with the simulation z axis. In order to validate the model with GOCE's ITA data, a semicircular arm, on which Faraday Cup and Langmuir probes were mounted, is modeled with two circular curves perpendicular to each other, with radius 1.2 m from the thruster exit and length $\pi/3$. On this curve the beam characteristics, like ion beam current density J_i , electron density n_e and plasma potential V_p , are evaluated. The effective electron energy is calculated on the plane $x - y$ located at $z = 1.2$ m from the thruster exit. All the boundaries are set to be opened according to which the particles hitting them are removed from the simulation. The simulation setup is illustrated in Figure (5.3).

The domain was modeled using $120 \times 120 \times 140$ hexahedral uniform cells with constant size of $\Delta x = 1$ cm. The total number of cells is 2016000. However, in order to resolve the space charge density on the mesh and to simulate the neutralization process the mesh requires to resolve the Debye length ($\Delta x = \lambda_D$). Setting the mesh size to λ_D with the same simulation domain span leads to have 2×10^{12} cells; the mesh refinement by employing unstructured tetrahedral cells in the beam zone would not resolve the problem, since the total number cell would be still large (several thousands of millions). Moreover, the time step must be selected to respect the CFL condition and the Leapfrog time step limitation.

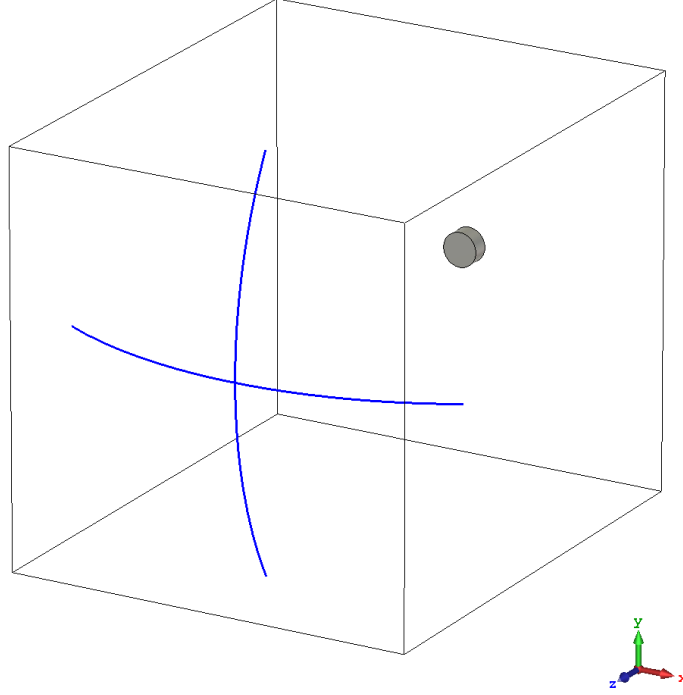


Figure 5.3: Simulation setup with curves representing the probes.

The maximum frequency of the system to be resolved is ω_{pe} and including at least 4 oscillations at the thruster exit and 10 at a few radii conduct to

$$\Delta t = 10^{-10} \text{ s}. \quad (5.18)$$

The simulation has to be run till the steady-state, in which the particles in the simulation domain does not vary in time: the injected number of macro-particles from the sources is equal to the number of macro-particles removed from the boundaries. Hence, reaching the steady-state solution requires that at least the ion beam reaches the boundary at z_{max} . If the ion beam velocity is assumed to be constant, the necessary time to cross the whole domain is

$$T_{sim} = \frac{z_{max}}{v_i} = 6.57 \times 10^{-5} \text{ s} \quad (5.19)$$

and the number of timesteps with $\Delta t = 10^{-10} \text{ s}$ are

$$N_{steps} = 657300. \quad (5.20)$$

Thus, the modeling of the ion thruster plume with full-PIC methods on full-scale is not computationally feasible, since the equations are evaluated on a grid and the Poisson's equation solver goes with $N_g \ln N_g$. The time for a simulation would grow to several years and it would be problematic to store such a massive mesh.

Therefore, it is still possible to compute the transient process of the plume on a mesh with $\Delta x = 1$ cm, and stop the simulation before the particles reach the border. In this way, the thruster, instead of forming a distinct beam with the electrons forming a neutralizing cloud surrounding the beam, will operate in a virtual anode mode [66]. The reason is attributed to the concept of the Debye length, which is the shortest distance at which quasi-neutrality of a plasma can be assumed. Indeed, with the mesh of $\Delta x = 1$ cm only 1% of λ_D is solved. Plasma modelling with full-PIC method requires that the local non neutrality of the plasma is solved, otherwise the electron motion will not be simulated correctly [70].

In fact, after 10000 time steps, the ions are confined near the thruster exit and do not propagate downstream, as they lack the kinetic energy to pass over the potential hill of the virtual anode, and are reflected back to the thruster. From the potential and the charge density maps, showed in Figure (5.4), it can be observed that the potential hump formation is associated to the high space charge.

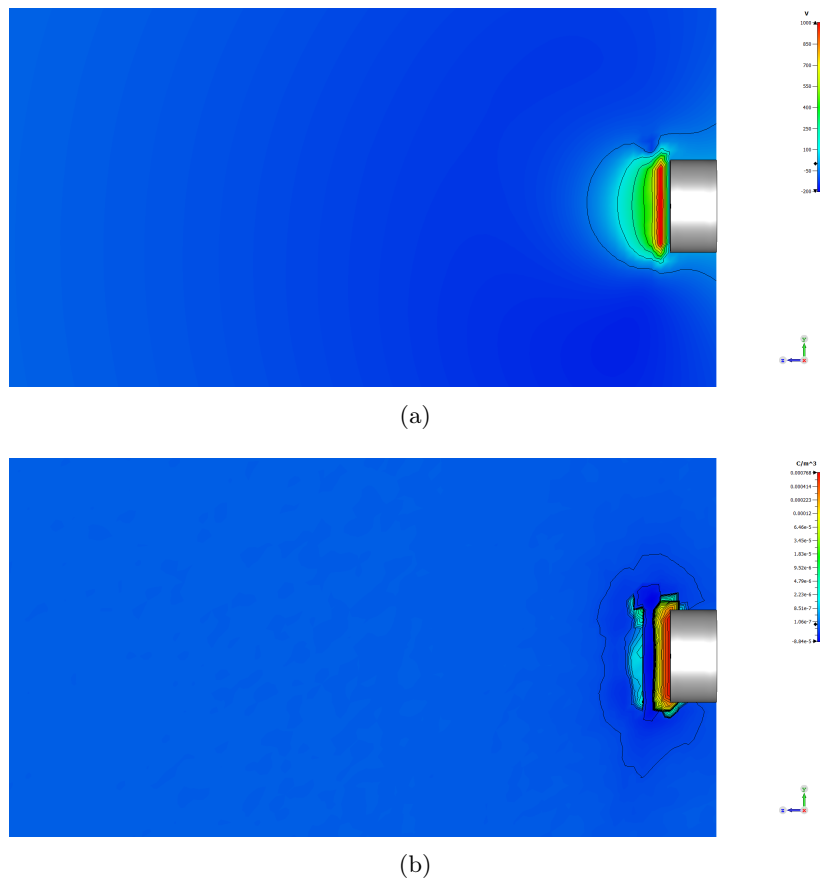


Figure 5.4: Potential (a) and charge density (b) after 10000 time steps on the center $z-y$ plane.

A similar simulation was performed in [71], in which the electrons were injected from

the same source as ions. However, in this case the thermal electrons are released from an upper position from the ion emitter for the charge neutralization. They are overall attracted to the potential hump formed by a virtual anode and propagate towards the ion emission surface. As soon as electrons are emitted from the neutraliser they are quickly attracted to the core of the ion concentration in front of the thruster exit and are initially accelerated to the negative z direction. Then most of them penetrate the core part of the ion beam. Figure (5.5) reports the ions and electrons densities. These, results show that the electrons react correctly to the ion beam concentration, but the space charge neutralization is still to be resolved.

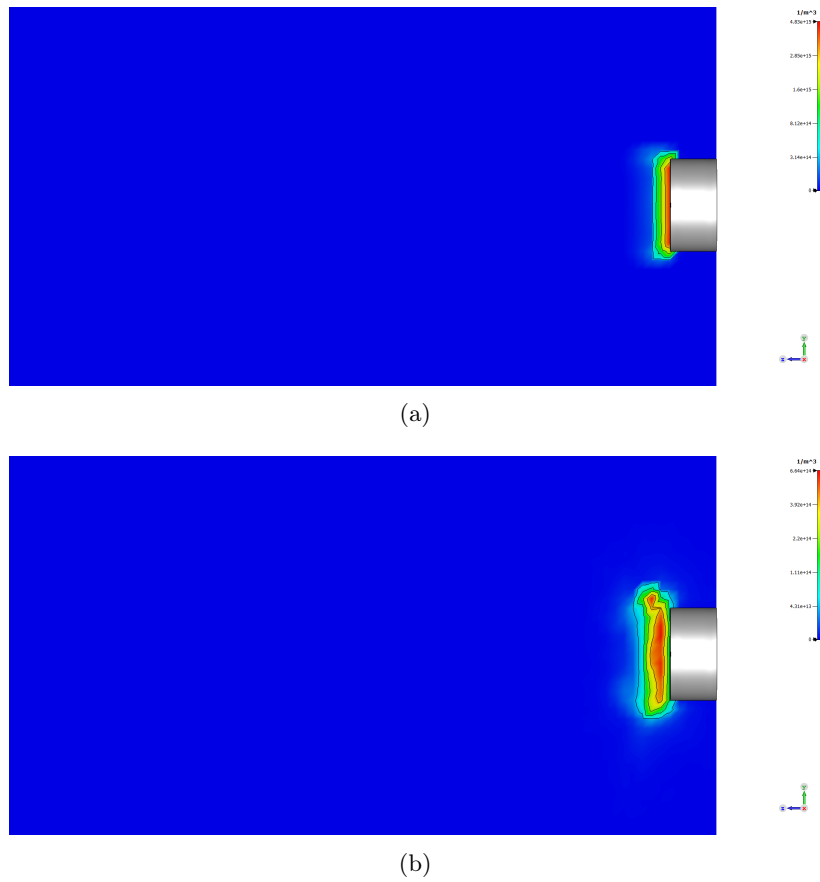


Figure 5.5: Ions (a) and electrons density (b) after 10000 time steps on the center $z - y$ plane..

5.1.4 Dimensional Scaling

The plasma plume of an ion thruster is not computationally feasible to study with full-PIC model on a full-scale geometry. For this reason a scaling-down procedure was proposed in [71]. In this thesis the same methodology is applied. The thruster dimensions and the domain span are scaled by a factor $f = 100$. However, the scaling-down procedure is possible on a condition of not altering the plasma plume dynamics. It means that a scaled-down model has to reproduce the same plasma environment of that produced by the full-sized model. Two requirements are to be verified:

- The scaled-down thruster dimensions and the span of simulation domain should be larger enough compared to the Debye length. This simplification has already been introduced in [26]:

$$L \gg \lambda_D. \quad (5.21)$$

- The plasma environment must be identical to the full-scale thruster.

A more detailed scaling treatment from mathematical point of view is available in [71]. The scaling factor adopted in this thesis is 1:100, which reduced the diameter of the thruster from 10 cm to 1 mm, while the cell size Δx is reduced from 1 cm to 0.01 cm. Hence, the mesh solves the Debye length in all the simulation domain. It should be noted that the emission surface diameter is still larger than the Debye length

$$D \approx 10\lambda_D \quad (5.22)$$

and is comparable to some recent studies of ion thruster neutralization and plasma plumes emissions by means of full-PIC methodology. The values range from $10\lambda_D$ [28], [69] to $40\lambda_D$ [72], [73], [74], [75]. Accordingly, the first requirement of the scaling-down method is satisfied.

In order to preserve the plasma environment through scaling the thruster operating conditions are to be adjusted. The ion beam and electrons currents are to correct by a factor f^2 and the external fields, if present, by a factor f . In this way, particle density, beam velocity, particle temperatures are not to rectify.

5.1.5 Plume Model Validation

To validate the plasma plume model emission it has been considered the operation parameters corresponding to the thrust level of 8 mN. The simulation domain span of the scaled-down model is $12R \times 12R \times 28R$, discretized with $120 \times 120 \times 140$ hexahedral uniform cells having $\Delta x = 10^{-4}$ m. In this was the Debye length is solved in all the simulation domain and the total cells number is not altered, $N = 201600$. To be observed that the simulation domain span is still much larger than λ_D , since $R = 5\lambda_D$.

The simulation ran for 20000 time steps with uniform $\Delta t = 10^{-10}$ s to simulate

$$T_{sim} = 2 \times 10^{-6} \text{ s}. \quad (5.23)$$

This time is found to be sufficiently long to make the ion beam reach the boundary at z_{max} and achieve the steady-state. In Figure (5.6) is illustrated the number of simulation macro-particles as a function of simulation time. The electrons reached the steady-state at the time step when the ions beam reached the boundary at z_{max} . The Xe^+ number of macro-particles grow due to the expansion in radial direction. Negligible variations in ion density are observed in the zone of beam core, after 8000 time steps. It can be observed that after 1000 steps ($\Delta t = 0.1$ ns) the electrons macro-particle number follow different path, since at the simulation beginning the electrons are emitted with their thermal velocity and some have escaped through the boundary, before the ion beam has formed. When ions form a positive space charge, the electrons are immediately accelerated to the potential formed by ions, and thus, they are trapped. Indeed, after 25 ns, as showed in Figure (5.7), the number of negative particles start to grow till the steady-state.

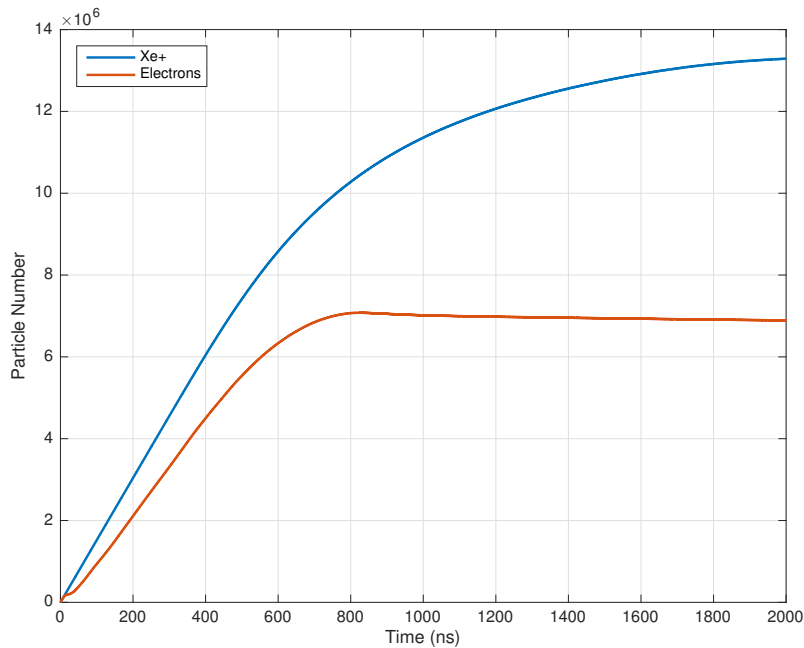


Figure 5.6: Macro-particles count in the simulation domain.

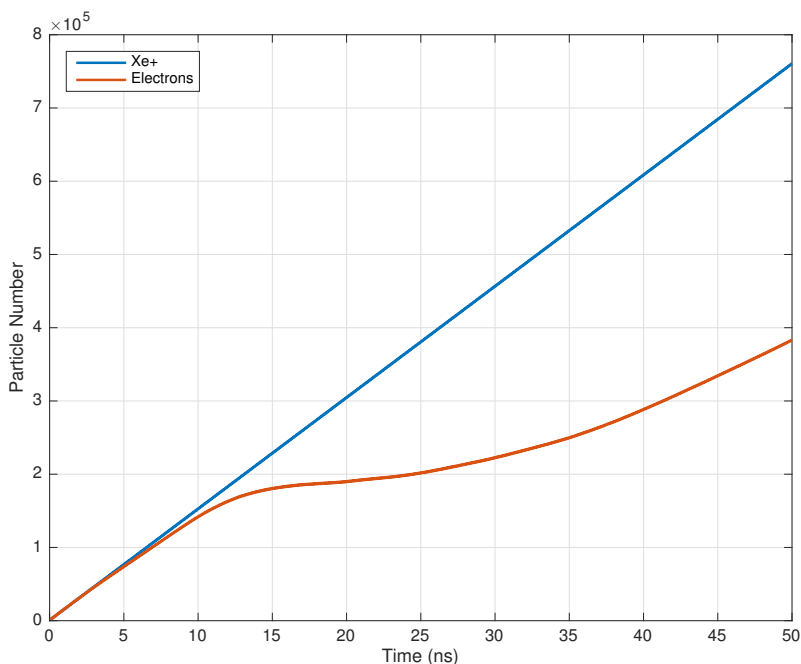


Figure 5.7: Macro-particles count after 500 time steps in the simulation domain.

It is interesting to compare simulation results with experimental GOCE ITA measurements. The comparison of ion beam current density between experimental measurements and PIC simulation results are reported in Figure (5.8). Due to the simulation domain restriction these results are shown over the beam angle range of -30° to 30° at distance $12R$ from the thruster exit. To the measurements first order interpolation is applied. Good agreement is found between simulated ion current and the measure. However, the simulated solutions present a stochastic noise, since the simulation will never contain enough particles to represent what actually the nature does. For this reason a zero-phase digital filtering is performed and compared to experimental data, as showed in Figure (5.9). From results presented the plume model fits very well measured current density data in the main beam region. Ion density beam after 20000 time steps is illustrated in Figure (5.12).

Figure (5.10) shows plasma potential as a function of beam angle at distance $12R$ from the thruster exit on the $x = 0$ cutting plane. A little disagreement within 1 V is found and attributed to the high electrons mobility, since not all the electrons are captured by the ion beam, a little high energy swirl is formed, as it can be observed in Figure (5.13). Whatever, the potential map on $y - z$ cutting plane through the thruster center $x = 0$, in Figure (5.14), demonstrate that the plume is well neutralized.

Nevertheless, electron density plot in Figure (5.11) provides a disagreement between the results of the two assessments. The measured electron density is almost 35 times higher than the numerical solution. It might be also observed that a such high n_e would lead to have negative space charge density, and thus, negative plasma potential of the plume. Instead, from the measurement V_p is positive. This discrepancy is attributed to the exper-

imental error, since the measure was performed with a positively polized Langmuir probe [23], which attracts negative charges. Moreover, the analysis method of Langmuir probe data assumes a quasi-neutrality. Thus, this measure can not be considered as accurate. However, an expected concordance between two data may be observed: the electron density peaks at the centre of the ion beam.

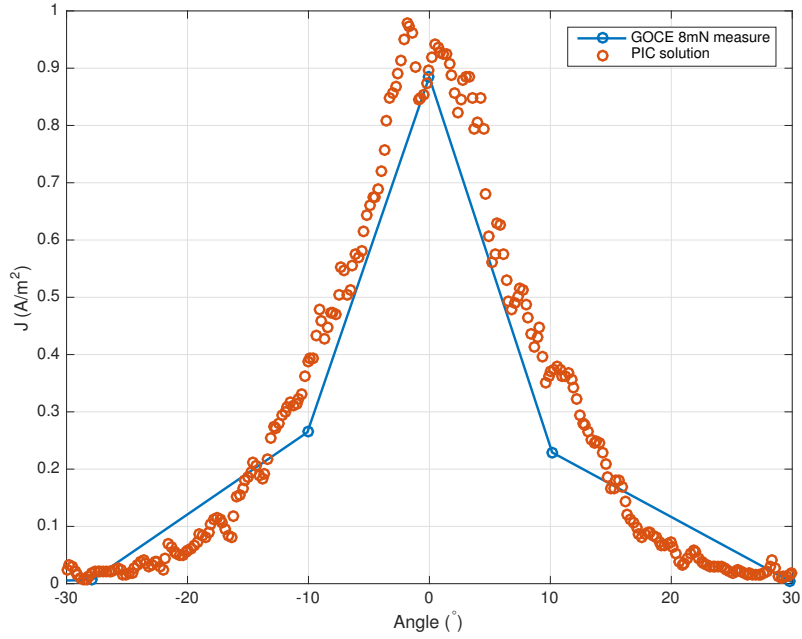


Figure 5.8: Ion current density validation at distance $12R$ from thruster exit.

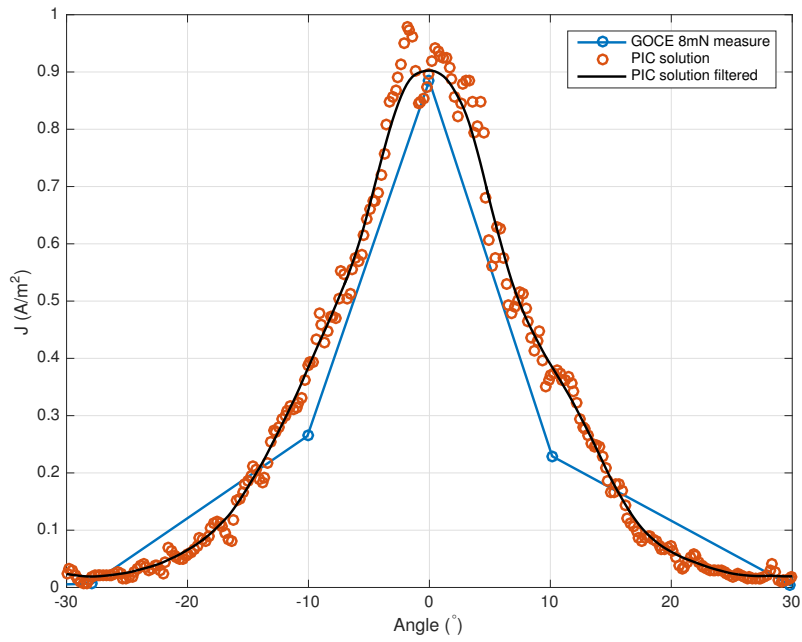


Figure 5.9: Ion current density validation and filtered simulation solution at distance $12R$ from thruster exit.

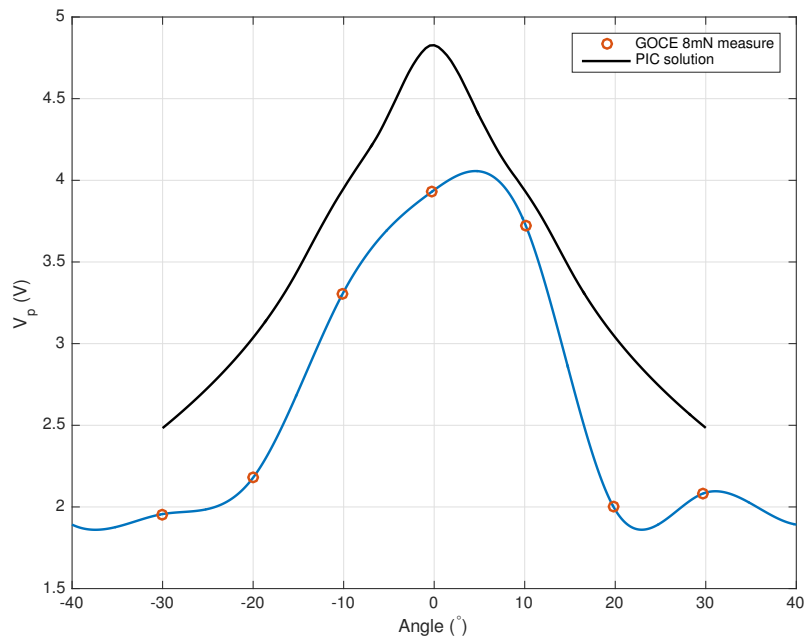


Figure 5.10: Plasma potential validation at distance $12R$ from thruster exit.

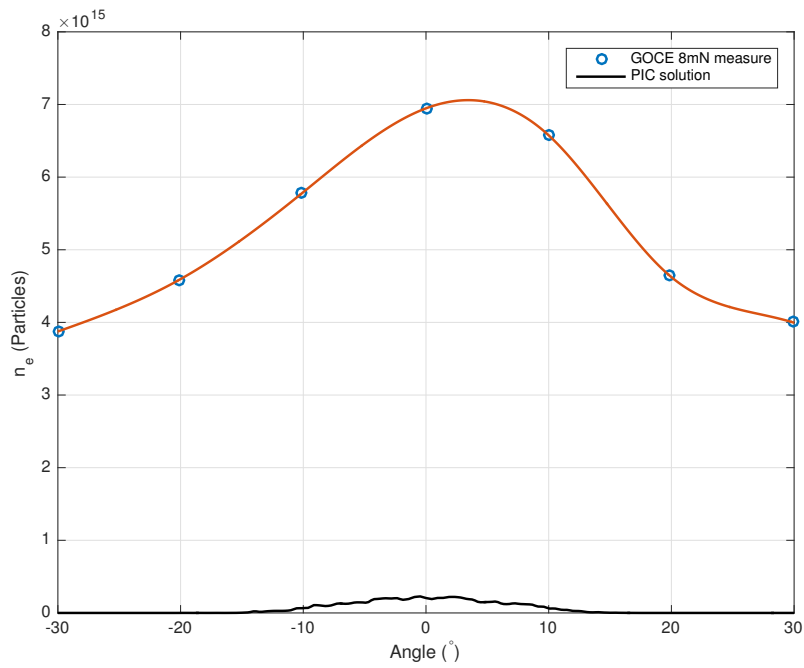


Figure 5.11: Electron density at distance $12R$ from thruster exit.

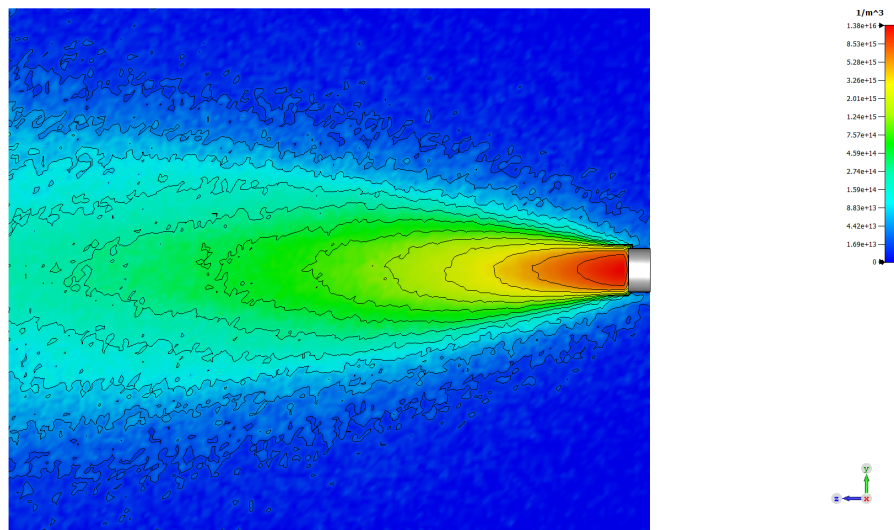


Figure 5.12: Ion density map at the simulation steady-state on the center $z - y$ plane.

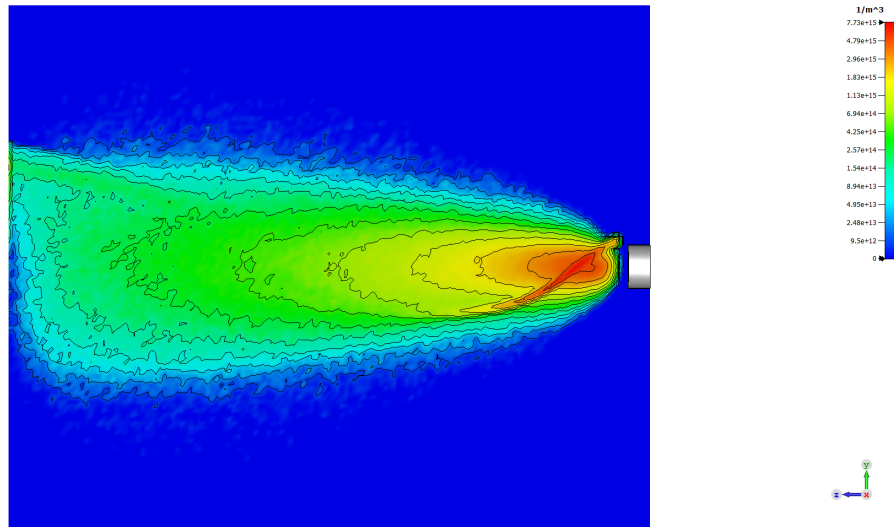


Figure 5.13: Electron density map at the simulation steady-state on the center $z - y$ plane.

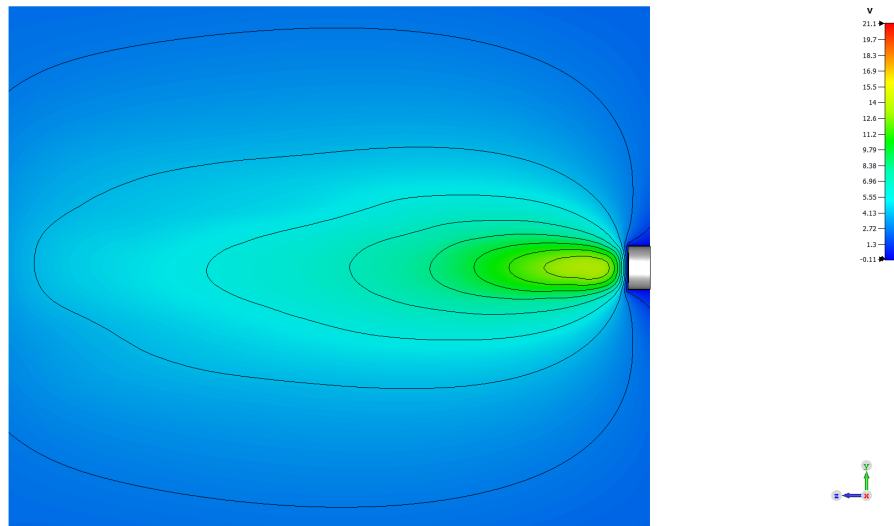


Figure 5.14: Potential map at the simulation steady-state on the center $z - y$ plane.

5.2 Magnetic Thrust Vectoring Concept

5.2.1 Magnetic Steering Analysis

A gridded ion thruster can achieve thrust vectoring by simply applying a transversal magnetic field to the ion beam ejected from the engine. From analytical model the steering angle is

$$\alpha_x = \arcsin\left(\frac{qB_y L}{m_i v_{beam}}\right) \quad (5.24)$$

Assuming to fix the distance $L = 10$ cm, where the field is applied, the plume deflection angle α in direction x as a function of applied magnetic B_y is reported in Figure (5.15) for a generic ion thruster with 10 cm of diameter operating at three thrust levels. Thus,

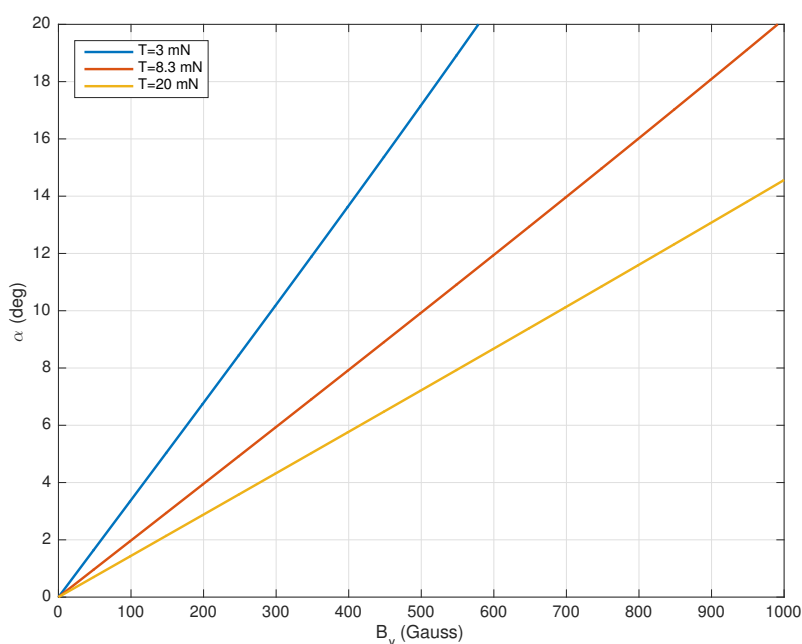


Figure 5.15: Plume deflection angle as a function of applied magnetic field to the ion beam for a fixed application distance $L = 10$ cm.

from analytical model in Equation (5.24), the displacement of thrust vector of about 8° can be obtained with relatively low magnetic fields. The Table (5.2) shows the operating conditions of a 10 cm diameter gridded ion thruster and the corresponding magnetic field B_y needed to achieve $\alpha = 8^\circ$. These values seem to be very promising, as such low magnetic fields may be obtained with device employing neodymium magnets, which have remanence field $B_r = 14000$ Gauss [76], or electromagnetic coils. However, some interesting questions about the application on the ion thruster plume may arise:

- The positively charged particles are not accelerated with the same velocity, therefore instead, they follow a Maxwellian distribution function. Hence, each particle moves

T (mN)	\dot{m} (mg/s)	I_{beam} (mA)	Power (W)	I_{sp} (s)	B (Gauss)
3	0.09	57.4	113	1268.2	236
8.3	0.240	155.8	258	2171.9	403
20	0.531	366.7	598	2980.2	553

Table 5.2: Performance parameters of a gridded ion thruster having 10 cm of diameter and the magnetic field needed to carry out a thruster vector angle of 8° .

with a different velocity and the deflection plume angle depends on its velocity. The analytical calculations does not provide this kind of information. Additionally, one may ask if the magnetic field influences a plume divergence?

- The relative position of the neutraliser with respect to the applied magnetic field should be studied too, since the electrons are much lighter than ions, and thus, they are easy magnetizable and follow the magnetic lines in transversal direction, instead of being trapped by the ion beam.

The two topics cannot be discussed by means of a solution from analytical model. More details can be obtained with a full-Particle-In-Cell simulation, which considers particles self-induced field in the region of deflection. In these simulations the CST Particle-In-Cell solver is coupled with CST Magneto-Static (MS) solver.

5.2.2 Simulation Setup

The magnetic thrust vectoring (MTV) concept is modeled as an uniform applied magnetic field in direction y and is applied to the plume model of GOCE's ITA. According to the Lorentz force the ion beam will be deflected in direction $-x$. The thruster is simulated at three different operating conditions and the magnetic field is created such to reach a deflection of 8° (see Table (5.2)). It is necessary to move the neutraliser downstream the MTV field in order to avoid the fully magnetization of electrons. According to the Kaufman's experiments [3], the electrons emitter may be placed downstream the thruster exit, as some electrons tend to migrate upstream, and thus, the neutralization is achieved somewhere ahead of the actual electron source. In addition, in-flight experience on Artemis [36] demonstrated that the remote neutralization is possible.

Case	T (mN)	I_{beam} (mA)	I_{sp} (s)	B (Gauss)
1	3	57.4	1268.2	236
2	8.3	155.8	2171.9	403
3	20	366.7	2980.2	553

Table 5.3: Simulation cases to carry out a thruster vector angle of 8° .

The simulation setup is illustrated in Figure (5.16). The ion and electron source models have not been modified. The uniformly applied magnetic field is represented by red arrows

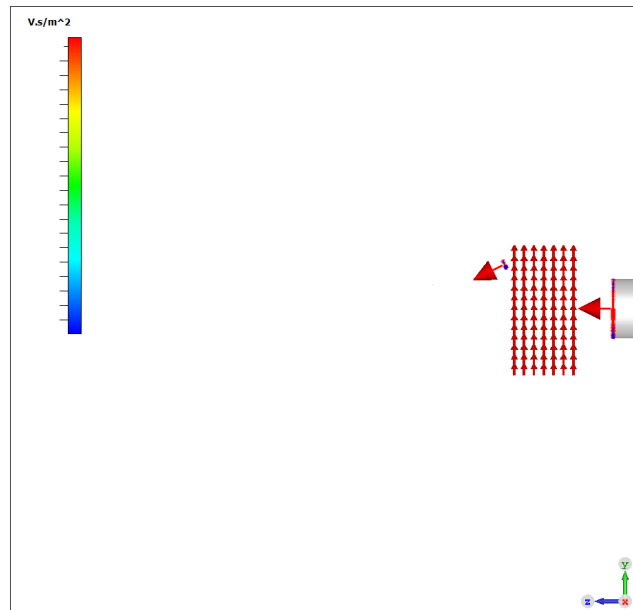


Figure 5.16: Simulation setup and MTV concept applied at the distance R from thruster exit.

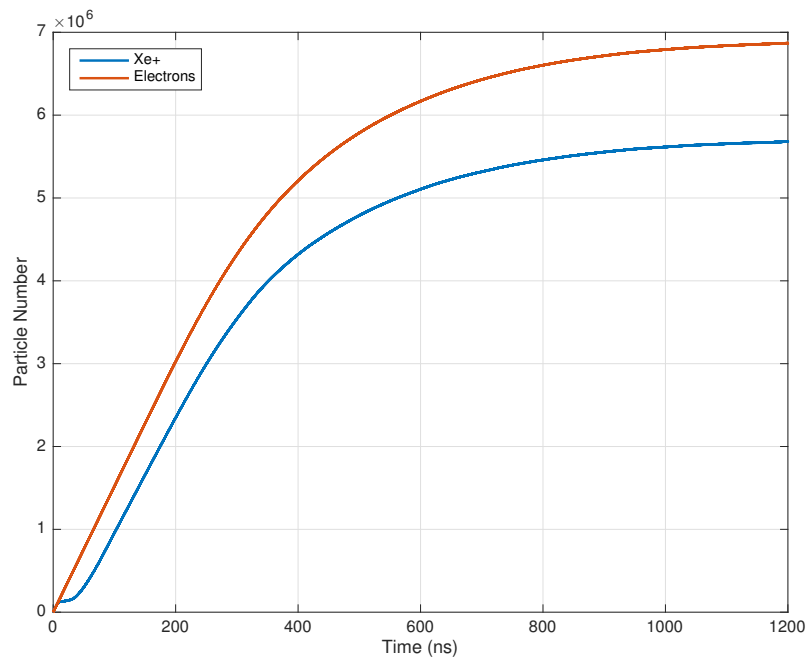


Figure 5.17: Macro-particles count in the simulation domain for thrust level 20 mN.

pointing in y and is applied in the sub-volume corresponding to $2D \times 2D \times D$ placed at

the distance R from the exit. The center of the sub-volume is aligned with the thruster's axis z . Moreover, the computational domain is decreased to $10R \times 10R \times 20R$ to speed up the calculation time. The scaling-down requirements are still satisfied. The domain is discretized with uniform hexagonal mesh cells having $\Delta x = 0.01$ cm. The total mesh cells are $N = 10^6$. The time step is $\Delta t = 10^{-10}$ s and the needed times to reach steady-state are simulated. Figure (5.17) shows that the simulation is at steady-state after 1200 ns. Small negligible variations of Xe^+ particles are observed due the radial expansion of the beam outside of the beam core.

5.2.3 Beam Diagnostics

In Figures from (5.24) to (5.27) are showed simulation results for three thrust levels with an applied magnetic field on an $z - x$ cutting plane through the emitter center at $y = 0$. The simulation cases are reported in Table (5.3). The results displayed include ion and electron densities, potential and charge density maps. Since the magnetic field B_y is applied along y axis, it is clearly seen from ion densities map that the plume is deviated along axis $-x$. Moreover, it can be seen that the beam ion density increases with higher thrust demands. It is interesting to note that even if the electron emitter is placed downstream the magnetic field, in all simulation cases, the neutralization of the beam is achieved, as the electrons migrate upstream the thrust vectoring applied magnetic field to neutralize high space charge. From the plasma potential map it can be observed that downstream values are comparable to that from T5 experimental test [23] [13]. A small potential hump is observed close to the thruster but this value is in agree with experiments data. Space charge density maps confirm that the neutralization is achieved and a meso-thermal plasma is formed, since inside the beam core electrons are attracted and trapped by ions.

For completeness, thrust vectoring performance is evaluated using the beam plasma diagnostics by means of ion density distribution at different distance from the thruster exit, showed in Figures from (5.18) to (5.23). Three different thrust levels are simulated. All figures report also a dashed lined corresponding to 8° of steering. The simulated solution is represented with $*$ and is filtered with digital zero-phase using Matlab.

In Figure (5.18) is illustrated the ion density distribution as a function of beam divergence at the distance $z = R$ on $y - z$ cutting plane with $x = 0$. For this distance the beam has not reached the magnetic steering field. In fact, the ion density distribution is found to be symmetrical with respect to zero angle, and thus, zero angle plume deviation is observed. With decreasing the thrust level the ion density distribution function decreases too, as the thruster operates at lower current.

Figure (5.19) shows the ion density distribution calculated at $z = 6R$ from the thruster exit. The profiles are not symmetrical with respect to the 0° plume angle, but instead the maximum points of three thrust levels are moved on the left side close to the 8° vertical line. Indeed, these results suggest that the plume is steered in $-x$ direction and the deviation of the thrust vector of around 8° is obtained.

At larger distances from the thruster exit the plume maintains its steering of about 8° . However, it can be observed once the beam has been steered, the distribution of ion density distribution is not symmetrical with respect to its maximum, but is skewed positive,

instead. From physical point of view, it means that higher ion density is observed on the side, where the deflection is required ($-x$). Hence, the plume divergence is increased on one side. The reason is attributed to the non uniform velocity distribution: ions on the right and left sides of distribution have lower velocity and those on the left side follow smaller Larmor radius, and thus, the deviation angle is higher than at the plume center. Whereas, particles on the right side are slower than at the particles at the center, and hence, are subjected to higher deflections too. In fact from ion density map, showed in Figure (5.24), higher beam divergence are noted in direction of the thrust vector.

As expected, from Figure (5.24) it can be seen that the plume, once crossed the zone with transversal magnetic field, it follows the direction of 8° from the thruster exit. Higher deflection angles are possible at cost of stronger magnetic fields or by applying it for longer distances, fixed the operating condition; while, higher thrust demands require higher strength of applied magnetic field. The direction of the thrust vector deflection depends on the direction of the magnetic field. Thus, in order to achieve the thrust vector in any azimuthal direction at different operating conditions, a device capable to rotate the field direction and change its magnitude is suggested.

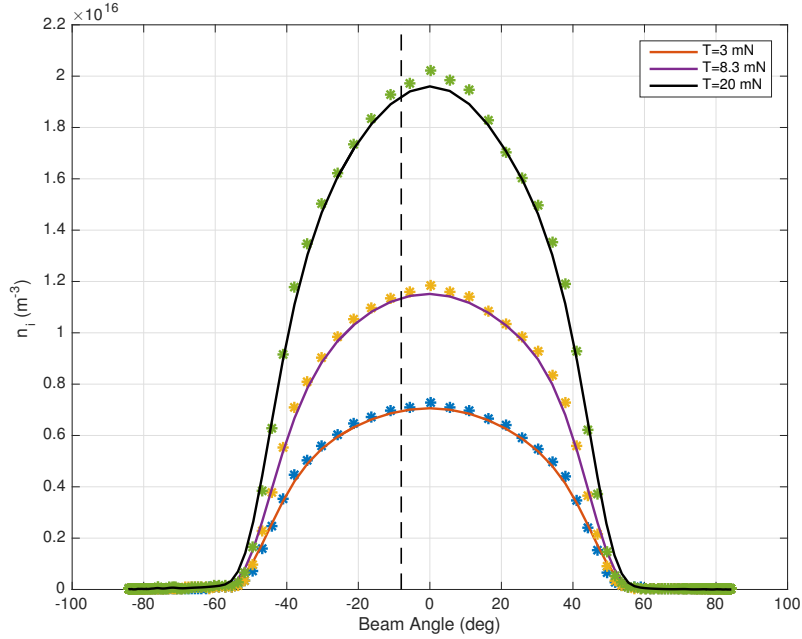


Figure 5.18: Ion density distribution at distance $z = R$ from thruster exit.

In this zone the ion beam has not crossed through the magnetic field zone yet, and indeed, the profiles is symmetrical with respect to 0° plume angle. The dashed vertical line indicates the divergence of 8° .

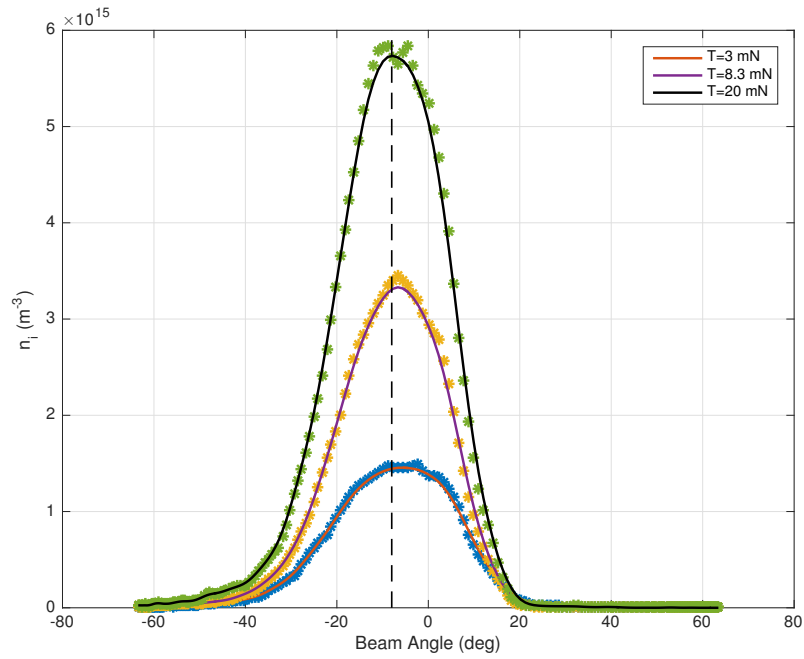


Figure 5.19: Ion density distribution at distance $z = 6R$ from thruster exit. The plume has crossed the magnetic field and deflection angle of around 8° is seen. The dashed vertical line indicates the divergence of 8° .

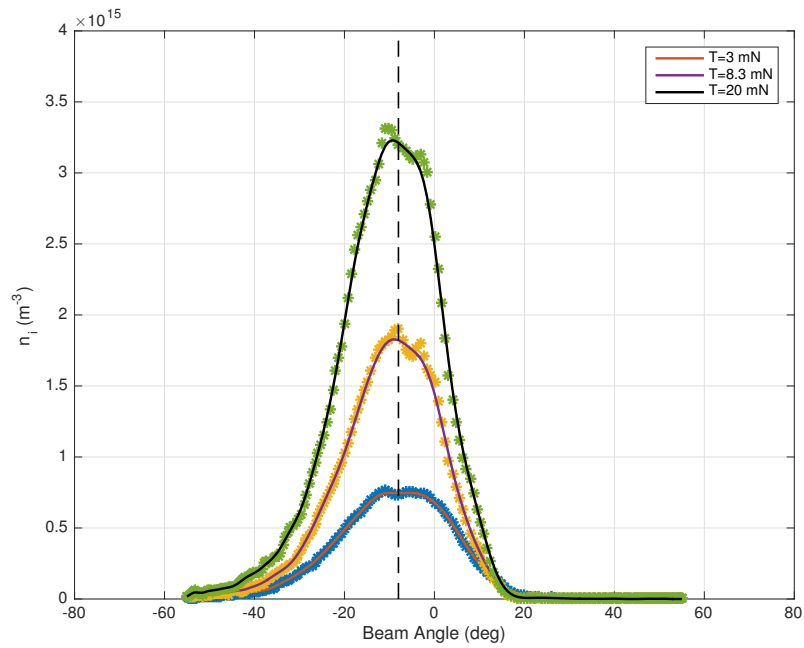


Figure 5.20: Ion density distribution at distance $z = 9R$ from thruster exit. The plume has crossed the magnetic field and deflection angle of around 8° is seen. The dashed vertical line indicates the divergence of 8° .

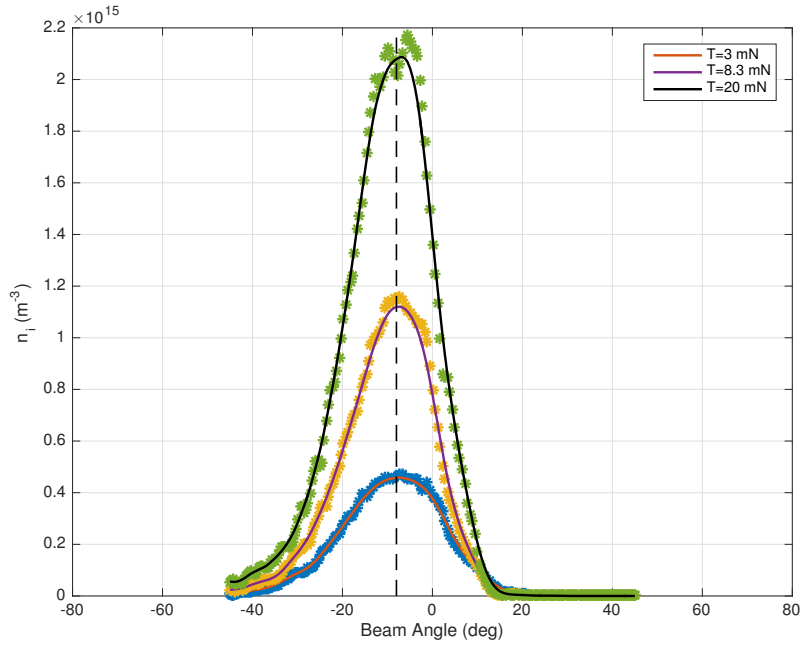


Figure 5.21: Ion density distribution at distance $z = 12R$ from thruster exit. The plume has crossed the magnetic field and deflection angle of around 8° is seen. The dashed vertical line indicates the divergence of 8° .

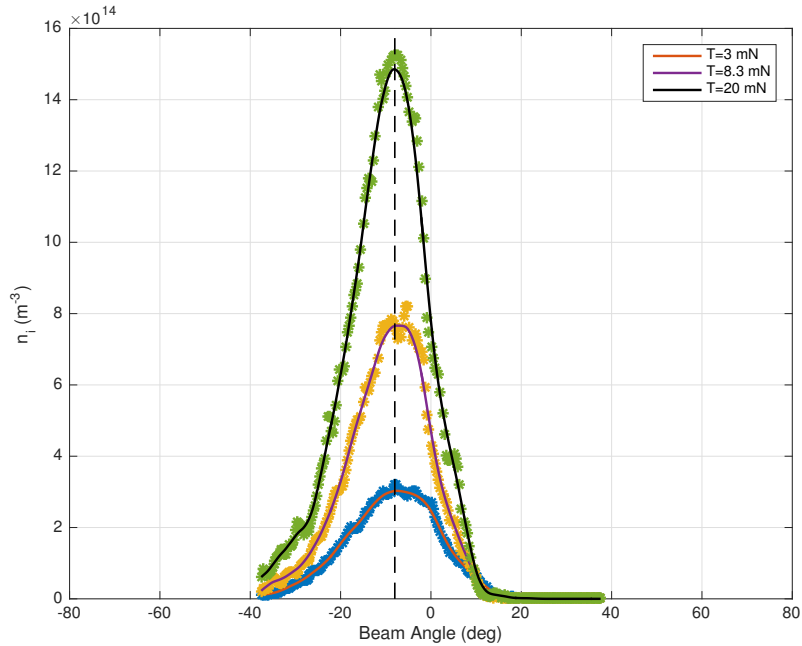


Figure 5.22: Ion density distribution at distance $z = 15R$ from thruster exit. The plume has crossed the magnetic field and deflection angle of around 8° is seen. The dashed vertical line indicates the divergence of 8° .

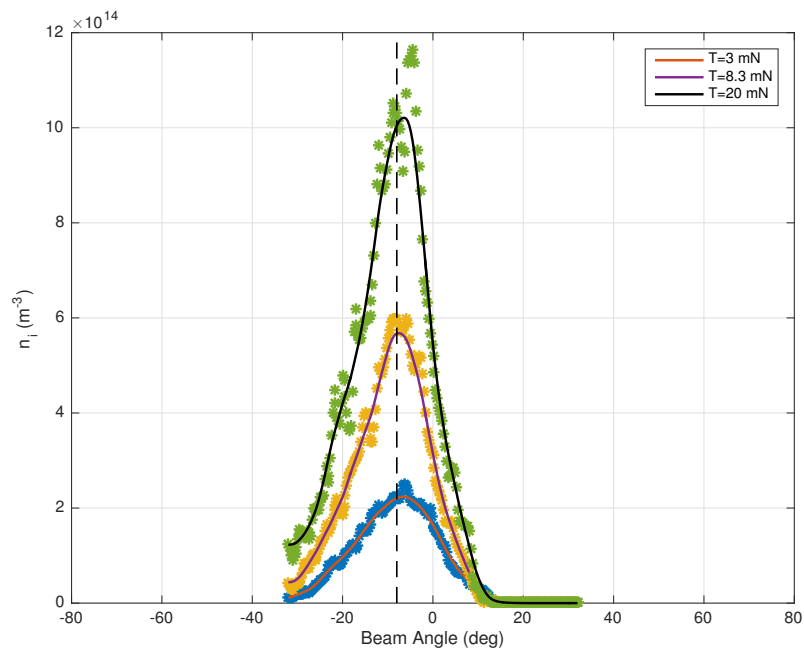
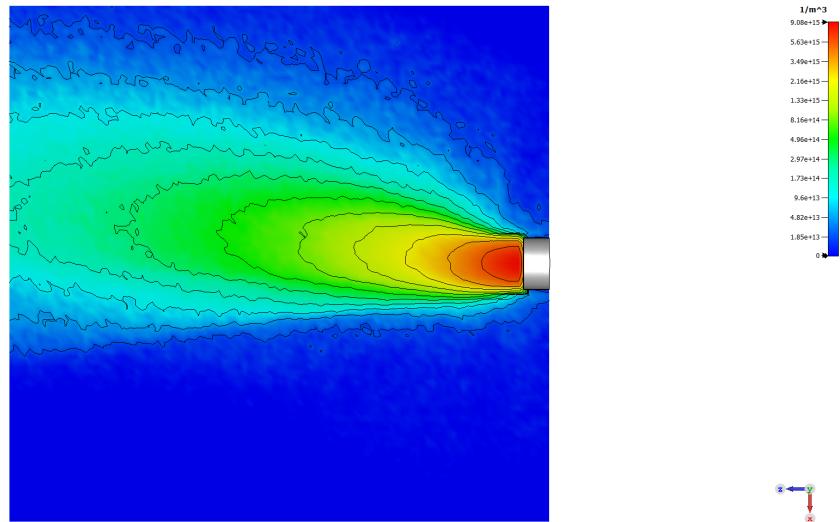
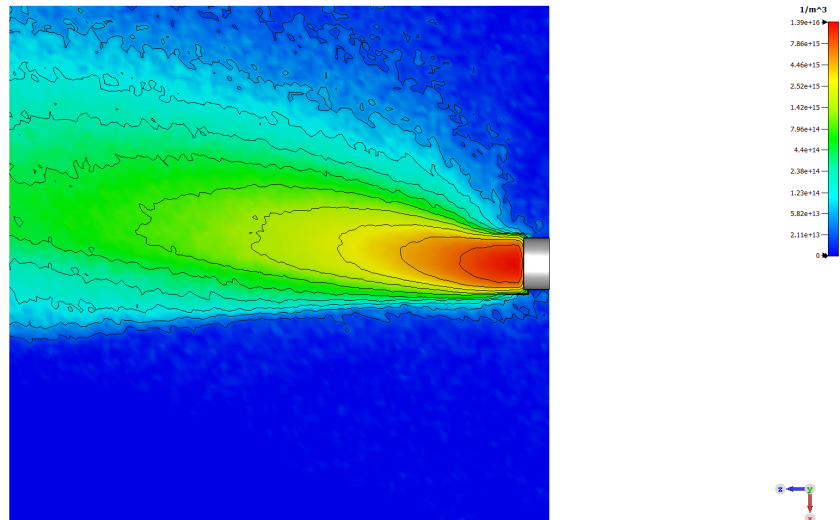


Figure 5.23: Ion density distribution at distance $z = 18R$ from thruster exit. The plume has crossed the magnetic field and deflection angle of around 8° is seen. The dashed vertical line indicates the divergence of 8° .

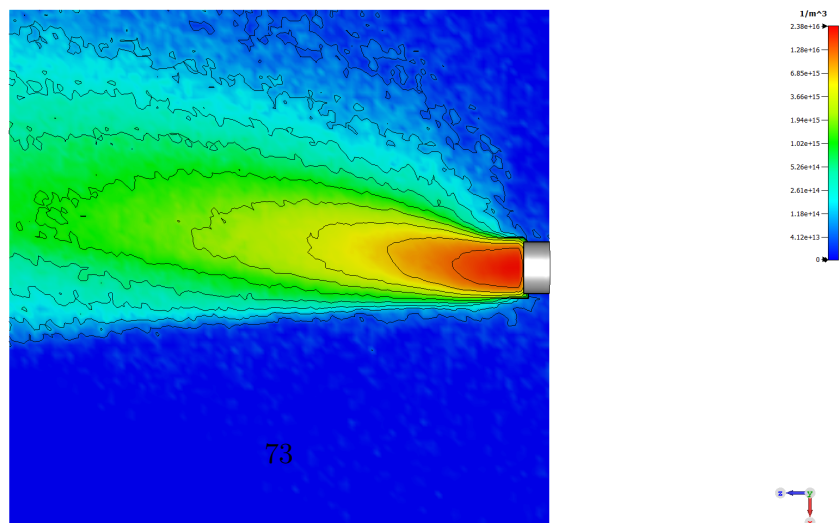
5.2. MAGNETIC THRUST VECTORING CONCEPT



(a)

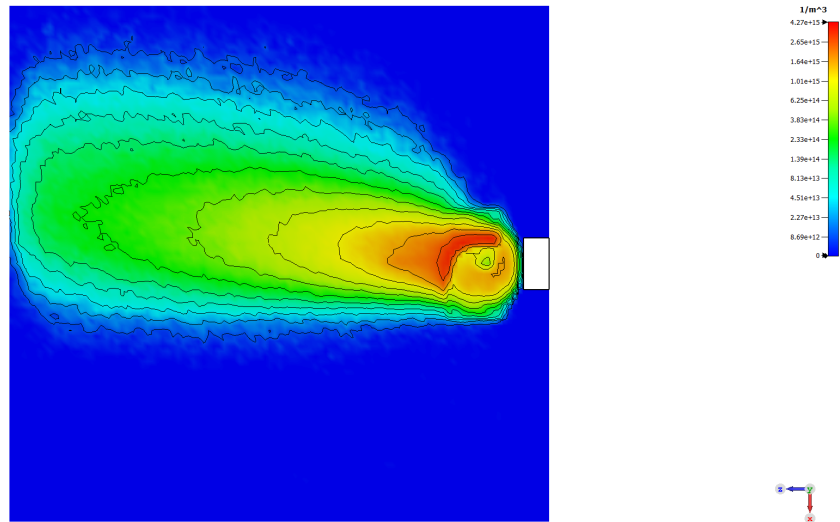


(b)

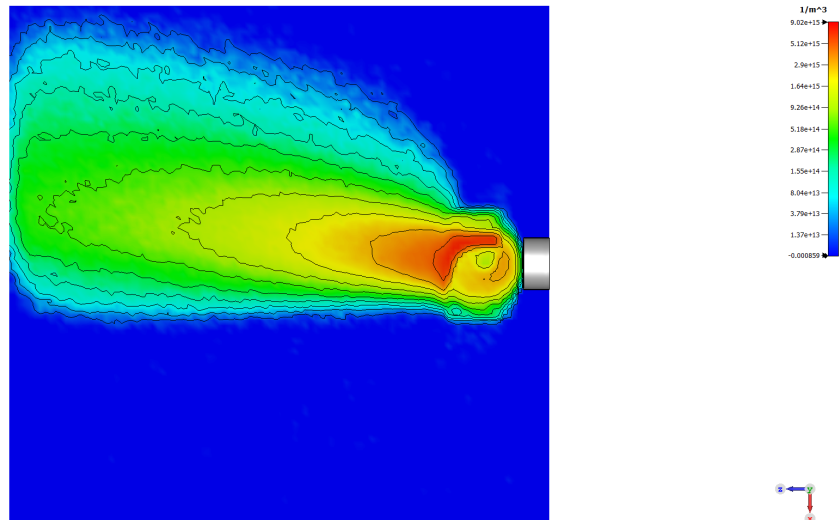


(c)

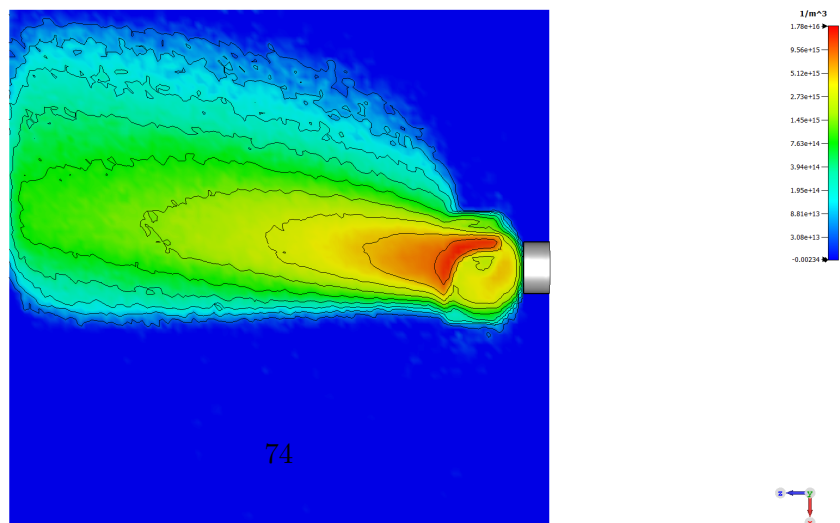
Figure 5.24: Ion density for thrust demands 3 mN (a), 8.3 mN (b) and 20 mN (c).



(a)

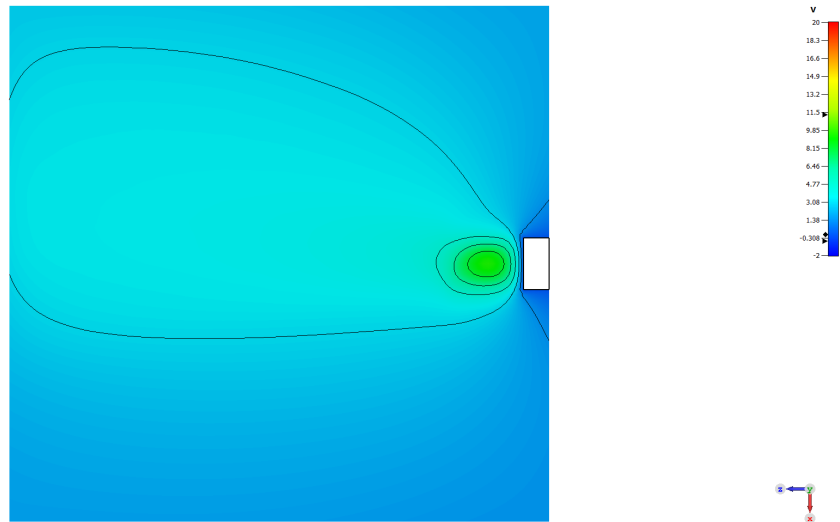


(b)

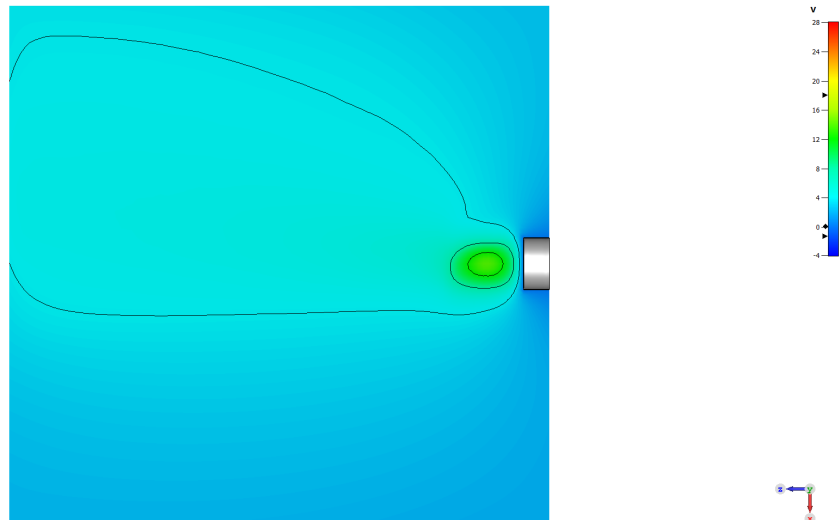


(c)

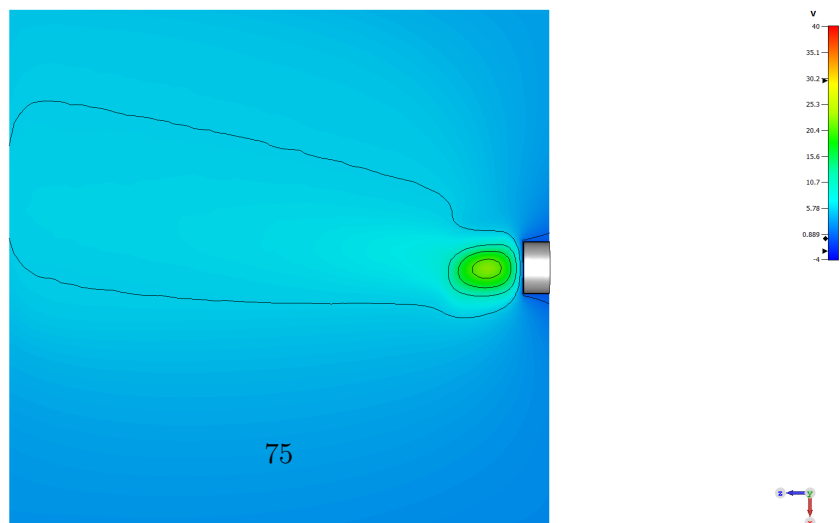
Figure 5.25: Electron density for thrust demands 3 mN (a), 8.3 mN (b) and 20 mN (c) on the center $z - x$ plane.



(a)

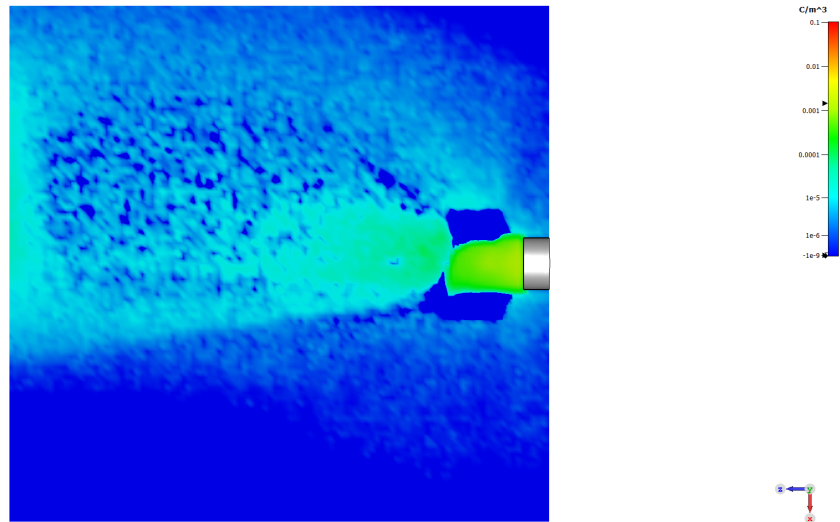


(b)

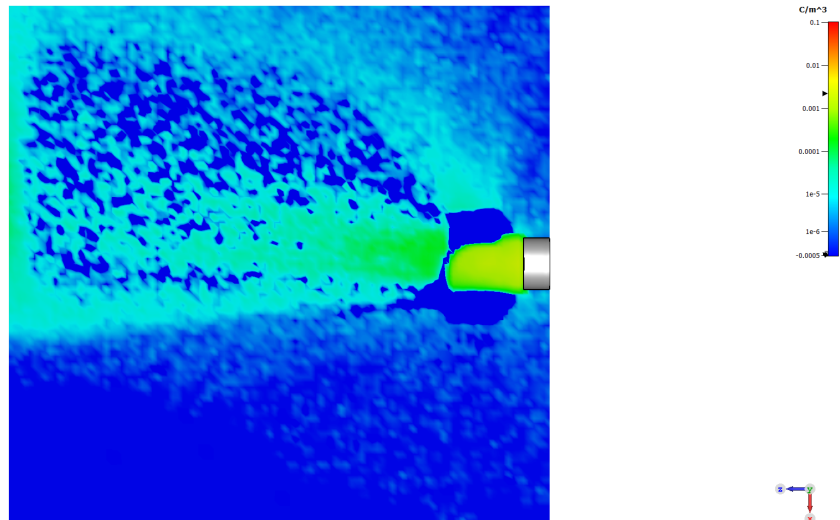


(c)

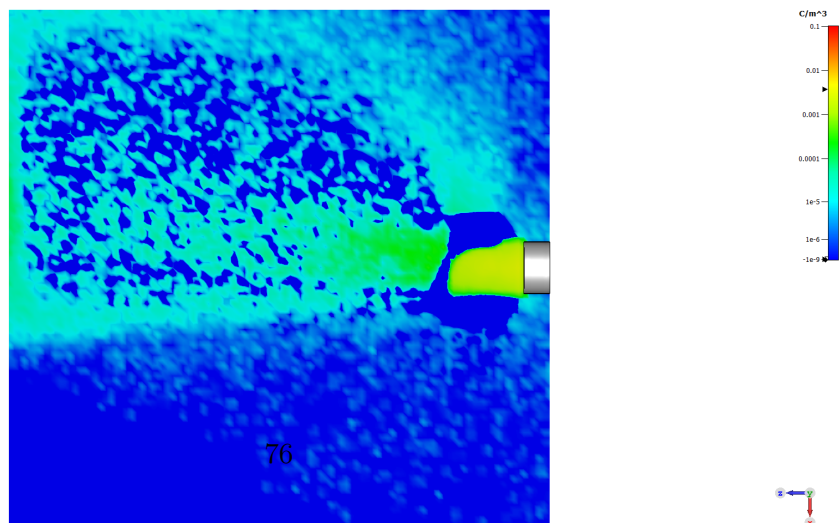
Figure 5.26: Potential maps for thrust demands 3 mN (a), 8.3 mN (b) and 20 mN (c) on the center $z - x$ plane.



(a)



(b)



(c)

Figure 5.27: Charge density maps for thrust demands 3 mN (a), 8.3 mN (b) and 20 mN (c) on the center $z - x$ plane.

5.3 Vectorial Magnetic Nozzle Concept

5.3.1 Preliminary Analysis

The VECMAN device is mentioned to be capable of generating thrust vector deflections for gridded ion thruster. It is decided to apply the magnetic field generated by a tilted at 30° coil to the GOCE's T5 ion thruster plasma plume model. Only one of three coils are simulated at the thruster's operating condition of 8.3 mN. The coil is placed at distance D from thruster exit and its radius is supposed to be

$$R_{coil} = 2R \quad (5.25)$$

The generated magnetic field is at the center of the coil in direction of its axis is

$$B_0 = \frac{\mu_0 IN}{2R_{coil}} = 0.2011 T \quad (5.26)$$

with $IN = 16000$ A-turns and $\mu_0 = 4\pi \times 10^{-7}$ Tm/A is the vacuum permeability. A series of test runs was performed to determinate the A-turn parameter. However, a component of magnetic field which generates a deflection should be in transversal direction to the thruster axis z . Thus,

$$B_y = B_0 \sin 30^\circ = 0.1005 T. \quad (5.27)$$

The simulation case is reported in Table (5.4).

Case	T (mN)	I_{beam} (mA)	I_{sp} (s)	R_{coil}	B_0 (Gauss)	B_y (Gauss)
1	8.3	155.8	2171.9	$2R$	2011	1005

Table 5.4: Simulation case to carry out a thruster vector angle of 8° with VMN.

5.3.2 Vectoring Performance

The model is illustrated in Figure (5.28). The neutraliser is placed as in validation plume model, close to the thruster. The simulation setup is the same of MTV concept. The simulation setup in terms of domain span, mesh and time is not altered with respect to MTV concept.

Before evolving the particles in time the magnetic field generated by a tilted coil is calculated by a CST Magneto-Static solver. Then, the field is imported in the Particle-In-Cell simulation and the particles are evolved across the magnetic field. Since the coil is tilted at angle 30° the field has two components along axes z and y . The magnetic fields B_z and B_y are illustrated in Figures (5.29) and (5.30), respectively. The field B_y is responsible of thrust steering.

In Figure (5.31) is reported ion density on $y = 0$ cutting plane, the plume deflection is obtained. It is interesting to observe that the beam divergence is smaller with respect to the steering by means of application of the uniform magnetic field (MTV concept). This

is due the existence of the field along the coil axis which magnetize slow ions, and thus their stream lines coincide with the magnetic field line. In addition, the color map of ion density (see Figure (5.31)) show the coil is on direct contact with plasma plume, which generates erosion on the thrust vectoring device. Once may increase the radius of the coil but the power consumption and weight will increase too.

Ion density distribution at different distances from the thruster exit (see Figure (5.33)) shows that the steering angle of 8° is achieved. Taking into account the reluctance of each component, a coil of 1.6×10^4 A-turns is found to be necessary to provide a deflection of 8° . Thus, assuming to use wires AWG-20 or similar, the weight of only one coil would be of the same order of magnitude of relatively small ion thruster of 10 cm diameter and the power consumption would be till 2 kW. This must be regarded as excessive and a prohibitively large mass, especially as it requires other 2 coils to provide vectoring in all azimuthal directions.

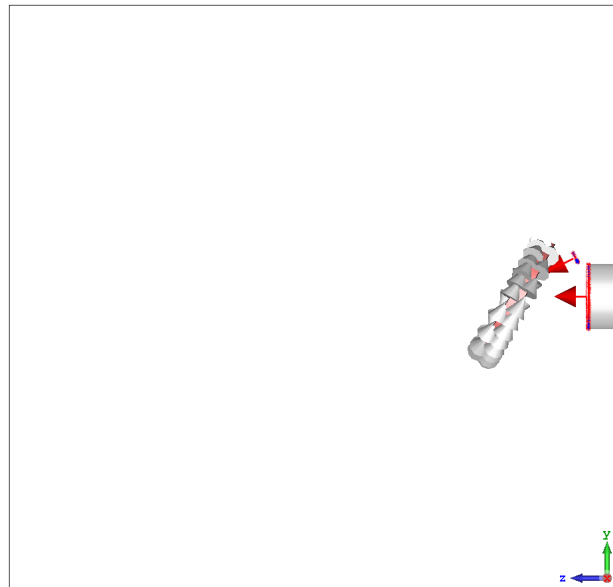


Figure 5.28: Simulation setup of VECMAN concept modeled with one coil placed at distance D from thruster exit on the center $z - y$ center. The neutraliser is positioned close to the thruster.

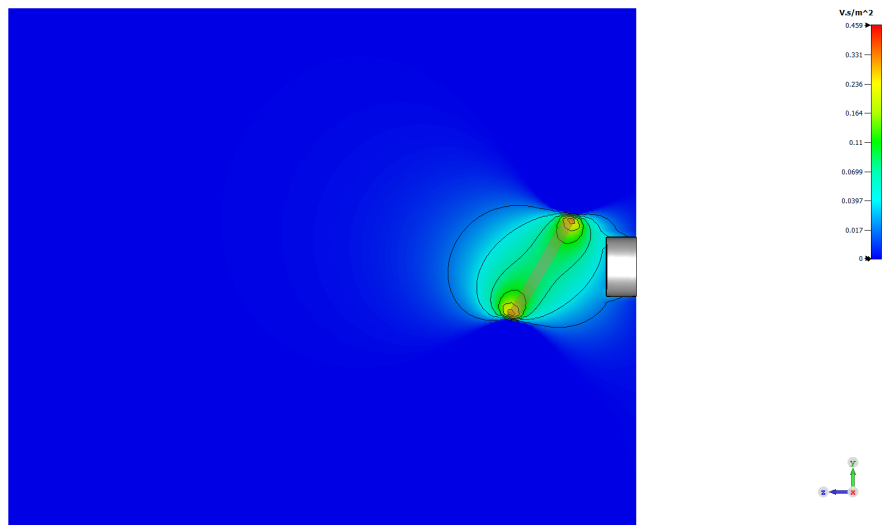


Figure 5.29: Magnetic field generated by a VECMAN coil tilted at 30° with respect to x axis on the center $z - y$ center. Map colors illustrate the magnitude of the magnetic field along z axis.

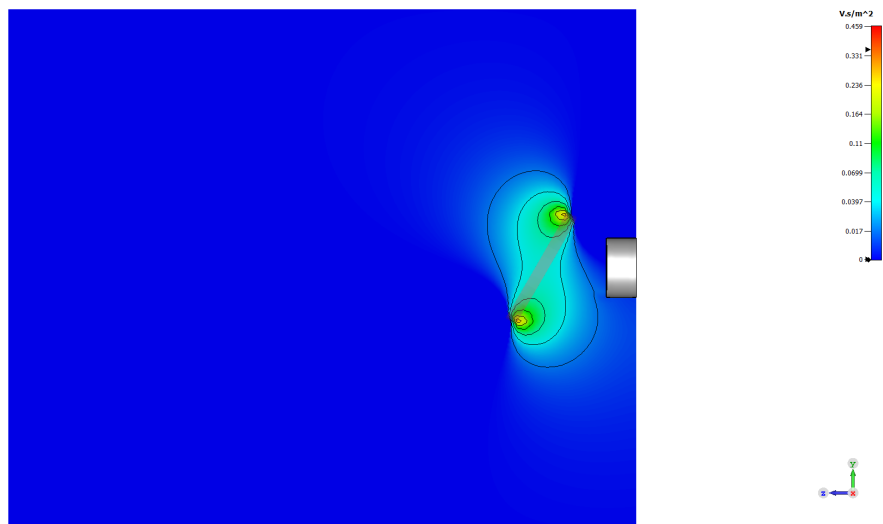


Figure 5.30: Magnetic field generated by a VECMAN coil tilted at 30° with respect to x axis. Map colors illustrate the magnitude of the magnetic field along y axis on the center $z - y$ center. The field B_y is responsible of thruster vectoring.

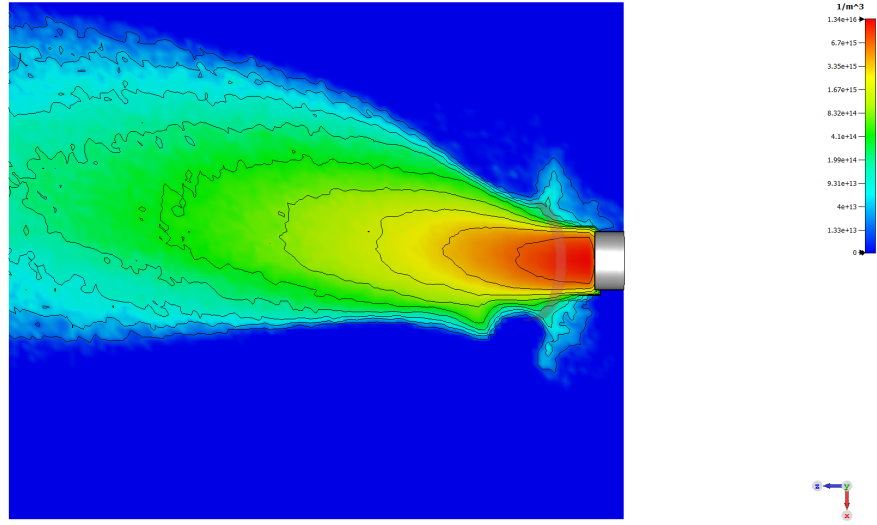


Figure 5.31: Ion density map on the center $z - x$ center.

The plume deflection along axis $-x$ is obtained as a consequence of application of the magnetic field generated by a tilted coil of VECMAN device. A smaller beam divergence can be seen with respect to the MTV concept reported in Figure (5.32).

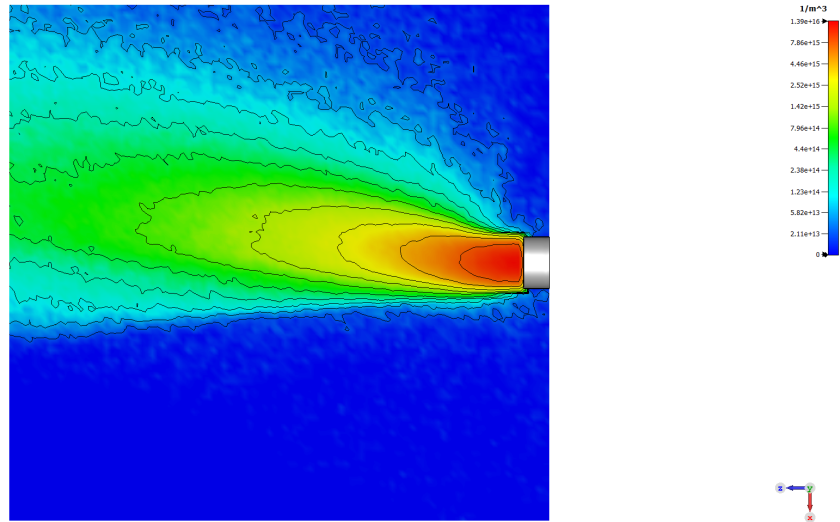


Figure 5.32: Ion density map on the center $z - x$ center.

The plume deflection along axis $-x$ is reached as a consequence of application of the uniform magnetic field generated along axis y . A bigger beam divergence can be seen with respect to the VECMAN concept in Figure (5.31).

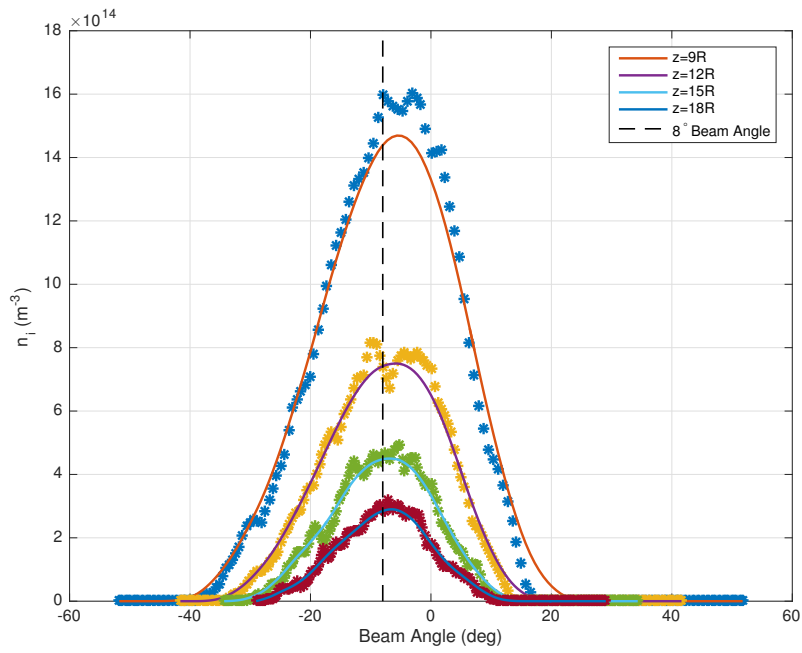


Figure 5.33: Ion density distribution at different distances from thruster exit. The plume has deflected by around 8° .

Chapter 6

Conclusions

6.1 Final discussion

This thesis is focused on developing a simulation methodology of ion thruster plasma plume by means of full-PIC commercial code, validation numerical results against experimental data and application of magnetic thrust vectoring concepts to the developed plume model. The background of the problem can be summarized in several points:

- The considered situation compromises the ion beam emitted from a spacecraft and thermal electrons ejected from a different position to provide the charge neutralization. The electron distribution function inside the plume is required to be solved and such aim is achievable by employing full-PIC, Particle-Particle or fully-kinetic algorithms. However, the last two are not computationally feasible to perform studies on three-dimensional domain. Hence, the CST Particle Studio solver is chosen to carry out full-PIC simulations in electrostatic mode. A special trial licence of the tool in beta version is provided by official distributors, since the ES-PIC solver will be released from 2019 version.
- In order to validate the code, the solver is applied to study the space charge emissions in vacuum and the numerical solution is compared against one-dimensional analytical model. The beam consisted of a single specie ions and, instead, of emitting the electrons, the neutralization is imposed by the external boundary, from which the beam exits the computational domain. Different neutralization distances from the source are taken in consideration.
- During the development of a plasma plume model several computational difficulties are met, since in order to evaluate correctly the space charge density the mesh and the time scale require to resolve the Debye length and the electron plasma frequency, respectively. Resolving these characteristics on the full-scale simulation domain is not feasible from a computational point of view. The calculations would require several years. For this reason, a scaling-down procedure is used [71] to decrease the dimensions by a factor of 100 and to solve the Debye length by the mesh. Input

parameters are adjusted to produce identical plasma environment to the full-scale model.

- Therefore, a natural question arises as to whether or not the numerical solution can be validated against the experimental data. For this reason, a comparison study between the numerical and experimental measurements of GOCE's T5 ITA is carried out.
- For what concerns the magnetic thrust vectoring, two concepts are applied to the plume model. Firstly, the uniformly applied magnetic field is sized and imported into the simulation domain as an external field. This study shows how the magnitude of the field and thruster's operating conditions influence the thrust vectoring performances. Moreover, the relative position of the neutraliser with respect to the TVC device is investigated too. Secondly, the ability of a patented device, Vectorial Magnetic Nozzle, is studied to steer the plasma plume.

Regarding the numerical results, the following achievements have been carried out:

- The code validation tests determined that the numerical solution is in excellent agreement with one-dimensional analytical model for the cases in which the beam emission radius is larger than the neutralization distance from the source. This is because, within such distance the ion flow can be considered as one-dimensional. Moreover, it was demonstrated that in three-dimensional scenario the neutralization requirements, in term of the distance from the source, are less severe compared to the one-dimensional analyzes. In 3D situations the beams have the freedom to expand their cross section prior the neutralization, in response to the space-charge forces. Thus, the practical observation made by Kaufman [7], about the position of the neutraliser, has been validated numerically.
- The validation campaign of the plume model showed excellent agreements in ion current density and plasma potential, while the discrepancy in electron density profile was attributed to errors made during the experimental test, which employed polarized Langmuir probes.
- The plume has been well neutralized with thermal electrons emitted from the upper side of the ion engine model. The electrons are attracted and then trapped electrostatically by the ion beam core. Their oscillating motion suggested the realization of the neutralization process.
- The transversally applied magnetic field concept has proved its ability to steer the thrust vector. Ion density distributions suggested deflections up to 8° with just 400 Gauss applied in transversal direction with respect to plume axis, for a thruster operating at 155 mA. Higher deflection angles are possible at cost of stronger magnetic fields or by its application for longer distances. Higher thrust levels require higher strength of magnetic field, while the direction of the TVC depends on the direction of the magnetic field. Nonetheless, ion density map showed increase in the plume

divergence on the side where the vectoring is required. Although, from the electron density and plasma potential maps, the achievement of the plume neutralization is obtained even with MTV switched on by placing the neutraliser emitter downstream the MTV device. Such modification is suggested in order to avoid the fully magnetization of neutralizing electrons.

- The VECMAN device has showed its bright side to have lower beam divergence compared to the first concept, since the field created by the coil converge the plume density. However, such concept is not found to be promising, because the necessary supply power would be up to double of that required by the thruster, while the weight of only one coil would be of the same order of magnitude of the engine.

Finalizing, from the results described above, the main objectives have been met:

- A model of ion thruster plasma plume consisted of ions and electrons ejected from different positions has been developed and validated against experimental data. This simulation methodology will allow Thales Alenia Space to study challenging neutralization architectures.
- The first magnetic thrust vectoring concept has been observed to be a promising solution. However, in order to achieve deflections in any azimuthal direction at different operating conditions, a device capable to rotate the field direction and change its magnitude is suggested. Since the CST ES-PIC and the Magneto-Static solvers are fully integrated, new concepts may be developed too.
- The application of the VECMAN device on a plasma plume of an ion thruster is not feasible for a required deflection angle. Its weight and the needed power supply are regarded as excessive, since to provide vectoring operations in all azimuthal directions, other 2 coils are necessary.

Bibliography

- [1] T. Melkumov, *Pioneers of Rocket Technology: Selected Works*, vol. 9285. National Aeronautics and Space Administration, 1965.
- [2] D. M. Goebel and I. Katz, *Fundamentals of electric propulsion: Ion and Hall thrusters*, vol. 1. John Wiley & Sons, 2008.
- [3] H. R. Kaufman, “Technology of electron-bombardment ion thrusters,” in *Advances in Electronics and Electron Physics*, vol. 36, pp. 265–373, Elsevier, 1975.
- [4] M. A. Lieberman and A. J. Lichtenberg, *Principles of plasma discharges and materials processing*. John Wiley & Sons, 2005.
- [5] C. Child, “Discharge from hot cao,” *Physical Review (Series I)*, vol. 32, no. 5, p. 492, 1911.
- [6] R. G. Jahn, *Physics of electric propulsion*. Courier Corporation, 2006.
- [7] H. R. Kaufman, “One-dimensional analysis of ion rockets,” tech. rep., National Aeronautics and Space Administration. Lewis Research Center, Cleveland, 1960.
- [8] I. Boyd and A. Ketsdever, “Interactions between spacecraft and thruster plumes,” *Journal of Spacecraft and Rockets*, vol. 38, no. 3, pp. 380–380, 2001.
- [9] F. Cichocki, M. Merino, and E. Ahedo, “Modeling and simulation of ep plasma plume expansion into vacuum,” in *50th AIAA/ASME/SAE/ASEE Joint Propulsion Conference*, p. 3828, 2014.
- [10] R. Myers, E. Pencil, V. Rawlin, M. Kussmaul, and K. Oden, “Nstar ion thruster plume impacts assessment,” in *31st Joint Propulsion Conference and Exhibit*, p. 2825, 1995.
- [11] P. De Boer, “Electric probe measurements in the plume of an ion thruster,” *Journal of propulsion and power*, vol. 12, no. 1, pp. 95–104, 1996.
- [12] J. E. Pollard, “Profiling the beam of the t5 ion engine,” *IEPC Paper*, pp. 97–019, 1997.
- [13] P. T. De Boer, “Measurements of electron density in the charge exchange plasma of an ion thruster,” *Journal of propulsion and power*, vol. 13, no. 6, pp. 783–788, 1997.

-
- [14] J. Foster, G. Soulas, and M. Patterson, "Plume and discharge plasma measurements of an nstar-type ion thruster," in *36th AIAA/ASME/SAE/ASEE Joint Propulsion Conference and Exhibit*, p. 3812, 2000.
- [15] R. M. Myers and D. H. Manzella, "Stationary plasma thruster plume characteristics," 1994.
- [16] L. B. King and A. D. Gallimore, "Ion-energy diagnostics in the plasma exhaust plume of a hall thruster," *Journal of Propulsion and Power*, vol. 16, no. 5, pp. 916–922, 2000.
- [17] B. E. Beal, A. D. Gallimore, and W. A. Hargus Jr, "Plasma properties downstream of a low-power hall thruster," *Physics of plasmas*, vol. 12, no. 12, p. 123503, 2005.
- [18] M. Nakles, L. Brieda, G. Reed, W. Hargus, and R. Spicer, "Experimental and numerical examination of the bht-200 hall thruster plume," in *43rd AIAA/ASME/SAE/ASEE Joint Propulsion Conference & Exhibit*, p. 5305, 2007.
- [19] K. Dannenmayer, S. Mazouffre, M. Merino-Martinez, and E. Ahedo, "Hall effect thruster plasma plume characterization with probe measurements and self-similar fluid models," in *48th AIAA/ASME/SAE/ASEE Joint Propulsion Conference & Exhibit*, p. 4117, 2012.
- [20] A. Korsun, E. Tverdokhlebova, and F. Gabdullin, "Earth's magnetic field effect upon plasma plumes expansion," 1997.
- [21] M. Tajmar, B. Foing, J. Gonzalez, G. Noci, W. Schmidt, and F. Darnon, "Charge-exchange plasma contamination on smart-1: First measurements and model verification," in *40th AIAA/ASME/SAE/ASEE Joint Propulsion Conference and Exhibit*, p. 3437, 2004.
- [22] F. F. Gabdullin, A. G. Korsun, and E. M. Tverdokhlebova, "The plasma plume emitted onboard the international space station under the effect of the geomagnetic field," *IEEE Transactions on Plasma Science*, vol. 36, no. 5, pp. 2207–2213, 2008.
- [23] G. B. Julie Owen, Matt Potts, "Goce ita plume characterisation go-tn-qiq-0003 issue 3.0," tech. rep., QinetiQ Space Department, 2005.
- [24] C. M. S.R. Doughty, M.C. Potts and G. Baker, "Goce ita retrofit test report go-tn-qiq-0035 issue 2.0," tech. rep., QinetiQ Space Department, 2006.
- [25] M. Martinez-Sanchez and J. E. Pollard, "Spacecraft electric propulsion-an overview," *Journal of propulsion and power*, vol. 14, no. 5, pp. 688–699, 1998.
- [26] C. K. Birdsall and A. B. Langdon, *Plasma physics via computer simulation*. CRC press, 2004.

- [27] M. Zirnbauer, N. Memmel, A. Benninghoven, H. Kastrup, K. Bethge, P. Brix, T. Bührke, H. Rechenberg, and K. Von Meyenn, “Hockney u. eastwood: Computer simulation using particles/zangwill: Physics at surfaces/zirnbauer/watt u. grime: Principles and applications of high-energy ion microbeams/batalin, isham u. vilkovichsky: Quantum field theory and quantum statistics: Essays in honour of the sixtieth birthday of es fradkin, vol. 1 a. 2/wollnik: Optics of charged particles/swinne: Hans geiger: Spuren aus einem leben für die physik/roth: Taschenbuch für planetenbeobachter/dresden: Ha kramers—between tradition and revolution/glick: The comparative reception of relativity,” *Physikalische Blätter*, vol. 44, no. 11, pp. 435–437, 1988.
- [28] Y. Zhao, J. Wang, and H. Usui, “Simulations of ion thruster beam neutralization using a particle–particle model,” *Journal of Propulsion and Power*, pp. 1–7, 2018.
- [29] R. S. Roy, D. Hastings, and N. Gastonis, “Numerical study of spacecraft contamination and interactions by ion-thruster effluents,” *Journal of Spacecraft and Rockets*, vol. 33, no. 4, pp. 535–542, 1996.
- [30] J. Wang, D. Brinza, and M. Young, “Three-dimensional particle simulations of ion propulsion plasma environment for deep space 1,” *Journal of Spacecraft and Rockets*, vol. 38, no. 3, pp. 433–440, 2001.
- [31] M. Ruiz, I. Urdampilleta, C. Bombardelli, E. Ahedo, M. Merino, and F. Cichocki, “The fp7 leosweep project: Improving low earth orbit security with enhanced electric propulsion,” in *Space Propulsion Conference*, no. 2980908, 2014.
- [32] D. Parks and I. Katz, “A preliminary model of ion beam neutralization,” in *14th International Electric Propulsion Conference*, p. 2049, 1979.
- [33] N. Leveque, C. Welch, A. Ellery, and A. Curley, “Trajectory simulations for thrust-vectoring electric propulsion missions,” in *28th International Electric Propulsion Conference*, 2003.
- [34] D. G. Fearn, “Ion thruster thrust vectoring requirements and techniques,” in *International Electric Propulsion Conference, Pasadena*, pp. 1–115, 2001.
- [35] V. Obukhov and et al., “Method of control of spacecraft motion and control system for realization of this method,” *Google Patents*, p. RU2309876C1, 2006.
- [36] R. Killinger, R. Kukies, M. Surauer, A. Tomasetto, and L. van Holtz, “Artemis orbit raising inflight experience with ion propulsion,” *Acta Astronautica*, vol. 53, no. 4, pp. 607 – 621, 2003. The New Face of Space Selected Proceedings of the 53rd International Astronautical Federation Congress.
- [37] B. Wood, W. Buff, and P. Delouard, “Smart-1 electrical propulsion steering mechanism (epmec),” in *Proc. 9th European Space Mechanisms & Tribology Symposium, Liege*, pp. 19–21, 2001.

- [38] A. Wittmann, “Redundant system for satellite inclination control with electric thrusters,” May 20 2003. US Patent 6,565,043.
- [39] H. Gray, S. Provost, M. Glogowski, and A. Demaire, “Inmarsat 4f1 plasma propulsion system initial flight operations,” in *29th International Electric Propulsion Conference*, 2005.
- [40] J. Biron, N. Cornu, H. Illand, M. Serrau, R. Rigollet, and H. Gray, “The thruster module assembly (hall-effect thruster) design, qualification and flight,” in *29th International Electric Propulsion Conference, IEPC-2005-213, Princeton, NJ*, 2005.
- [41] V. Petrosov, “A concept of development of electric thrusters with thrust vector control,” in *27th International Electric Propulsion Conference*.
- [42] O. Duchemin, M. Prioul, H. Illand, S. Banetta, A. Vicini, L. Garrigues, R. Rigollet, and D. Estublier, “Development of a prototype thrust steering device for hall-effect thrusters,” in *4th International Spacecraft Propulsion Conference*, vol. 555, 2004.
- [43] P. Smith, “Thrust vector control unit for an ion thruster,” *BAE Systems Electronics Ltd/Matra Marconi Space UK Ltd*, p. EP0468706A2, 1990.
- [44] A. Kural, N. Leveque, C. Welch, and P. Wolanski, “Design of an ion thruster movable grid thrust vectoring system,” *Acta Astronautica*, vol. 55, no. 3-9, pp. 421–432, 2004.
- [45] Y. e. a. Yashnov, “Vector magnetic nozzle used for electric propulsion,” *KELDYSH RESEARCH CENTER Airbus Defence and Space SAS*, p. EP0778415B1, 1995.
- [46] O. Duchemin, H. Illand, M. Saverdi, U. Cesari, M. Signori, D. Pagnon, and D. Estublier, “Testing of a thrust steering device on the pps® 1350 hall thruster,” in *42nd AIAA/ASME/SAE/ASEE Joint Propulsion Conference & Exhibit*, p. 4478, 2006.
- [47] L. Garrigues, C. Boniface, G. M. Hagelaar, J. Boeuf, and O. Duchemin, “Performance modeling of a thrust vectoring device for hall effect thrusters,” *Journal of propulsion and power*, vol. 25, no. 5, pp. 1003–1012, 2009.
- [48] G. Emsellem and et al., “Low-thrust rocket engine for space vehicle,” *Google Patents*, p. RU2445510C2, 2004.
- [49] A. e. a. Bishaev, “Device for vector control of plasma engine strip (options) and method of vector control of plasma engine strip,” *Google Patents*, p. RU2644810C2, 2015.
- [50] M. Merino and E. Ahedo, “Sistema sin partes móviles ni electrodos y procedimiento para vectorizar el empuje en motores espaciales de plasma,” *Spanish Patent Office*, p. P201331790, 2013.
- [51] M. Merino and E. Ahedo, “Contactless steering of a plasma jet with a 3d magnetic nozzle,” *Plasma Sources Science and Technology*, vol. 26, no. 9, p. 095001, 2017.

- [52] Z. HUA and et al., “Vector magnetic nozzle used for electric propulsion,” *BEIJING INSTITUTE SPACECRAFT ENVIRONMENT ENGINEERING*, p. CN102777342B, 2012.
- [53] C. Charles, R. Boswell, W. Cox, R. Laine, and P. MacLellan, “Magnetic steering of a helicon double layer thruster,” *Applied Physics Letters*, vol. 93, no. 20, p. 201501, 2008.
- [54] B. Lin and J. Sheehan, “Simulations and preliminary measurements of a magnetic nozzle thrust vectoring system,” 01 2018.
- [55] M. Merino and E. Ahedo, “Towards thrust vector control with a 3d steerable magnetic nozzle,” in *34th International Electric Propulsion Conference, No. IEPC-2015-414, Electric Rocket Propulsion Society, Fairview Park, OH*, vol. 29, 2015.
- [56] L. Tonks, “L. tonks and i. langmuir, phys. rev. 33, 195 (1929),” *Phys. Rev.*, vol. 33, p. 195, 1929.
- [57] J. Wang, J. Brophy, and D. Brinza, “3-d simulations of nstar ion thruster plasma environment,” in *32nd Joint Propulsion Conference and Exhibit*, p. 3202, 1996.
- [58] J. Wang and J. Brophy, “3-d monte-carlo particle-in-cell simulations of ion thruster plasma interactions,” in *31st Joint Propulsion Conference and Exhibit*, p. 2826, 1995.
- [59] Y. L. Klimontovich, “The statistical theory of non-equilibrium processes in a plasma,” *Journal of Plasma Physics*, vol. 3, p. 148, 1969.
- [60] D. R. Nicholson and D. R. Nicholson, *Introduction to plasma theory*. Wiley New York, 1983.
- [61] A. A. Vlasov, “The vibrational properties of an electron gas,” *Physics-Uspekhi*, vol. 10, no. 6, pp. 721–733, 1968.
- [62] R. W. Hockney and J. W. Eastwood, *Computer simulation using particles*. crc Press, 1988.
- [63] D. Anderson, J. C. Tannehill, and R. H. Pletcher, *Computational fluid mechanics and heat transfer*. CRC Press, 2016.
- [64] J. P. Boris, “Relativistic plasma simulation-optimization of a hybrid code,” in *Proc. 4th Conf. Num. Sim. Plasmas*, pp. 3–67, 1970.
- [65] C. PS, *CST - Computer Simulation Technology*, 2018 (accessed June 15, 2018).
- [66] J. Wang and S. T. Lai, “Virtual anode in ion beam emissions in space: Numerical simulations,” *Journal of spacecraft and rockets*, vol. 34, no. 6, pp. 829–836, 1997.
- [67] C. Fay, A. Samuel, and W. Shockley, “On the theory of space charge between parallel plane electrodes,” *Bell System Technical Journal*, vol. 17, no. 1, pp. 49–79, 1938.

- [68] H. Usui, A. Hashimoto, and Y. Miyake, “Full pic simulation of ion beam neutralization,”
- [69] L. Brieda, “Model for steady-state fully kinetic ion beam neutralization studies,” *IEEE Transactions on Plasma Science*, vol. 46, no. 3, pp. 556–562, 2018.
- [70] L. Brieda and J. Wang, “Modelling ion thruster beam neutralization,” in *41st AIAA/ASME/SAE/ASEE Joint Propulsion Conference & Exhibit*, p. 4045, 2005.
- [71] L. Brieda, *Development of the DRACO ES-PIC code and fully-kinetic simulation of ion beam neutralization*. PhD thesis, Virginia Tech, 2005.
- [72] J. Wang, O. Chang, and Y. Cao, “Electron–ion coupling in mesothermal plasma beam emission: Full particle pic simulations,” *IEEE transactions on plasma science*, vol. 40, no. 2, pp. 230–236, 2012.
- [73] Y. Hu and J. Wang, “Electron properties in collisionless mesothermal plasma expansion: fully kinetic simulations,” *IEEE Transactions on Plasma Science*, vol. 43, no. 9, pp. 2832–2838, 2015.
- [74] Y. Hu and J. Wang, “Fully kinetic simulations of collisionless, mesothermal plasma emission: Macroscopic plume structure and microscopic electron characteristics,” *Physics of Plasmas*, vol. 24, no. 3, p. 033510, 2017.
- [75] Y. Hu and J. Wang, “Modeling electron characteristics in an ion thruster plume: Fully kinetic pic vs. hybrid pic,” 2017.
- [76] www.supermagnete.it, *supermagnete*, 2018 (accessed November 15, 2018).